Boundary Layer and Shock Detection in CFD Solutions

by

David Lovely

Submitted to the Department of Aeronautics and Astronautics
in partial fulfillment of the requirements for the degree of

Masters of Science in Aeronautical Engineering

at the

MASSACHUSETTS INSTITUTE OF TECHNOLOGY

February 2000

Author .....
Department of Aeronautics and Astronautics
October 18, 1999

Certified by .....
Robert Haimes
Principal Research Engineer
Thesis Supervisor

Accepted by .....
Nesbitt Hagood
Chairman, Graduate Committee

Boundary Layer and Shock Detection in CFD Solutions

by

David Lovely

Submitted to the Department of Aeronautics and Astronautics
on October 18, 1999, in partial fulfillment of the
requirements for the degree of
Masters of Science in Aeronautical Engineering

Abstract

The motivation for feature detection research is to provide analysts with quantitative information about features of interest, without the need for manually probing the solution field. This thesis investigates new feature detection algorithms for shocks in compressible flow solutions and boundary layers in viscous solutions. These new algorithms were designed to be applied in a co-processing step, filtering the massive quantities of data and extracting physically meaningful flow characteristics.

Shock detection algorithms were developed to locate, classify and determine shock strength for both transient and steady state solutions. The algorithm uses the physics of the flow field to calculate a marker quantity that correlates with the location of shock. The marker quantity is an approximation to the Mach number normal to a moving or stationary shock. Since the Mach number relative to the shock wave has to pass through unity, this number can be used as a threshold to mark regions of likely shocks. Unfortunately, the marker quantity has some undesirable properties for a shock detector, picking out areas of the flow that are not shocks, so some other filters had to be created to remove these false indications.

The boundary layer algorithms estimate the displacement and momentum thickness on the solid boundaries of a CFD solution domain. The challenge in designing this algorithm was to make it applicable to any geometry and flow situation. This required a careful definition of the boundary layer, because some measures of the boundary layer thickness have a physical meaning in the two-dimensional flows, but loose that meaning in moving to a more complex topology.

The boundary layer thickness algorithms works in two steps, first estimating the free stream velocity by integrating vorticity components along curves normal to the wall. The second step is to integrate the mass flow rate and momentum flow rate in this region and construct a displacement and momentum thickness from these quantities. Comparisons were made between the actual free stream velocities and calculated free stream velocities for some standard two and three-dimensional flows. Results were encouraging; often coming within a percentage of the theoretical value, and sometimes finding the exact free stream function.

A numerical technique is introduced to perform the mass flow and momentum cal-

culations. The technique involves casting the streamline and stream-tube integrations as a linear convection problem, and then solving that problem. Results of the full boundary layer thickness estimation technique applied to a corner flow model show that it is possible to estimate the boundary layer thickness as a function along the solid surface of the model, without having any discontinuities in the function. The technique was also tested on two airfoil flow models, one in a laminar flow regime, the other in a turbulent flow. The comparison of displacement thickness estimated with the new technique to the displacement thickness calculated within the CFD solution process was within 10 percent.

Applications to more complex flows will have to deal with cases where vorticity is added from outside the boundary layer such as curved shocks and wakes from upstream bodies, but do not effect boundary layer thickness.

Thesis Supervisor: Robert Haimes
Title: Principal Research Engineer

Acknowledgments

The shock detection algorithm has been an extension of the work done by David Darmofal and others. Professor Mark Drela was instrumental in finding the unsteady extensions to the basic algorithm, as well as providing understanding of the boundary layer equations. Tim Barth was also a great resource for discussing boundary layer detection. I would also like to thank others in the Fluid Dyamics Research Lab, Ali Merchant and Alex Budge in particular for letting me use there datasets.

Funding for this project has been provided by NASA Ames, through grant number NCC2-985, and by the Army under grant DAAG55-97-1-0394.

0.1 Shock Wave Nomenclature

P	Pressure
ρ	Density
a	Speed of sound
U	Speed
M	Mach number
$\vec{M} = \frac{\vec{q}M}{U}$	Mach vector
γ	ratio of specific heats
$\vec{q}$	Velocity

0.2 Boundary Layer Nomenclature

P	Pressure
ρ	Density
δ	boundary-layer thickness
δ_1	Displacement thickness
δ_2	Momentum thickness
U	Velocity outside the boundary layer
u	local x velocity component
v	local y velocity component
w	local z velocity component
μ	absolute viscocity
μ_t	turbulent viscocity
$\nu = \mu/\rho$	kinematice viscosity
ν_t	turbulent kinematic viscosity
ω	vorticity

Contents

0.1 Shock Wave Nomenclature 5

0.2 Boundary Layer Nomenclature 5

1 Introduction **14**

1.1 Shock Waves 14

1.2 Boundary Layers 16

1.2.1 2D Boundary Layers 17

1.2.2 3D Boundary Layers 18

1.2.3 Flow Blockage 20

2 Stationary Shock Wave Detection **24**

2.1 Shock strength 25

2.2 Shock Classification 26

2.3 Grid Study 27

2.4 Supersonic projectile 31

3 Transient Shock Wave Detection **34**

3.0.1 Translating normal shock in a tube 35

4 Filtered Shock Detection Results **42**

4.1 Transonic Aircraft 46

5 Boundary Layer Detection **49**

5.1 Boundary Layer Definition 49

5.2 Possible Detection Methods 53

5.2.1 Potential flow quantities 53
5.2.2 Comparison with boundary layer theory 56
5.2.3 Turbulence model quantities 57
5.2.4 Integration schemes 57
5.2.5 Integration End Points 58
5.2.6 Geometric Difficulties 60

6 2D Boundary layer detection **66**
6.1 Flat plate results 66
6.1.1 Velocity integration vs. vorticity integration 66
6.2 Pipe Flow 70
6.2.1 Boundary layer measurements in channels 72
6.3 Boundary layer detection on a laminar flow airfoil model 73
6.4 Boundary layer detection on a turbulent flow airfoil model 80

7 3D Boundary Layer Detection **87**
7.1 Axisymmetric Stagnation Flow 87
7.2 Axisymmetric Stagnation Flow With Swirl 89

8 Integration Methods **92**
8.1 One dimensional test problems 92
8.2 Boundary layer integration as a solution to the convection equations . 94
8.2.1 1D model 96
8.2.2 Higher dimensions 97
8.2.3 Discretizing the equations 98
8.2.4 Corner flow test case 100
8.2.5 Laminar airfoil test case 104
8.2.6 Turbulent airfoil test case 108
8.2.7 Time dependant problems 110
8.2.8 Other three dimensional issues 111
8.3 Summary of Boundary Layer Detection Technique 111

9 Conclusions **113**

9.1 Shock Detection 113

9.2 Boundary Layer Description 114

List of Figures

1-1 Shock inflection points 16
1-2 Boundary Layer Definitions 17
1-3 Three dimensional boundary layer profiles 19
1-4 Swept wing boundary layer integration coordinates 20
1-5 Boundary Layer on Curved Surface 21
1-6 2D vs Curved Approximations 21
1-7 Displacement Thickness vs. Radius of Curvature 22

2-1 Shock detection test quantity 24
2-2 Computed vs. actual pressure ratio 26
2-3 Ramp model 28
2-4 Grid Refinement On Wedge Model 28
2-5 Shock contours on the coarse grid 29
2-6 Shock contours on the more refined grid 29
2-7 Shock contours on highly refined grid 30
2-8 Three dimensional shock representation on a projectile model in mach 1.2 flow 31
2-9 Shock strength false color image 32
2-10 Pressure gradient magnitude 33

3-1 Transient Shock Model 36
3-2 Pressure Distribution 37
3-3 Shock Scalar 38
3-4 Shock Scalar at δt 38

3-5 Shock scalar with unfiltered pressure gradient 39
3-6 Normal Mach Number vs. Location 39
3-7 Shock scalar vs. Location 40
3-8 Theoretical vs. Experimental Shock Location 41

4-1 Stationary shock algorithm applied to converged solution 44
4-2 Transient shock algorithm without filtering 45
4-3 Transient shock algorithm with pressure gradient magnitude filter . . 45
4-4 Shock detection algorithm applied to a Euler solution of an aircraft model 47
4-5 Unsteady shock detection algorithm applied to a euler solution of an aircraft model 48

5-1 Typical boundary layer profile 50
5-2 Cannel flow viscous and inviscid solution 51
5-3 Number of Nodes with Vorticity Magnitude Less than the Threshold vs. Threshold Value 55
5-4 Variation in boundary layer thickness with changes in integration end point 59
5-5 Velocity and velocity derivative profiles for various regimes 60
5-6 Boundary layer surface represented as a function of arc length 61
5-7 Corner Flow Model 62
5-8 ϕ Function and values of $\frac{u}{U}$ 63
5-9 ψ Function contours 63
5-10 ψ and ϕ contours 64
5-11 Areas used in displacement thickness calculation 64
5-12 Corner flow calculated vs. theoretical displacement curve 65

6-1 Vorticity plot on the flat plate test case 68
6-2 Displacement Thickness Calculated vs. Theoretical 68
6-3 Momentum Thickness Calculated vs. Theoretical 69

6-4 Calculated vs. theoretical displacement thickness 69
6-5 Calculated vs. theoretical momentum thickness 70
6-6 Pipe flow model geometry 71
6-7 Integration Areas for the pipe 73
6-8 Velocity contours on NACA0012 airfoil in Re = 500 flow 74
6-9 Vorticity contours on NACA0012 airfoil in Re = 500 flow 75
6-10 Free stream velocity calculation on airfoil in laminar flow, $\frac{x}{c} = 0.118$. 76
6-11 Free stream velocity calculation on airfoil in laminar flow, $\frac{x}{c} = 0.327$. 77
6-12 Free stream velocity calculation on airfoil in laminar flow, $\frac{x}{c} = 0.89$. 78
6-13 Calculated free stream velocity on laminar flow airfoil model 79
6-14 Calculated displacement thickness on laminar flow airfoil model . . . 80
6-15 Free stream velocity estimation at $\frac{x}{c} = 0.1$ 81
6-16 Free stream velocity estimation at $\frac{x}{c} = 0.008$ 82
6-17 Free stream velocity vs. location 83
6-18 Displacement thickness vs. location on upper airfoil surface 84
6-19 Displacement thickness vs. location on lower airfoil surface 85

7-1 Stagnation flow model geometry 88
7-2 Stagnation flow model with swirl 90

8-1 Element length vs. the error in displacement thickness 93
8-2 Element length vs. the error in momentum thickness 93
8-3 Boundary layer integration volume 95
8-4 Function integration as convection 96
8-5 Area integration as a solution to the convection equations 98
8-6 Typical Triangulated Domain 100
8-7 Area convection results after 10 iterations 101
8-8 Area convection results after 30 iterations 101
8-9 Convected area calculation 102
8-10 Convection values without damping: Area = 1.01, with damping: Area = 0.97 103

8-11 Dissipation constant vs. integrated area value 104
8-12 Displacement thickness curve 105
8-13 Displacement thickness curve for coarse grid 105
8-14 Convecting vorticity on a laminar airfoil model 106
8-15 Normal curves used for convecting vorticity on the laminar airfoil model 107
8-16 $\nabla\phi$ solution for convection velocity 108
8-17 Convecting vorticity on a turbulent airfoil model 109

List of Tables

2.1 Grid study results 30

4.1 Filtering study results 46

8.1 Boundary Layer Integration Parameters 94

Chapter 1

Introduction

This thesis discusses new numerical techniques in the areas of shock detection and boundary layer description. An attempt was made to use the physics of the situation to extract these features, instead of using a more generalized approach, although the goals are sometimes the same. Because the physics of shock waves and boundary layers are so different, they are presented independently.

1.1 Shock Waves

Shocks are a type of compression wave in flow fields that may occur when the velocity of the fluid exceeds the local speed of sound. The state of the fluid as described by the pressure, velocity and other primitive variables can change radically across a shock boundary of only a few molecular mean free paths wide. There are many types of discontinuities, but this thesis will only deal with simple shocks; compression discontinuities without heat addition and with constant specific heats. Shock discontinuities are of interest to designers because their strength and location affects drag on aircraft, the functioning of inlets, the efficiency of nozzles and a host of other design problems in fluid mechanics.

When fluid dynamic problems are simulated numerically with CFD codes, the real flow discontinuities often persist, but become harder to detect because of the numerical properties of the solution. The problem is analogous to finding edges in an

image, the purpose of both applications is to find discontinuities in a scalar field that contain large spatial changes in the scalar along with noise and smoothing. In the case of CFD solutions, the noise in the solution is analogous to dispersion and the smoothing is related to dissipation. Figure 1-1 shows the how the pressure across the idealized pressure discontinuity at a shock differs from an actual shock. Dissipation blurs the edges of the shock, making it hard to determine its extent. Dispersion creates the high frequency noise on the edges of the shock.

There are a couple of approaches to detecting shock discontinuities. The first approach is to view it as an edge detection problem and apply the methods that have been developed in that field. Alternatively the physics of shocks can be used to create a detection algorithm that is not applicable to the more general problem. This thesis takes the physics approach since there is not an agreed on 'best' edge detection algorithm and by looking at the physics, it might be possible to formulate a more rigorous detector.

In the past, shock waves have been extracted with an edge detection technique described by Ma, Rosendale, and Vermeer [1]. This technique searches for inflection points in the pressure or density fields by finding areas where the LaPlacian of the scalar quantity goes to zero. This works because scalar quantities like pressure have their maximum rate of increase at the shock and the second derivative of the scalar goes to zero, as shown in the figure 1-1. However, this detector will pick up other features that are not shocks. There can be expansion waves in a flow solution that are similar to shock features, except pressure and density decrease along streamlines through the expansion. The second derivatives of pressure and density are also zero in quiescent flow like regions far from a body. Both these artifacts have to be removed from the marked areas. One advantage of this approach is that it also captures moving shocks in a transient solution, since pressure and density are invariant quantities; unchanged when the frame of reference is attached to a moving shock.

A second method is to use the pressure gradient to find the value of the mach number normal to a shock. The approach was outlined by Darmofal [2] and also implemented in Plot3D [3]. Since the shock surface normal will be aligned with the

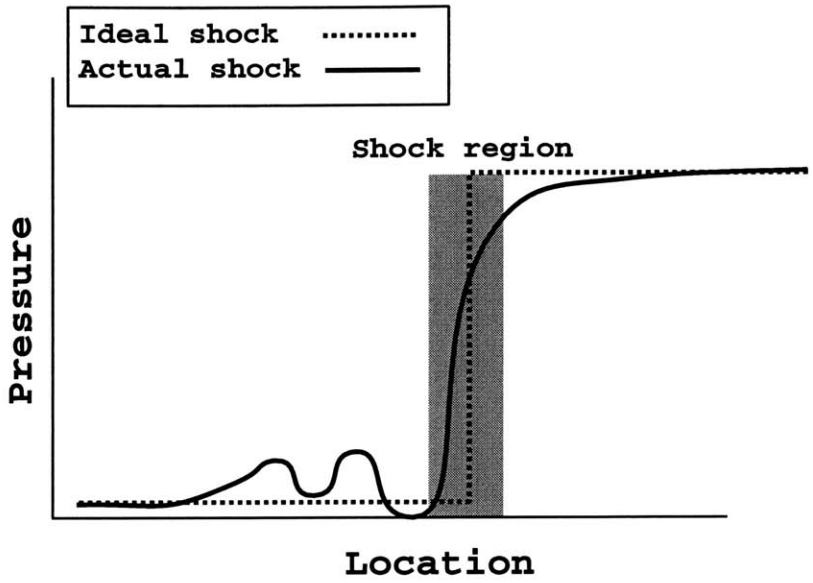

Figure 1-1: Shock inflection points

pressure gradient vector, the mach number in the direction of this vector is the normal Mach number. A shock is then located where this normal Mach number is greater than or equal to one.

One disadvantage of this shock finding method is that it will fail to capture some moving shocks in transient solutions. The mach vector is calculated in the CFD solution relative to the model frame of reference, but the shock calculation uses the mach vector in the shock frame of reference. For example, a shock traveling in a shock tube can exist when the fluid in the tube is moving at a velocity less than the speed of sound. Only when the Mach number is calculated with respect to the moving shock would this shock be detected. This thesis later describes extensions to the normal Mach number calculation that makes it applicable to moving shocks.

1.2 Boundary Layers

In most flows of engineering interest, the effects of the fluid inertia dominate over the effects of viscosity. The relative importance of the properties is described by the Reynolds number, $\frac{\rho U_\infty x}{\nu}$, where ρU_∞ reflects the influence of inertia and the ν term reflects the influence of viscosity. For cases of high Reynolds numbers, it is useful to

envision the flow as being composed of two regions; a far field region where viscosity is essentially zero, and a region close to the wall where the viscosity enforces the no-slip condition. The size and shape of the viscous region provides information about drag and flow blockage.

1.2.1 2D Boundary Layers

In real 2D flows, the velocity varies continuously from some free stream value to zero at the wall, so location of the boundary layer edge is subjective. It is often stated as the location where the velocity reaches 95% - 99% of it's free stream value. More objective measures of the boundary layer are the displacement thickness and momentum thickness. These two measures compare the actual velocity profile to a flow that has a step discontinuity at some distance away from the wall. The approximate velocity profile looks like one of those in figure 1-2. The displacement thickness is related to the velocity of the flow with the following equation.

$$\delta_1 = \int_0^{\delta} (1 - \frac{u}{U}) dn \tag{1.1}$$

The displacement thickness is a measure of the flow restriction and mass flow deficit

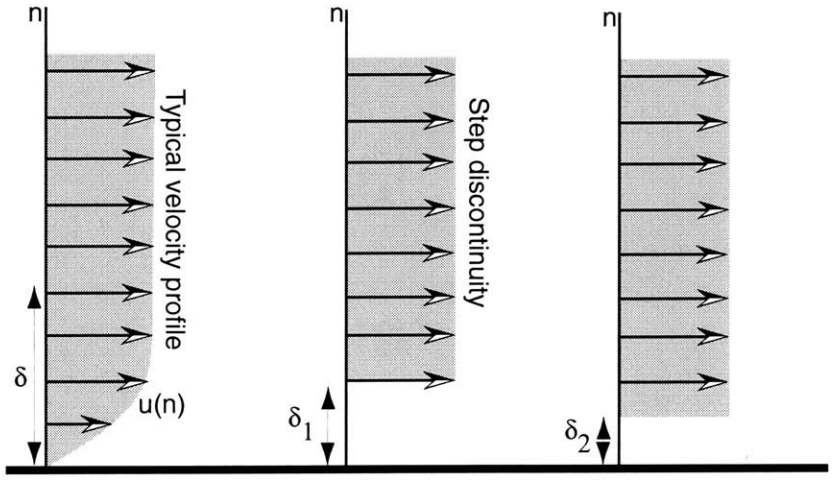

Figure 1-2: Boundary Layer Definitions

created by the viscous layer. The momentum thickness is similarly a measure of the

momentum deficit caused by the viscous layer, and is defined in relation 1.2.

$$\delta_2 = \int_0^\delta \frac{u}{U}(1 - \frac{u}{U})dn \tag{1.2}$$

1.2.2 3D Boundary Layers

Three dimensional boundary layers are much more complex because of the possibility that the flow changes direction through the viscous layer. Figure 1-3 shows a possible boundary layer profile for a three dimensional flow. One way of describing such flows is to calculate the displacement thickness in the free stream flow direction and a displacement thickness normal to this direction, the cross-flow component as described in Schlicting[4]. The equations for the displacement thickness parallel to the free stream velocity is shown in equation 1.3, where $u_{s\delta}$ is the component of the velocity vector in the direction of the velocity vector at the edge of the boundary layer, δ. Similarly, the equation for the cross-flow displacement thickness is shown in equation 1.4, where $u_{n\delta}$ is the component of the velocity vector in normal to the velocity vector at the edge of the boundary layer.

$$\delta_{1parallel} = \int_0^\delta (1 - \frac{u_{s\delta}}{|U|})dz \tag{1.3}$$

$$\delta_{1cross-flow} = \int_0^\delta (1 - \frac{u_{n\delta}}{|U|})dz \tag{1.4}$$

Alternatively, for some geometries, it makes sense to calculate the displacement thickness along perpendicular coordinates that are mapped to a surface. In this case, the definitions for the parallel and cross-flow displacement thickness change to equations 1.5 and 1.6, where x and y are some arbitrary orthogonal vectors, and it is assumed that x is the primary flow direction.

$$\delta_{1x} = \int_0^\delta (1 - \frac{u_x}{|U_x|})dz \tag{1.5}$$

$$\delta_{1y} = \int_0^\delta (1 - \frac{u_y}{|U_x|})dz \tag{1.6}$$

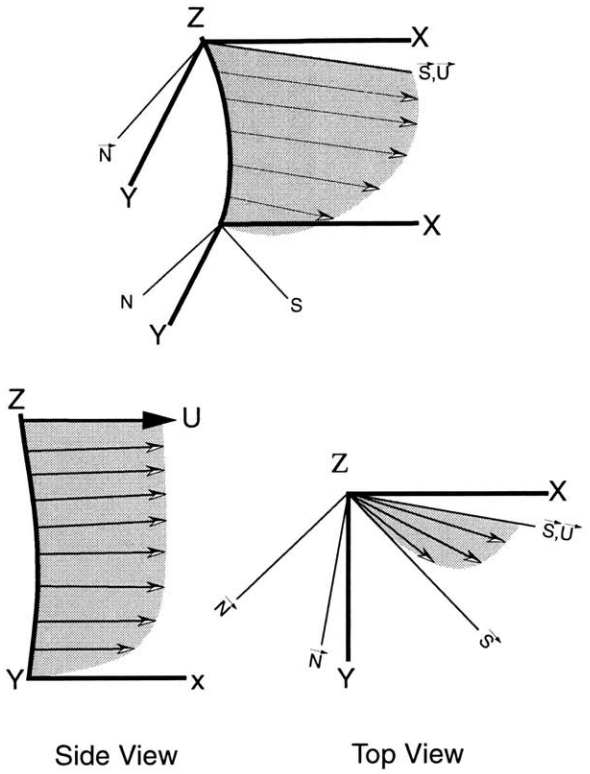

Figure 1-3: Three dimensional boundary layer profiles

For example, figure 1-4 shows a curvilinear coordinate system on the wing that is not aligned with the free stream, but is often used in design.

For very convoluted flows, with the cross-flow component switching from positive to negative sign, the integrated cross flow displacement thickness will not show this effect because some of the negative area cancels the positive area of the integral. The integral may be computed with the absolute value of the crossflow velocity component and compared to the normal calculation of the displacement thickness to determine if this is happening. An alternative way to measure these three dimensional boundary layers is to compute the displacement thickness in the local streamwise direction (equation 1.7) and a twist angle from the wall to the free stream (equation 1.8). This in effect unwraps the boundary layer and makes it two dimensional in the rotated coordinate system.

$$\delta_{1s} = \int_0^{\delta} (1 - \frac{u_s}{|U|}) dz \tag{1.7}$$

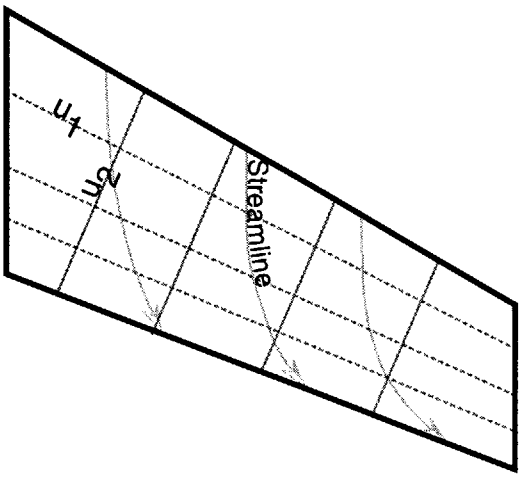

Figure 1-4: Swept wing boundary layer integration coordinates

$$\theta = \int_0^{\delta} (\frac{ds}{dz}) dz \tag{1.8}$$

This turning angle calculation suffers from the same problem as the cross flow integral in equation 1.4 because the angle may change sign from the edge of the boundary layer to the wall. Instead, it may be useful to perform the integral on the absolute value of the change in velocity direction and compare this to the total turning angle.

1.2.3 Flow Blockage

One of the advantages of using the displacement and momentum thickness is that these quantities have some physical meaning in two dimensional flows. However, the definitions loose their meaning for more complex geometries, requiring a redefinition for these new cases. In two dimensional flows, the displacement thickness represents the difference in mass flow rate between the actual viscous flow and a flow without viscosity. However, this assumes the body has an infinite extent out of the plane of flow, without any curvature in this direction. If the wall has curvature normal to the plane of flow, the integral no longer approximates the mass flow deficit. Figure 1-5 shows the situation that is being described. The two dimensional displacement thickness definition produces an elemental displacement volume shown in figure 1-6 that does not follow the wall curvature, but just extends in the z axis. A better approximation is to use the radius of curvature to create a new elemental control

volume. As shown in equation 1.9 the definition for δ_1 can be derived from equating the mass flow rate through an incremental width dz with that obtained by assuming a uniform flow of U_∞ outside of δ_1 and 0 less than δ_1.

$$\frac{\dot{m}}{dz\rho} = \int_0^\delta u(y)dy = \int_{\delta_1}^\delta U_\infty dy \tag{1.9}$$

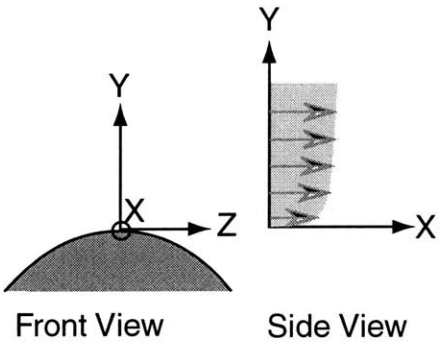

Figure 1-5: Boundary Layer on Curved Surface

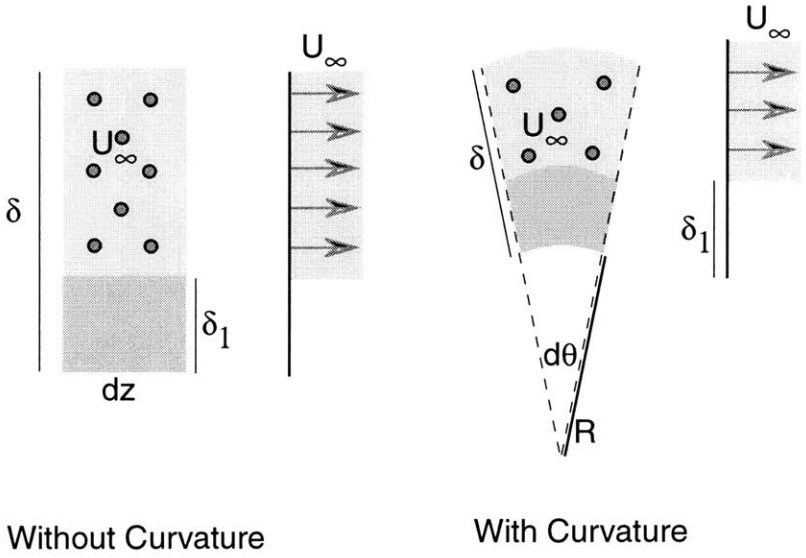

Figure 1-6: 2D vs Curved Approximations

This can be modified for the case of a cylindrical control volume element with a local radius of curvature, R, as shown in equation 1.10

$$\frac{\dot{m}}{d\theta\rho} = \int_R^{R+\delta} u(r)rdr = \int_{R+\delta_1}^{R+\delta} U_\infty rdr \tag{1.10}$$

This yields equation 1.11 for the displacement thickness as a function of the velocity profile and the local radius of curvature.

$$\delta_1 = (+\sqrt{R^2 + \int_R^{R+\delta} (2 - \frac{2u(r)}{U_\infty}) r dr}) - R \tag{1.11}$$

To check that this equation yields the same result as the two dimensional displacement thickness calculation for large radii of curvature, a simple test velocity profile was created and both displacement thickness equations were applied. The velocity profile tested was a linear profile varying from zero at the wall to 1 at the edge of the boundary layer. The thickness calculated for a flat wall is 0.5, while that for the curved wall is shown in figure 1-7. For large radii of curvature, the corrected displacement thickness approaches the two dimensional result, with increasing error in areas of large curvature.

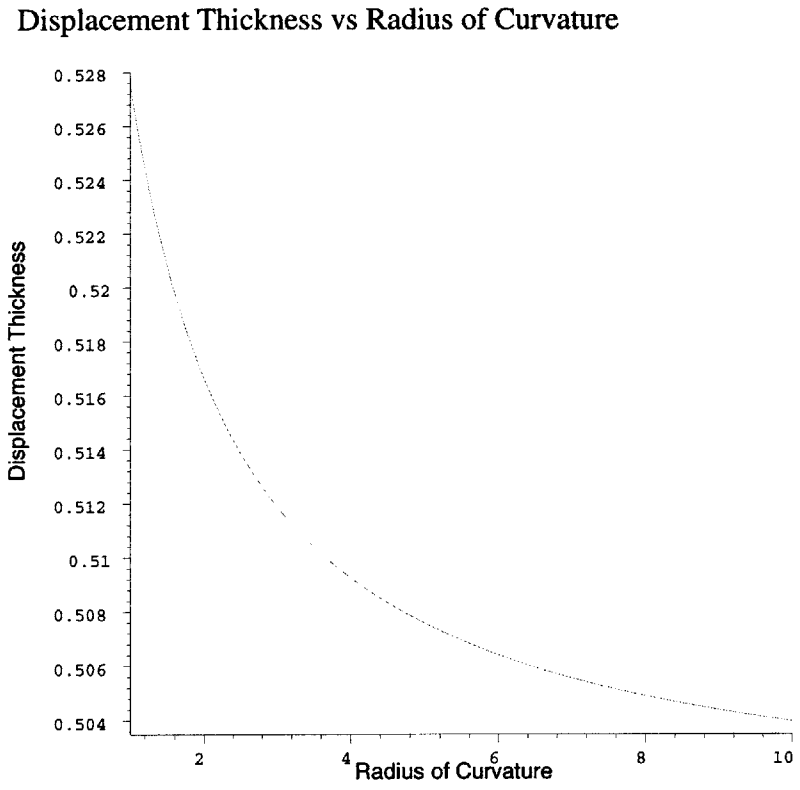

Figure 1-7: Displacement Thickness vs. Radius of Curvature

These results indicate that the displacement thickness as defined by equation 1.1 cannot be used to find the blockage effects of a body in a viscous flow, except in

circumstances where the surface of the body does not have any local radii of curvature comparable to the boundary layer thickness.

Chapter 2

Stationary Shock Wave Detection

The stationary shock algorithm was developed with a knowledge of the shock geometry shown in figure 2-1.

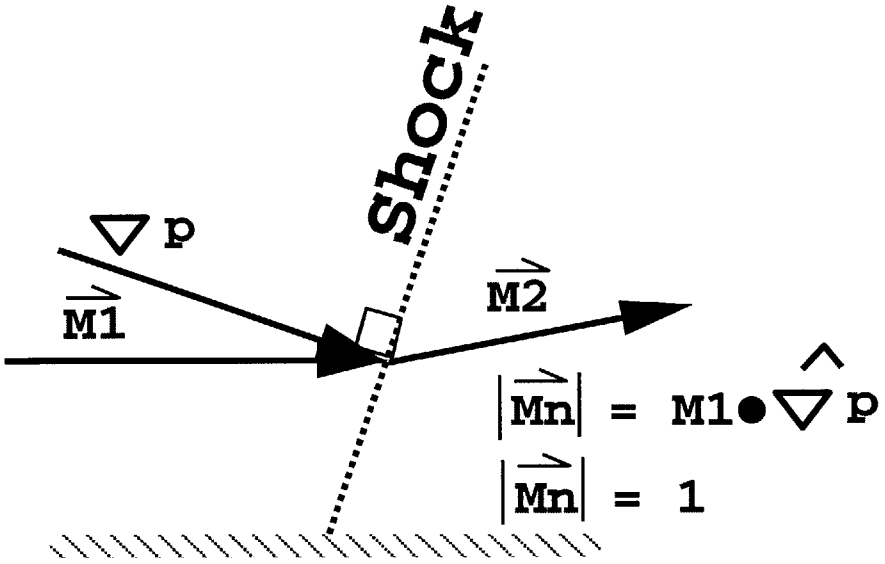

Figure 2-1: Shock detection test quantity

For any shock, the Mach number normal to the shock has a value of at least one just before the shock. This normal Mach number can be computed on each node and used as a test value for determining the shock location. The pressure gradient is always normal to the shock, so it was used to find the shock orientation. The pressure gradient was approximated for each node, and then dotted with the mach vector to

calculate a shock test value at each node. The locations where the test value equals one forms a boundary surrounding the shock location.

This test excludes areas of expansion, since the pressure gradient and the mach vector will have opposite senses, and their dot product will be less than zero.

For three-dimensional models, an iso-surface of $M_n = 1$ was used to visualize the results. The shock feature is surrounded by the $M_n = 1$ iso-surface, and has a thickness associated with it. In the two-dimensional case, contours of the normal Mach number were created, and the $M_n = 1$ curve forms a boundary for a shock region.

2.1 Shock strength

The relative strength of the shock is of interest to designers, as well as its location. Ideally, the shock strength can be represented by the ratio of some invariant flow variable across the shock. $\frac{P_2}{P_1}$ is measure of the shock strength often used to compute the ratio of the other flow variables across the shock. Unfortunately, the calculated shock region does not correspond to the actual extent of the shock. The shock finding algorithm relies on high gradients to mark the boundary of the shock region.

However, near the boundaries of the shock, the pressure and density gradients get smoothed due to viscosity in the real shocks and dissipation in numerical shocks. The result is that the detected shock region will not encompass then entire shock as illustrated in figure 2-2. This means that the pressure ratio across the boundary of the detected shock region will be smaller than the actual pressure ratio across the shock.

A different, more direct approach was used to find the pressure values. The algorithm starts from a node in the shock region and marches in space along the pressure gradient vector. When the pressure is no longer increasing, or is increasing at a very slow rate, then the marching is stopped and the pressure at this point is called P_2. A similar procedure is used to find the upstream pressure, but the stepping now follows the reverse of the pressure gradient vector. The procedure is

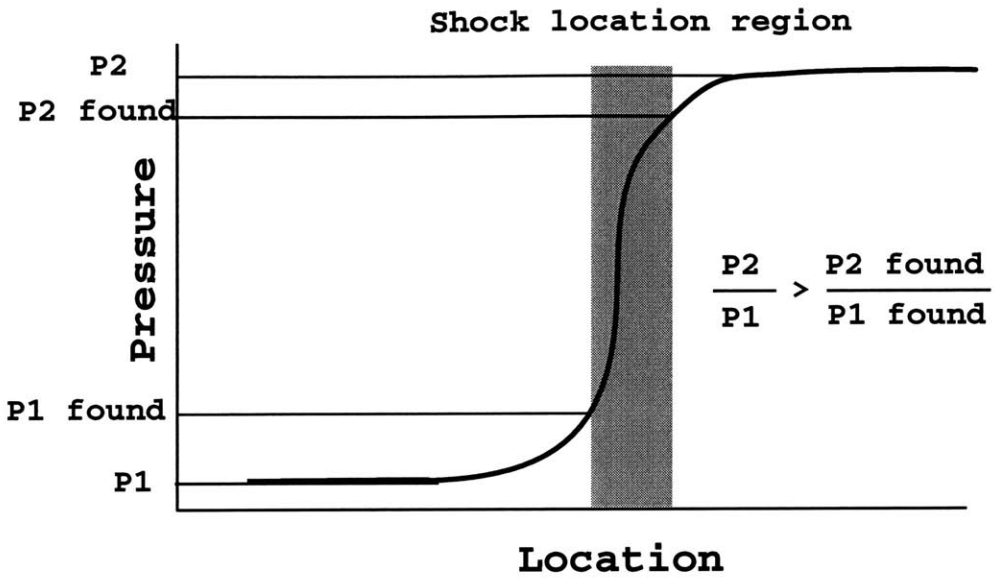

Figure 2-2: Computed vs. actual pressure ratio

computationally expensive, but is more analogous to the way an analyst would find the pressure ratio across the shock; by looking at the graph of the pressure normal to the shock. Fortunately, the number of nodes in the shock region is also relatively small and only covers a width of about three cells for the types of solutions tested, so a calculation of this type is not prohibitively expensive; on the order of the computation needed to calculate the shock test quantity.

The shock strength can be represented by the pressure ratio across the shock, which can be calculated by marching in space along the pressure gradient.

2.2 Shock Classification

Their geometry and relationship to physical objects can classify shock waves. This classification can be made automatically once the shock is located.

One classification that can be easily made is for normal or oblique shocks. All that is needed is the angle of the shock with respect to the local velocity. Since the pressure gradient is normal to shock, a test value can be constructed that is the angle

between the velocity vector and the shock surface with the equation 2.1.

$$\arccos\left(\bigtriangledown P \cdot \vec{q}/q\right) \tag{2.1}$$

The only difficulty with this test quantity is that it will change across an oblique shock because the velocity vector direction changes across the shock.

Another classification that can be made is whether the shock is attached (or not) to an object. In this case, it is necessary to see which geometric objects intersect the shock region. If the shock is not attached to a solid surface, then it is a detached shock. This paper does not cover any algorithms to coalesce the shock areas into distinct regions, but clearly this is possible by employing a flood algorithm. Then each shock could have a geometric description, a strength value, an angle, and (if it is a transient model), an associated speed. Unfortunately, it is not always clear how to display the angle and strength values in a meaningful way. For the three-dimensional cases, the angle and strength values were painted on the shock iso-surface, which produced some easily understood results. However, in the two-dimensional case, presenting contours of the strength and angle does not convey the information appropriately. These are single scalar values at a few isolated nodes, and having contours between them and the surrounding areas that do not have values does not make sense. A better method might be to put the numerical values on the shock contour itself.

With a few simple operations, the shocks can be easily classified once located.

2.3 Grid Study

The supersonic ramp test case had the geometry of figure 2-3. The shaded area is the region of the model that was used to plot the results and grids. Three different uniform grids were generated for the same geometry to determine the sensitivity of the detector to grid size. Figure 2-4 shows the three grids that were used for the experiment.

The results of the three runs were similar except for the thickness of the indicated

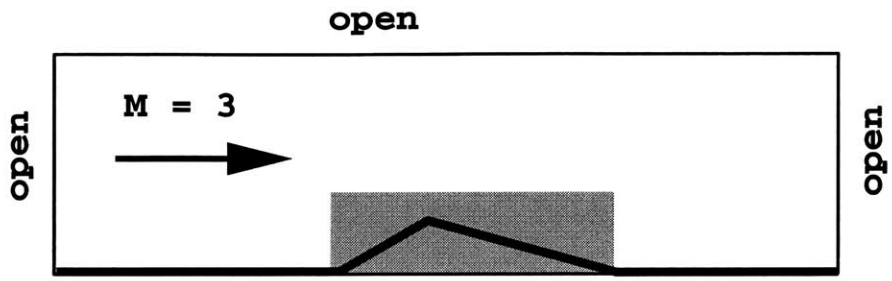

Figure 2-3: Ramp model

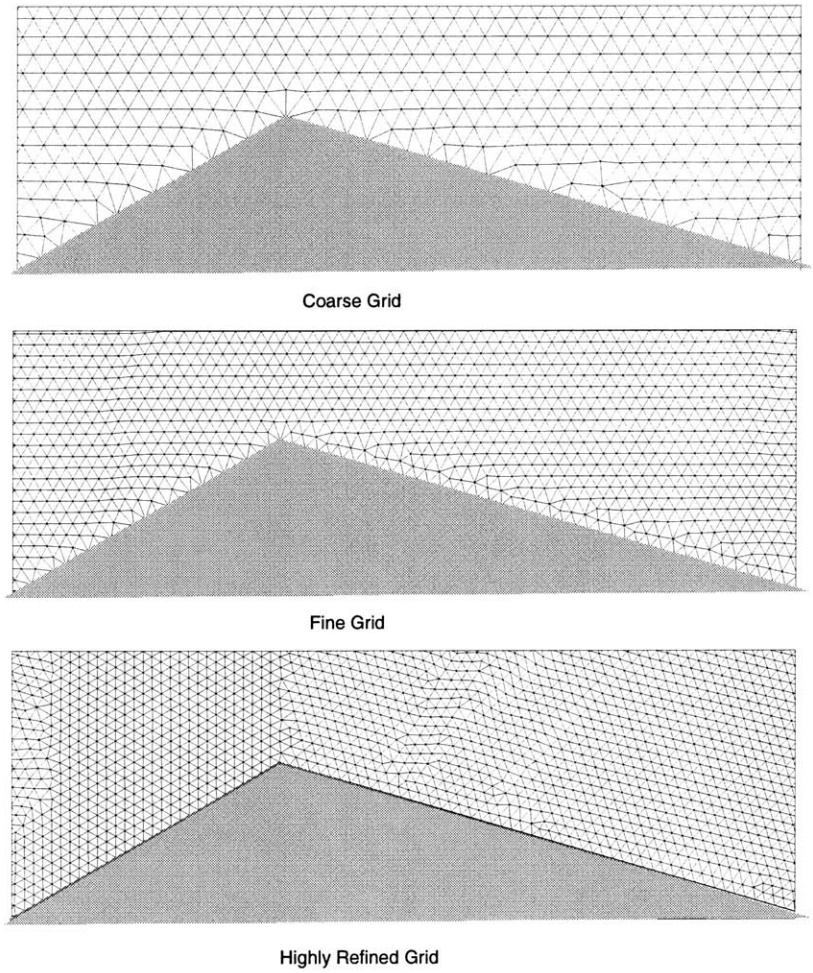

Figure 2-4: Grid Refinement On Wedge Model

shock. The larger the element size, the larger the indicated shock. Figures 2-5, 2-6 and 2-7 are contour plots of the normal Mach number, starting at $M_n = 1$ in the region of the wedge.

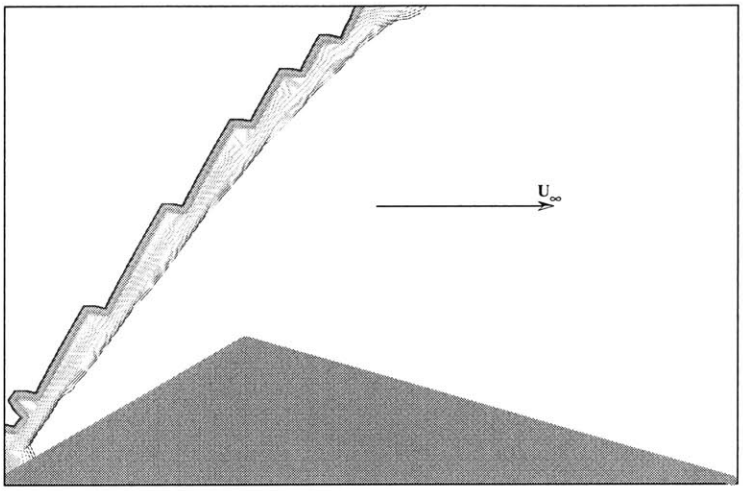

Figure 2-5: Shock contours on the coarse grid

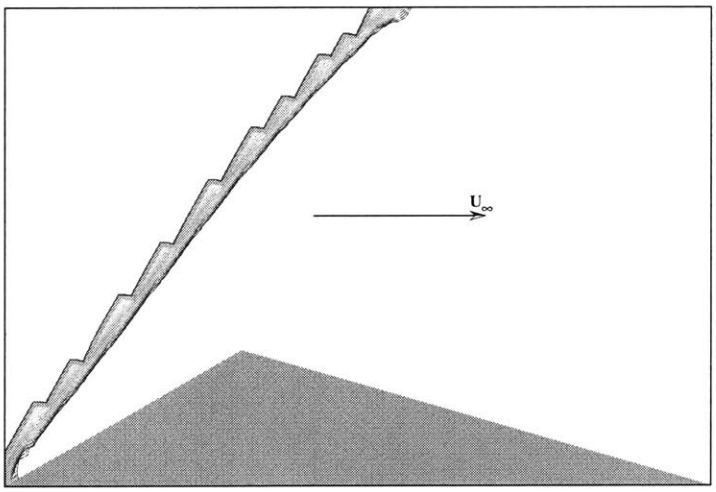

Figure 2-6: Shock contours on the more refined grid

The results in table 2.1 show that the shock algorithm displays shock thickness as a linear function of element size. The shape of the shock region not only locates the shock, but also can point to a lack of mesh refinement in the area.

The numerical model used to solve the problem also greatly effects the shape of the shocks. Some CFD solution algorithms are better suited to capturing the sharp

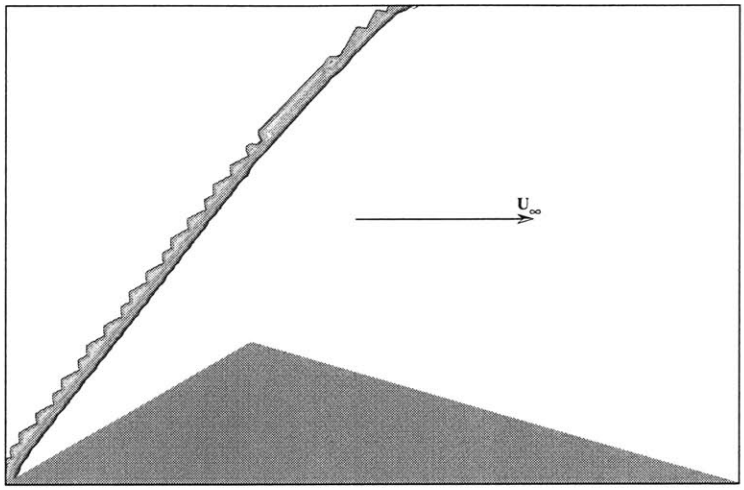

Figure 2-7: Shock contours on highly refined grid

Number of elements	Shock thickness (num cells)
5272	3
13801	3
20942	3

Table 2.1: Grid study results

discontinuities. The larger the effective dissipation, the more spread out the shock and the more cells involved.

2.4 Supersonic projectile

The same shock finding algorithms were applied to the results of a much larger three-dimensional viscous solution; a projectile in a Mach 1.2 flow. The image in figure 2-8 shows the shock iso-surface painted with the calculated pressure ratio. The grid is only refined near the body, so the shock appears jagged at any distance from the body. The highest pressure ratio occurs at the center of the oblique shock just in front of the nose, and has a value of 1.5.

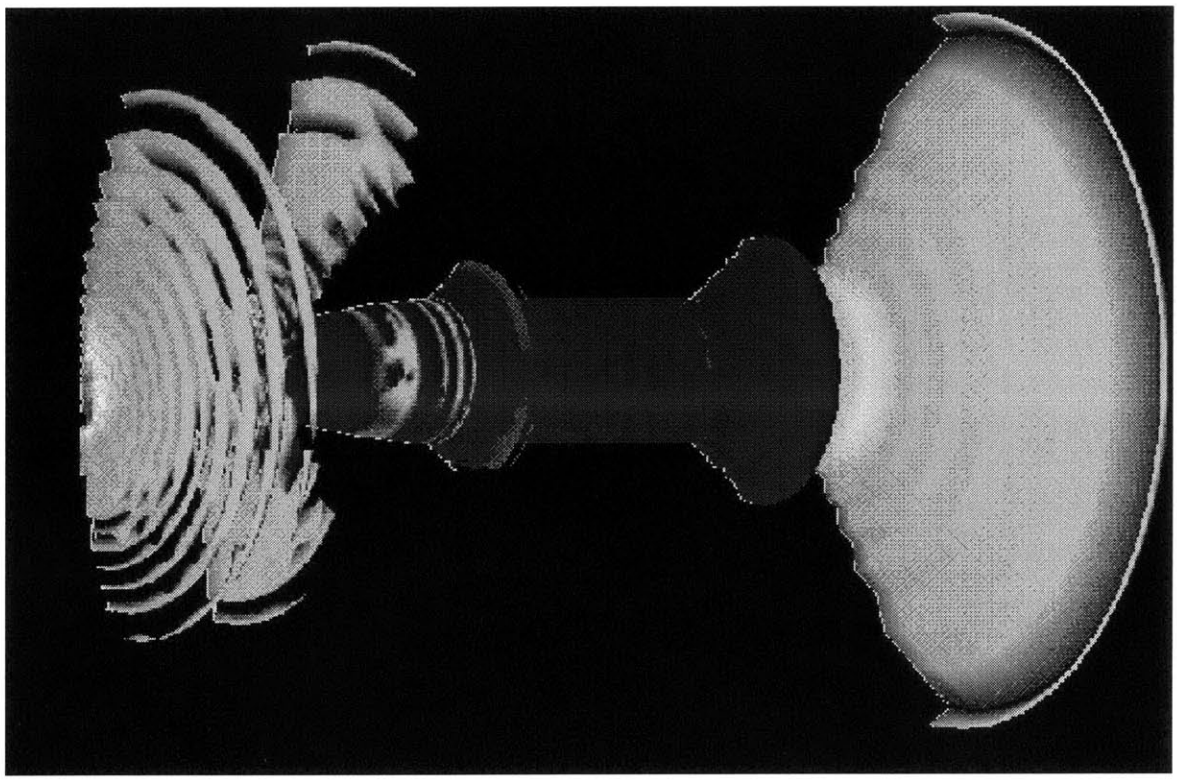

Figure 2-8: Three dimensional shock representation on a projectile model in mach 1.2 flow

Figure 2-9 shows a two dimensional slice of the same model. A couple of features appeared that were somewhat puzzling. Note that there was an indicated shock after the first bend on the top of the shell, which should really be followed by an expansion.

Closer examination of the pressure gradient magnitude shown in figure 2-10 shows that there is an expansion immediately following the turning, then a sudden increase in pressure that the shock finder has picked up. This filter is not picking up the expansion waves.

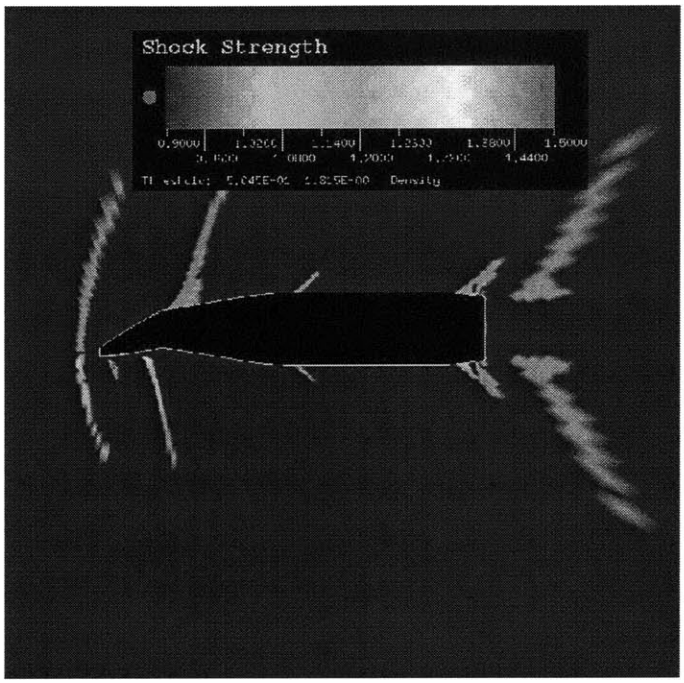

Figure 2-9: Shock strength false color image

The shock algorithm picked out the bow shock and compressive bend at the bottom front of the shell, but also detected some other interesting features. In fact, the designers of the projectile are still arguing over the cause of these compressions after the initial expansions.

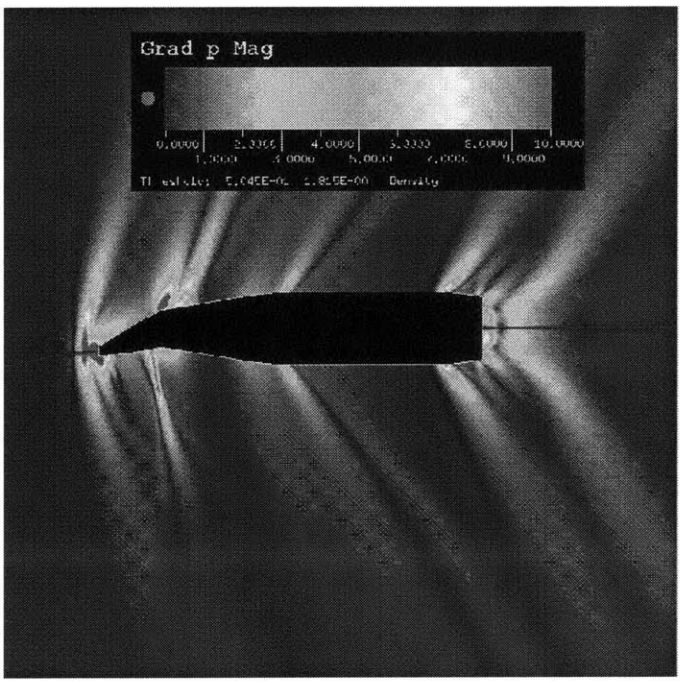

Figure 2-10: Pressure gradient magnitude

Chapter 3

Transient Shock Wave Detection

The assumptions made in constructing the previously described shock finding technique no longer apply when the shock is moving. To locate a shock with the previous method, it is necessary to assume that the observer is traveling with the shock and all velocities are measured with respect to this translating frame of reference. However, since all velocities are calculated in the model frame, there has to be a correction applied to the test equation to account for the moving shock. The equation 3.1 shows what this term must be, basically a time derivative of the pressure.

$$\frac{1}{|\bigtriangledown P|}\frac{1}{a}\frac{Dp}{Dt} = \frac{1}{|\bigtriangledown P|}\frac{1}{a}\frac{dp}{dt} + \frac{\vec{M}\cdot\bigtriangledown P}{|\bigtriangledown P|} \tag{3.1}$$

It is more computationally expensive to approximate time derivatives directly, since that would require the storage of multiple time steps. So, the time derivative of pressure was calculated based on relations that equate it to a spatial variation of the state variables. Equation 3.2 applies to isentropic flows.

$$dp = a^2 d\rho \tag{3.2}$$

This equation is then used along with the conservation of mass equation to produce

an equation for an invariant test quantity that can be used to locate moving shocks.

$$\frac{dp}{dt} = -a^2 \bigtriangledown \cdot(\rho\vec{q}) \tag{3.3}$$

From equations 3.2 and 3.3, equation 3.1 becomes:

$$\frac{1}{\mid \bigtriangledown P\mid}\frac{1}{a}\frac{Dp}{Dt} = -a\frac{1}{\mid \bigtriangledown P\mid} \bigtriangledown \cdot(\rho\vec{q}) + \frac{\vec{M}\cdot\bigtriangledown P}{\mid \bigtriangledown P\mid} \tag{3.4}$$

A shock is then located when this quantity equals or exceeds one.

In the general case, pressure can be related to the internal energy and velocity of the flow with equation 3.5.

$$p = (\gamma - 1)[\rho E - \frac{1}{\rho}(\rho\vec{q})\cdot(\rho\vec{q})] \tag{3.5}$$

Taking the time derivative of this quantity will yield the required correction term, equation 3.6.

$$\begin{aligned}\frac{dp}{dt} &= (\gamma-1)[\frac{d}{dt}(\rho E) - \\ &\quad \vec{q}\cdot\frac{d}{dt}(\rho\vec{q}) + \frac{1}{2}q^2\frac{d\rho}{dt}]\end{aligned} \tag{3.6}$$

Substituting equation 3.3 into equation 3.6, and replacing the time derivatives with their equivalents from the mass and momentum equations yields equation 3.7.

$$\begin{aligned}\frac{dp}{dt} &= (\gamma-1)[-\bigtriangledown\cdot(\rho\vec{q}H) + \\ &\quad \vec{q}\cdot(\bigtriangledown P + \bigtriangledown\rho\vec{q}\vec{q}) - \frac{1}{2}q^2\bigtriangledown\cdot(\rho\vec{q})]\end{aligned} \tag{3.7}$$

This is the generalized correction term needed for transient problems.

3.0.1 Translating normal shock in a tube

A model of a moving normal shock in a channel was created to investigate the behavior of the shock finding algorithm and the effect of the transient modification. Two

separate runs were done, the first had the initial conditions shown in the figure 3-1.

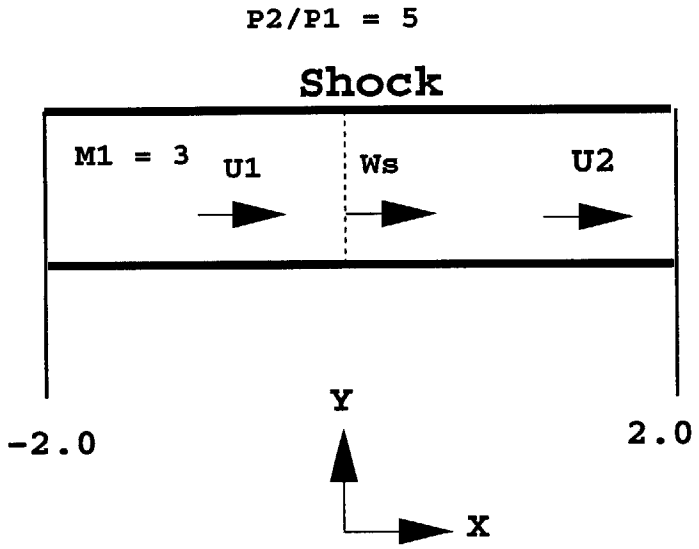

Figure 3-1: Transient Shock Model

Shock relations were used to set up the initial conditions for the model. The formulas for moving normal shock waves with constant C_p and C_v were applicable in this case. However, these formula assume that the upstream speed, U_1 is 0, so a correction had to be made to produce the correct initial conditions for the flow. For the first run, the pressure ratio was chosen to be less than the pressure ratio required for a standing shock in M=3 flow (10.33). This required that the shock move toward the right in the positive X direction. The speed of the shock traveling into a stationary fluid, W, was calculated with the equation 3.8. Since the upstream velocity was not zero, the actual speed of the shock had to be corrected with equation 3.9.

$$W = a_1\sqrt{\frac{\gamma+1}{2\gamma}(\frac{P_2}{P_1}-1)+1} \tag{3.8}$$

$$W_s = U_1 - W \tag{3.9}$$

The shock test scalar was calculated with the isentropic transient correction equation (equation 3.4), that was simplified for this particular example. The Y component of velocity was assumed to be zero in this case, so the divergence term simplified to

the following.

$$\frac{1}{|\bigtriangledown P|}\frac{1}{a}\frac{Dp}{Dt} = -a\frac{1}{|\bigtriangledown P|}(\frac{d}{dx}u\rho) + \frac{\vec{M}\cdot\bigtriangledown P}{|\bigtriangledown P|} \tag{3.10}$$

The derivative of the density times the X velocity was then expanded, yielding the final equation.

$$\frac{1}{|\bigtriangledown P|}\frac{1}{a}\frac{Dp}{Dt} = -a\frac{1}{|\bigtriangledown P|}(\frac{du}{dx}\rho + \frac{d\rho}{dx}u) + \frac{\vec{M}\cdot\bigtriangledown P}{|\bigtriangledown P|} \tag{3.11}$$

Results indicated that the pressure variation across the shock has some interesting features that are problematic for the shock finding algorithm. The shock started at X=0, and is moving to the right in the positive X direction. As it moves, the shorter wavelengths that makeup the initial discontinuity move at a slower speed than the longer wavelengths. This difference in speed is a numerical artifact of the time stepping method used in the CFD solver. As time progresses, high frequency pressure oscillations show up behind a moving shock, as shown in the figure 3-2.

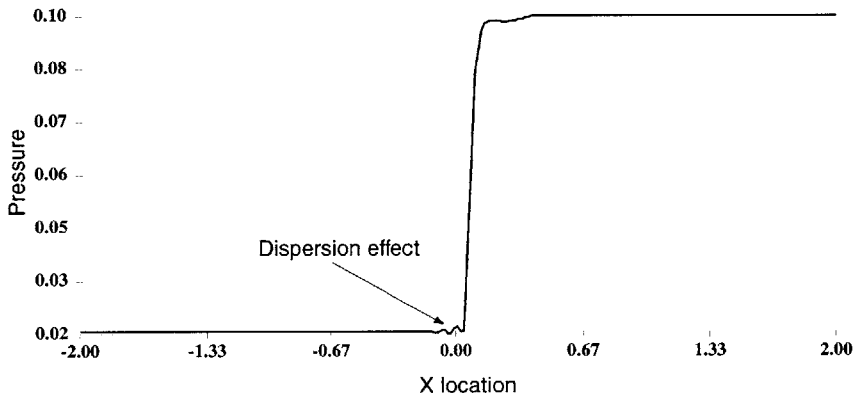

Figure 3-2: Pressure Distribution

Figure 3-3 is a plot of the shock scalar with the isentropic transient correction. A filter has been applied to eliminate the pressure gradients caused by dispersion. The dashed line on this and following figures represents the threshold for a shock. Everything above one is marked as a shock region.

Figure 3-4 is a plot of the same quantity after a few more iterations. The shock

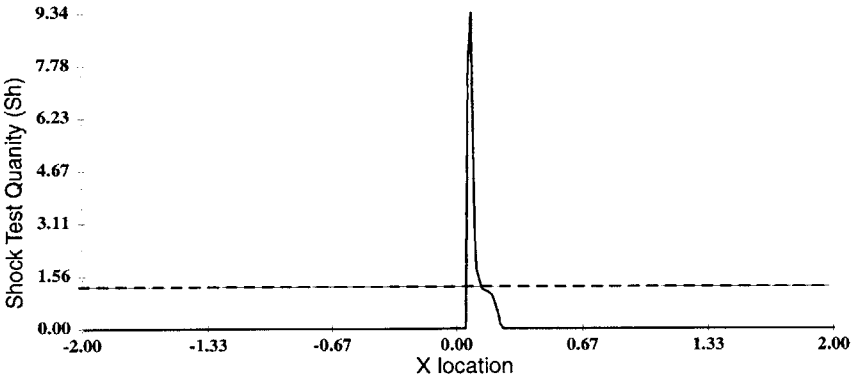

Figure 3-3: Shock Scalar

is clearly moving to the right, as expected.

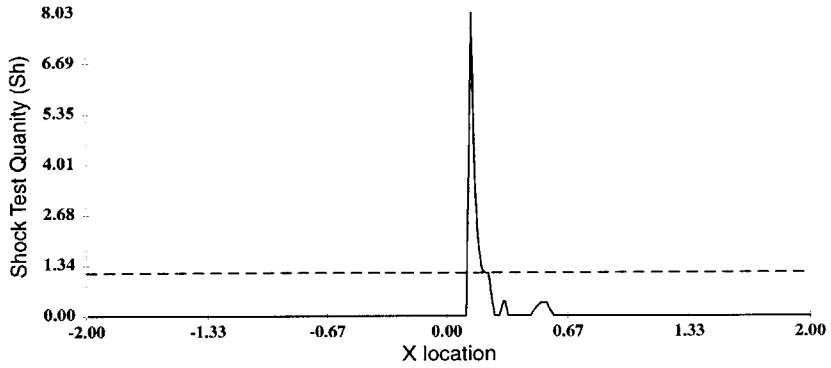

Figure 3-4: Shock Scalar at δt

The results of this experiment point to the importance of choosing a threshold value for the magnitude of the pressure gradient. Because of the slower wave speeds of the higher frequency pressure waves, oscillations in the pressure gradient take place behind the shock. These pressure gradient increases are enough to skew the results and show up in the shock detection values as a group of shocks behind the actual position as shown in figure 3-5.

From the above experiment, it was noted that it did not matter if the transient correction was used or not, a shock would still be indicated. This was because the upstream Mach number was greater than one, making the uncorrected normal Mach number greater than one. A change in initial conditions was made to see what happens

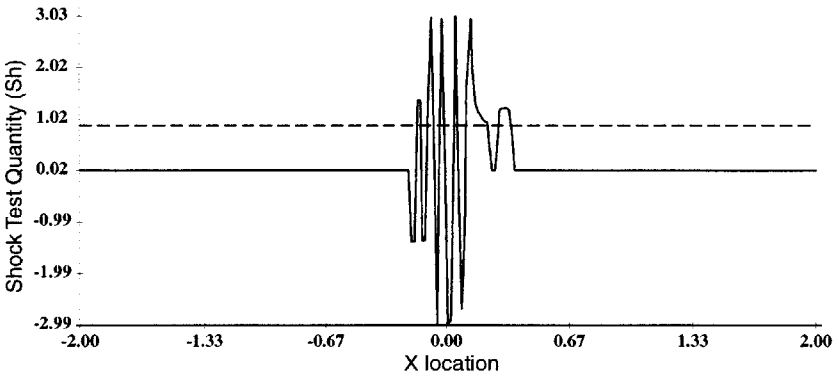

Figure 3-5: Shock scalar with unfiltered pressure gradient

when the upstream Mach number is less than one. The upstream Mach number was set to 0.9, and the pressure difference was set to 3.0, which will produce a normal shock moving in the negative X direction of figure 3-1.

The results of applying these boundary conditions are shown in the following figures. In figure 3-6, the normal Mach number is plotted against the model x coordinate. The normal Mach number never exceeds unity, which by the previous test indicates that no shock is present in the flow. However, the shock test scalar in figure 3-7 does exceed unity at the shock, indicating that the shock is indeed present. The correction term has made it possible to locate the shock.

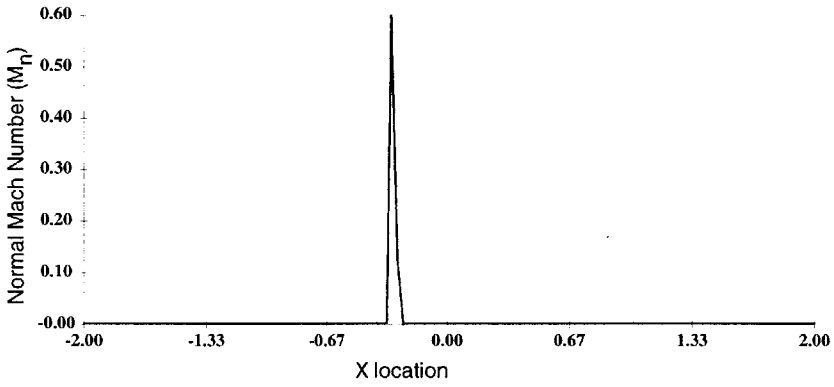

Figure 3-6: Normal Mach Number vs. Location

The experimental results were then compared to the theoretical location of the shock at any given time, calculated with the following equation, where x is the loca-

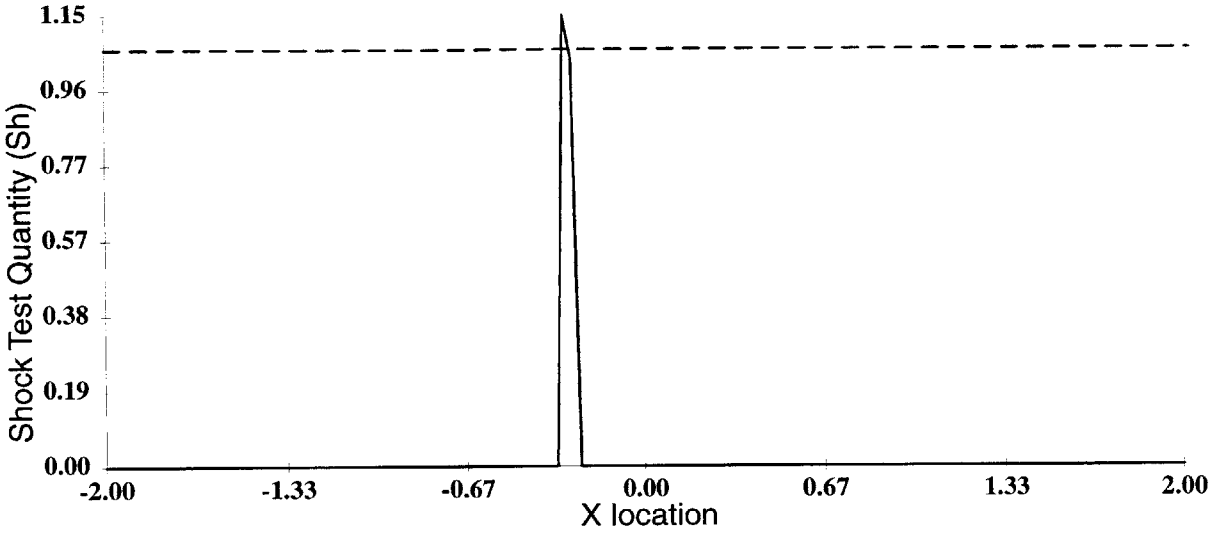

Figure 3-7: Shock scalar vs. Location

tion, t is time and W_s is calculated with equations 3.8 and 3.9.

$$X = W_s t \tag{3.12}$$

Figure 3-8 is a plot of the difference between theoretical and measured shock location vs. time.

The experimental shock location was measured two ways, first by the location of the maximum pressure gradient magnitude, and secondly by central location of the shock region.

Since the shock region actually covers about 3 cells in width, or 0.09 units, the theoretical shock location and pressure gradient maximum both occur well within the region at all times.

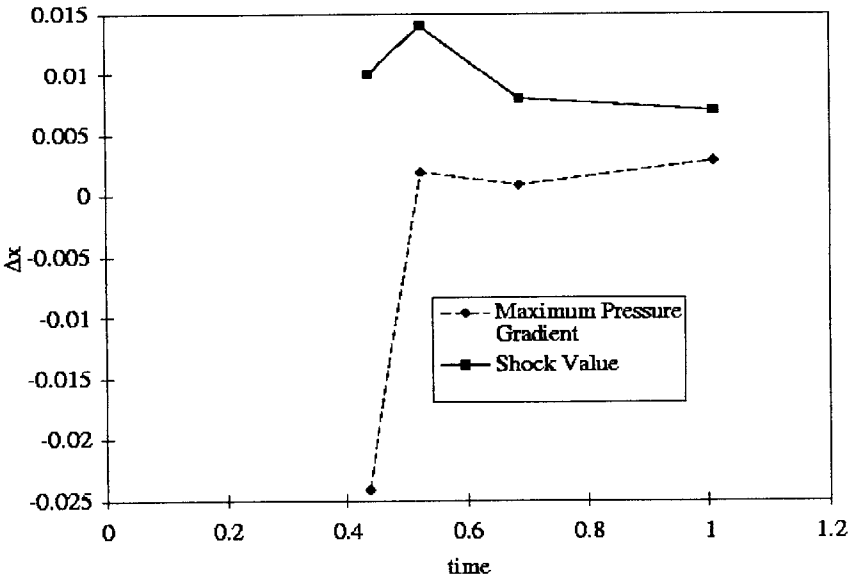

Figure 3-8: Theoretical vs. Experimental Shock Location

Chapter 4

Filtered Shock Detection Results

The previous results show that this shock finding algorithm produces some falsely indicated shock regions. This is partially due to small numerical errors in the gradient away from the shock. As the gradient of pressure goes to zero in the far field, errors in the shock test function build as shown in the following equation, where δ is a small variation in the quantity.

$$\frac{M_n(\bigtriangledown P + \delta \bigtriangledown P)}{|\bigtriangledown P + \delta \bigtriangledown P|} \rightarrow \frac{\delta \bigtriangledown P}{|\delta \bigtriangledown P|} \rightarrow O(1) \tag{4.1}$$

To remove these false indications, three filtering techniques have been applied to the problem. The techniques start with an iso-surface constructed where the value of the shock test scalar is 1.0 and they reject a subset of the triangles that makeup that surface. The first technique enforces the property that the pressure gradient is normal to the shock surface. This technique removes all shock surface triangles that do not pass the test in the following equation, where n is the normal of the surface triangle, and c is a threshold value between 0 and 1.

$$\frac{|\bigtriangledown P \cdot n|}{|\bigtriangledown P|} \leq c \tag{4.2}$$

The second technique removes all iso-surface triangles that fall below a certain pressure gradient magnitude threshold. This technique is based on the fact that shock

discontinuities should only occur in regions of relatively high gradients. The problem is to determine the meaning of a 'relatively' large gradient and set an appropriate threshold. To accomplish this, all the triangles were divided into groups based on the value of the pressure gradient magnitude at their centers. The count of triangles in each group forms a curve. The threshold was chosen where the derivative of this curve goes to zero. This method of setting a threshold assumes that the actual shock surface is located in a region of high gradients and that changing the threshold by some small amount will not change the number of triangles in the surface.

Note that setting a pressure gradient magnitude threshold can be done before the shock iso-surface is constructed by applying the filter to the nodal shock scalar values. If the node does not pass the pressure gradient magnitude test, the shock value can be set to 0. Applying a filter to the nodal values has the advantage of producing a more connected shock surface, without disjoint triangles missing.

A third technique removes all the triangles that do not have jumps in density and temperature that correspond to normal shock relations. For a moving normal shock, equations 4.3 and 4.4 state the relationships between the pressure jump across the shock and density and temperature ratio, respectively.

$$\frac{\rho_2}{\rho_1} = \frac{1 + \frac{\gamma+1}{\gamma-1}\frac{p_2}{p_1}}{\frac{\gamma+1}{\gamma-1} + \frac{p_2}{p_1}} \tag{4.3}$$

$$\frac{T_2}{T_1} = \frac{p_2}{p_1}\frac{\frac{\gamma+1}{\gamma-1} + \frac{p_2}{p_1}}{1 + \frac{\gamma+1}{\gamma-1}\frac{p_2}{p_1}} \tag{4.4}$$

The difficulty with this filtering technique is that the extent of the shock needs to be known before hand, so that the pressure, temperature and density ratios can be accurately measured. To overcome this problem, a number of measurements of the pressure temperature and density were made on both sides of the surface triangles, then the two measurements that best fit the shock relations were used to determine if the triangle should be rejected. A fitness function was constructed that, given the measured pressure ratio at two points on either side of the triangle, compares the measured temperature ratio to the temperature ratio computed with equation 4.4

and the measured density ratio with the computed density ratio of equation 4.3 and produces a value of 1.0 in the case where the measurements match theory, and less than 1.0 otherwise.

$$f(p_1, p_2, T_1, T_2, \rho_1, \rho_2) <= 1.0 \tag{4.5}$$

If none of the points on either side of the triangle can produce a fitness value of greater than some threshold, the triangle is removed.

To compare the filtering techniques, a measure of difference between the shock test value fields was constructed. The comparison works from a baseline that is assumed to be the actual shock, then the comparison is run against the results of the unfiltered algorithm and the solution with the various types of filtering. The difference measure is constructed by gathering the centerpoints of all the triangles in the shock surface, F, then all the points that have a shock value greater than 1 in the baseline and test solution are removed from F. The total difference value is the sum of the absolute value of the difference between the values of the baseline and test solution at the points in C. The final comparison function takes the total difference and divides it by the final number of triangles in the shock surface.

$$C = F - B \bigcap F \tag{4.6}$$

Figures 4-1, 4-2, and 4-3 show the results of applying some of the filtering techniques, and why they are necessary. In this case, the solution being examined is an

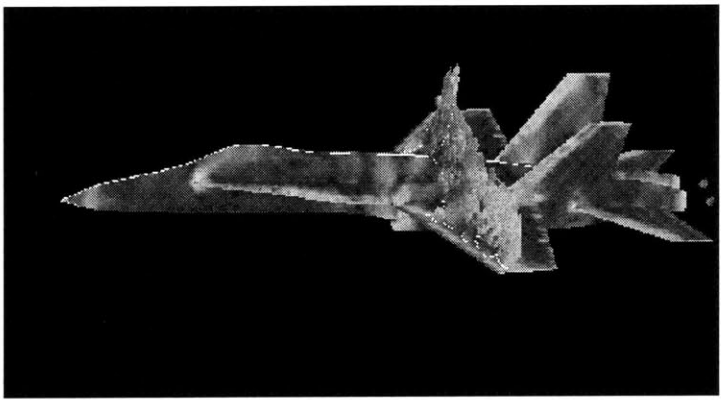

Figure 4-1: Stationary shock algorithm applied to converged solution

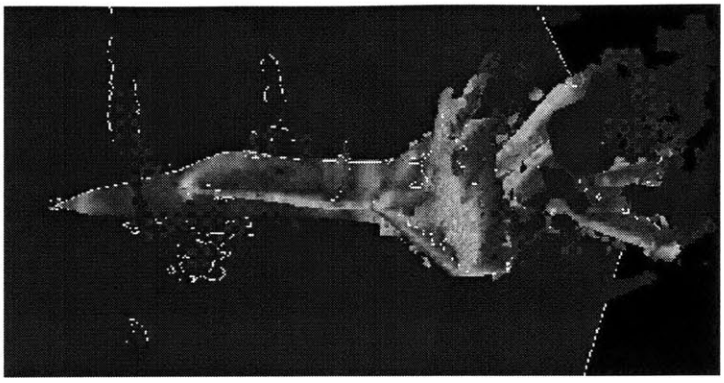

Figure 4-2: Transient shock algorithm without filtering

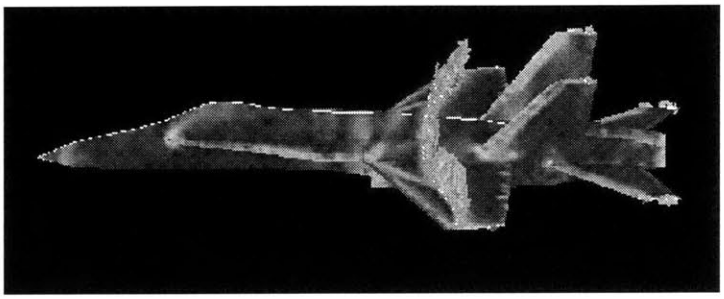

Figure 4-3: Transient shock algorithm with pressure gradient magnitude filter

inviscid converged flow on a 300,000 element f18 aircraft model traveling in subsonic flow. Because the solution has run to convergence, the stationary and transient shock finding algorithms should produce the same results, which as figure 4-2 shows, is not the case. The transient algorithm generates noise and false indications. However, these false signals can be removed with filtering to produce a shock surface that is very similar to the stationary shock finding results. Figure 4-3 shows the results of running the transient shock finder through a pressure gradient magnitude filter.

Table 4.1 is a collection of the results from passing the transient shock finder through various combinations of the three filtering algorithms. The results in table 4.1 indicate that the pressure gradient magnitude filter alone is better than when used in combination with the other two. This became more evident in looking at the graphical output, where there would be a fairly continuous shock surface at the end of the pressure gradient magnitude filter, with some additional outliers. Applying the normal filter or jump condition filter to these results did not get rid of the outliers, but only removed some of the surface triangles enclosing the shock region, making the

test case	Comparison function value
no filtering	0.57
$\mid \nabla P \mid$ filter	0.105
$\mid \nabla P \mid$ and normal filter	0.223
$\mid \nabla P \mid$ and jump filter	0.104
jump filter	0.567

Table 4.1: Filtering study results

final result worse than the result from the pressure gradient magnitude filter alone.

4.1 Transonic Aircraft

The transient modifications were tested on a relatively large model (1 million elements) of an aircraft traveling in transonic conditions (mach 0.85) to see if the unsteady shock finding algorithm could produce useful results on a realistic model. Figure 4-4 shows the results of applying the steady state shock finding algorithm to the converged solution. An iso-surface has been constructed where the normal Mach number equals one, and this iso-surface is painted with the pressure gradient magnitude as an indication of the shock strength. Note that the thickness of these shock regions is quite small due to the highly refined mesh. Figure 4-5 is of the same model, but the iso-surface is now plotted on the results from the unsteady shock algorithm.

Since the solution has converged, the unsteady and steady shock results should be identical. While this was true of the larger shock features, the unsteady algorithm also produced some false indications. It was necessary to threshold out these regions with the pressure gradient magnitude. Even when this was done, some false indications remained, especially at the leading and trailing edges of the wing. This result was in agreement with the one-dimensional results, where it was also necessary to filter out the gradients caused by dispersion in the results.

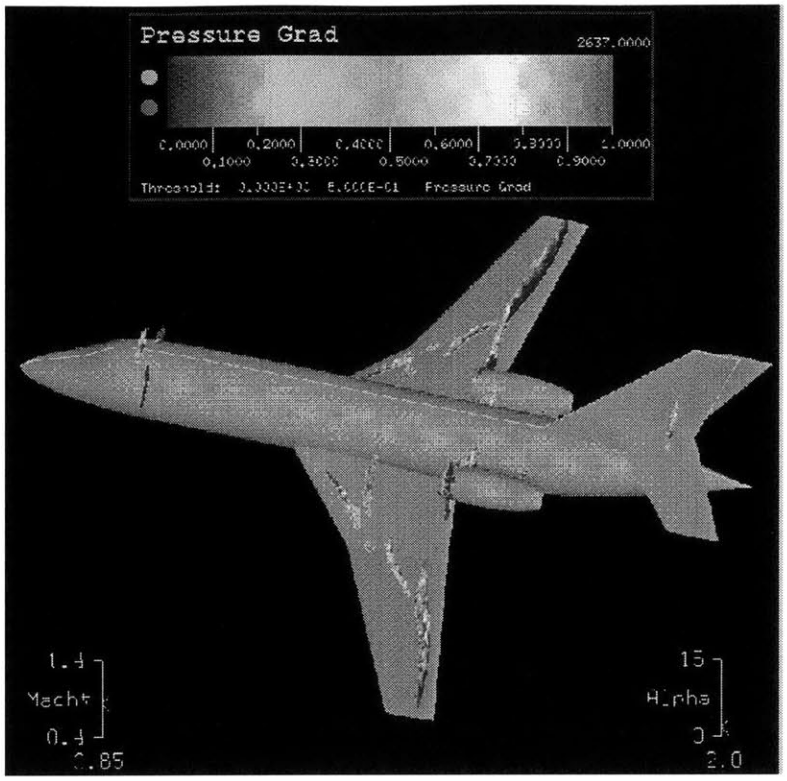

Figure 4-4: Shock detection algorithm applied to a Euler solution of an aircraft model

The shock finder captured some fairly complex shock structures that would be difficult to find almost any other way.

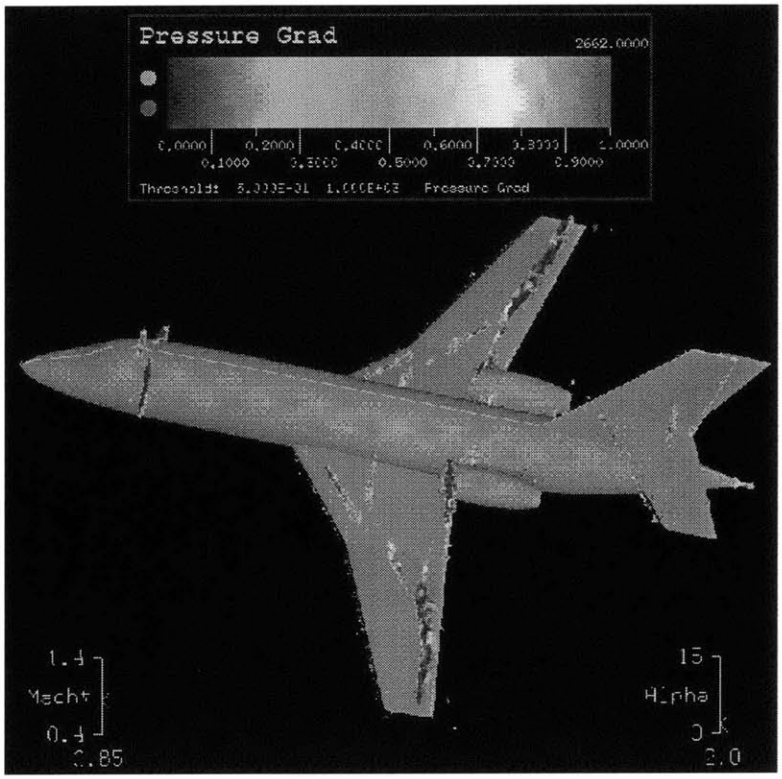

Figure 4-5: Unsteady shock detection algorithm applied to a euler solution of an aircraft model

Chapter 5

Boundary Layer Detection

This chapter presents the basic algorithm that was developed for determining the boundary layer thickness, as well as a more formal discussion of the different boundary layer measures and their characteristics. Later chapters are devoted to applying the algorithm to various velocity profiles from exact solutions of the boundary layer equations. In these test cases, the theories were applied analytically to see if they would be valid for the velocity profile of the solution. Then any difference between the analytic and numerically obtained results was investigated. Even if the boundary layer thickness was determined exactly using analytic means, it is important to know how discretization introduces error into the calculation. Ideally a CFD solution has 10-20 points in the boundary layer, so if a numerical method cannot resolve the boundary layer thickness with information from these few points it is essentially useless, even though it may give exact answers for an analytic, smooth velocity profile.

5.1 Boundary Layer Definition

The algorithms developed here try to determine a characteristic boundary layer thickness, but what is that exactly? In general, the boundary layer is the region in the neighborhood of a solid body where high velocity gradients and boundary conditions on the body make viscosity influence the flow, while outside of this region viscosity may be neglected. It can be shown that the characteristic thickness of this region is

related to the square root of the Reynolds number, and for flows of engineering interest, this makes the boundary layer thickness very small; on the order of a percent of the characteristic length of the flow. With this in mind, it is possible to get an idea of the geometry of the boundary layer on a solid body. The picture becomes that shown in figure 5-1, where the curvature of the wall becomes large relative to the boundary layer thickness, and the local normal varies slightly in the streamwise direction. Neglecting three-dimensional effects, the velocity magnitude goes from zero up to a "free stream" value where it is no longer affected by viscosity. This "free stream" velocity is not necessarily the velocity far from the body, but the velocity just outside the region where viscosity has an influence. So, if one knows the free stream velocity, the boundary layer thickness can be defined as the location along the normal where the velocity is some percentage of the free stream velocity like $\frac{u}{U} = 0.99$ or $\frac{u}{U} = 0.95$. Unfortunately, the way to define free stream velocity is to find the velocity outside of the boundary layer, making a circular argument for finding the boundary layer thickness. What if the flow equations could be solved on the same geometry, but with a

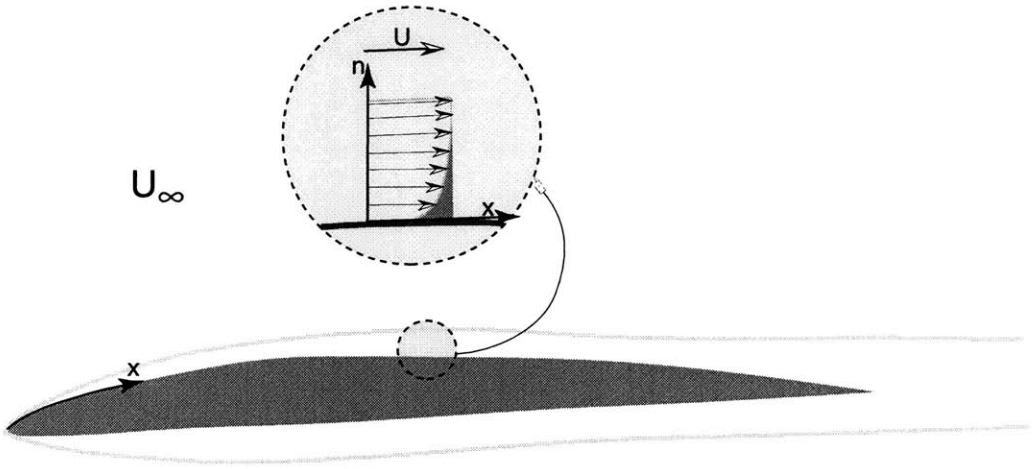

Figure 5-1: Typical boundary layer profile

zero viscosity? Would the velocity at any point on the surface in the inviscid solution be the free stream velocity? Well, the short answer is no, not for all cases. Imagine the problem of fully developed incompressible laminar flow in a channel between two points as shown in figure 5-2. The mass and momentum balance equations for this

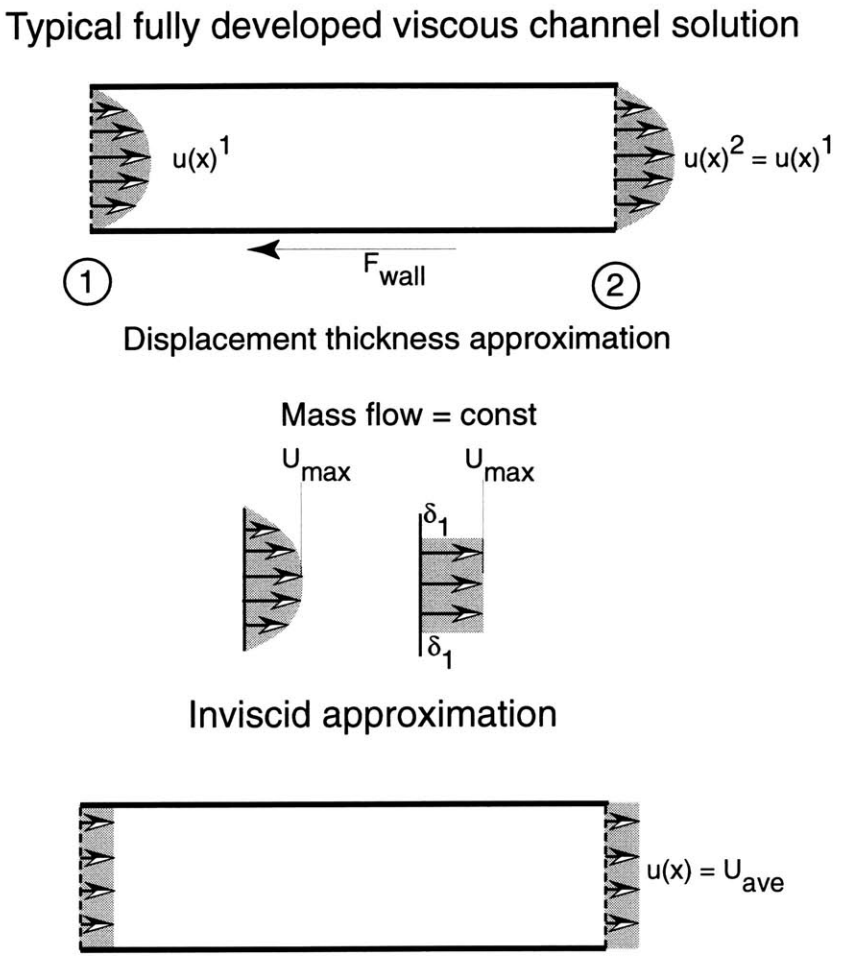

Figure 5-2: Cannel flow viscous and inviscid solution

flow are shown in the equation 5.2.

$$\int_0^L u_1 dy = \int_0^L u_2 dy \tag{5.1}$$

$$\rho \int_0^L (u_2^2 - u_1^2) dy = (p_1 - p_2)L - F_{wall} \tag{5.2}$$

Since this is a fully developed flow, u is not a function of x, therefore the pressure difference from station 1 to 2 balances the shear force exerted by the wall. Compare this solution to a problem with the same boundary conditions, but without viscosity and shear stress. Without the shear stress term and given a finite pressure difference, the flow will accelerate through the channel. So, picking a single free stream velocity from the inviscid solution is not possible. As an alternative, an inviscid solution could be generated where the pressure difference was set to zero, and the mass flow rate was the same as in the viscous solution. The viscous velocity profile cannot be uniform, since the velocity has to go to zero on the boundaries. Therefore it goes from zero at the wall to some maximum, and then back to zero at the other wall, with the area under the curve representing the mass flow rate. However, the inviscid solution will be a uniform velocity across the channel with the velocity times the height of the channel equal to the viscous mass flow rate. Because of the difference in the shape of the velocity profiles, the inviscid flow velocity will be less than the maximum viscous velocity. If the definition of the boundary layer is the region where the flow is influenced by viscous forces, then the fully developed channel flow only has one point outside of the boundary layer, the center of the channel and location of maximum velocity. With this definition, the maximum velocity in the viscous solution would be the "free stream" velocity. But this conflicts with the definition of free stream velocity that is the velocity at the surface in an inviscid solution on the same geometry, because that velocity is a mean velocity across the channel and less than the maximum. Having an inviscid solution on the same geometry and with the same boundary conditions did not make the problem of finding the boundary layer thickness easier to solve; they are unrelated in this case.

5.2 Possible Detection Methods

For completeness, a few ways of finding the extent of the boundary layer are presented, along with some reasons for and against their usefulness. The following are the criteria that were used for comparing boundary layer detection algorithm

1. Uses only the vector of unknowns from the CFD simulation or quantities derived from these. This includes the mass, momentum and energy at each point.
2. Works irrespective of wall geometry
3. Does not need to know the velocity on the edge of the boundary layer before hand
4. Works for wakes and separated regions
5. Works for laminar and turbulent boundary layers

5.2.1 Potential flow quantities

One technique is to use the idea that some scalar flow quantities do not change in potential flow regions. Boundary layers can be located by marking the regions where these variables are changing, or differ from the free stream values. For this technique to work, a threshold has to be calculated or set that is a physically meaningful boundary layer edge. There has to be a value of a field variable, where if below or above this threshold, the location is no longer in the boundary layer.

Entropy is one such field variable that is a constant in the potential flow region, and generated in the boundary layer. Unfortunately it may also generated in shock waves and in areas of heat addition, so these areas would have to be somehow removed from the boundary layer detector. An entropy detector also suffers from the problem of choosing a threshold value, because entropy is not guaranteed to be the same across all the streamlines before entering the boundary layer. There are situations in isentropic flows, where the entropy does not change along a streamline, but does change from streamline to streamline. Another difficulty is that the value of the

specific entropy does not have any real physical meaning, only changes in entropy, so that a standard threshold value cannot be established.

Another possibility is to use vorticity, defined in equation 5.3, as a boundary layer marker.

$$\omega = \bigtriangledown \times \vec{q} \tag{5.3}$$

Because entropy and vorticity are intimately related, they share some of the same difficulties in finding a marker value. They are both generated in regions of curved shocks, and do not necessarily have to be zero valued outside of the boundary layer. There are cases where vorticity is being generated upstream and being convected into the boundary layer that need to be addressed. Vorticity also usually varies as $\frac{1}{y}$ from the surface, so it blends smoothly from some maximum at the wall into the freestream value of zero. This means there is no natural threshold value to determine the extent of the boundary layer region.

One technique that might be employed for finding a vorticity threshold is to move the threshold around some range while counting the number of cells or nodes that lie within the marked region. If there is some wide range of the threshold value that has the same number of marked nodes or cells, this might be an indication of an appropriate threshold value. This kind of experiment was done on the vorticity values generated from a Blasius flat plate solution. Figure 5-3 shows the result of the experiment on a 4000 node mesh. The number of points defined in as in the boundary layer varies asymptotically with the threshold value, making the choice of a cutoff value arbitrary. This technique for finding a threshold would not work.

Stagnation enthalpy overcomes some of these problems as a field marker variable, because it does not change values on either side of a stationary shock. If the free stream flow is not disturbed by an upstream boundary layer, a moving shock wave or heat addition, the stagnation enthalpy should be constant across all the streamlines in the free stream before entering the boundary layer. Using the stagnation enthalpy as a marker assumes that the Prandtl number is approximately unity; that the thermal and velocity boundary layers are of the same dimension. This type of detector also

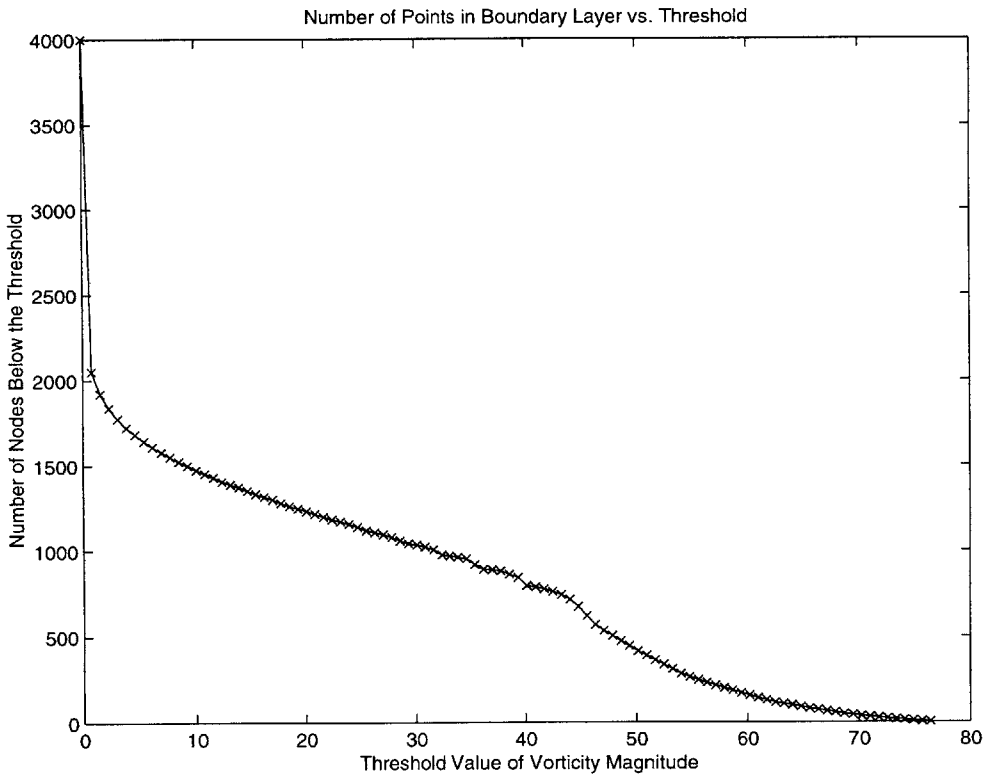

Figure 5-3: Number of Nodes with Vorticity Magnitude Less than the Threshold vs. Threshold Value

suffers from the same thresholding problems as the entropy and vorticity markers.

Using the fact that certain flow quantities do not vary in the inviscid portions of the flow field is one possible way of marking the boundary layer, but this type of marker suffers from two effects. There are other regions of viscous action beside the boundary layer that may generate these quantities. It is also difficult to create a function that relates the value of these test quantities to some boundary layer measure like $\frac{u}{U}$.

5.2.2 Comparison with boundary layer theory

One approach is to use the semi-emperical theories developed for describing laminar and turbulent velocity profiles in the boundary layer and comparing those with the velocity profile that actually exists in the CFD solution. If it was possible to derive the shape of the velocity profile from known information, then it could be fitted to the results from the CFD analysis. With the fitted curve, quantities like the displacement thickness and momentum thickness could be found analytically. Probems with this approach are formidable. Firstly, the turbulence model used to create the CFD solution may have been using different assumptions about the velocity profile than the boundary layer detector, so it would be comparing apples and oranges. Secondly, the descriptions of regions of the boundary layer like the law of the wall, law of the wake, and formulas for the log layer are all semi-empirical and depend on variables like wall curvature and pressure gradients, see for example [5]. All of the boundary layer descriptions depend on the local Reynolds number of the flow, so the local viscosity is needed for the computation. Unfortunately, the viscosity is not usually present in CFD output vector and may be a complex function of temperature. Assuming a velocity profile lacks generality needed to deal with separation regions, and three-dimensional boundary layers where there would be two profiles to find, which both depend on each other. For all of these reasons, using the boundary layer theory to compare with CFD data was not used in favor of a more direct approach.

5.2.3 Turbulence model quantities

Many of the turbulence models produce quantities like the turbulent viscosity, μ_t, to estimate the mean effects of turbulence on the flow [6]. This information may be useful, because it would indicate the region where the turbulence model predicts a boundary layer. Unfortunately, this information is not present in they typical CFD output.

5.2.4 Integration schemes

Finding a threshold for a boundary layer test quantity is also a problem since the exact extent of the boundary layer is subjective, varying from the location where $\frac{u}{U} = 0.95$ to $\frac{u}{U} = 0.99$, where u is the local speed and U is the speed of the flow just outside of the boundary layer. For that reason it may be useful to determine the unambiguous displacement and/or momentum thicknesses of the boundary layer. These quantities are also often of direct interest to analysists since displacement thickness is related to the blockage effect of the body, and momentum thickness is related to the drag on the body. Equations 1.1 and 1.2 recall the definitions for the displacement and momentum thickness. The unknowns in the equation are boundary layer thickness (δ), speed outside the boundary layer (U), and the displacement thickness (δ_1); two too many unknowns to solve for δ_1. However, near the wall the vorticity as defined by equation 5.4 and 5.5 in the two dimensional case can be related to the variation of the velocity normal to the wall. So there is an alternative approach which involves replacing U with the integral of the vorticity as in equation 5.6.

$$\omega = \nabla \times \vec{q} \tag{5.4}$$

$$\omega_z = \frac{1}{2}(\frac{dv}{dx} - \frac{du}{dy}) \tag{5.5}$$

$$U = \int_0^\delta \frac{du}{dy} dy \approx \int_0^\delta \omega_z dy \tag{5.6}$$

Since the vorticity goes to zero in the free stream irrotational flow region, the upper boundary of the integral can be changed from δ to infinity. Integrating the vorticity from the surface to infinity can then approximate the velocity outside the boundary layer. With this approximation for U, the displacement thickness can be calculated with another similar integration 5.7.

$$\delta_1 \approx \int_0^{\omega=0} (1 - \frac{u}{U_{aprox}}) dy \tag{5.7}$$

This algorithm seems to be the most attractive of the choices because it approximates the unambiguous boundary layer measures and it does not suffer from most of the problems with the previously described techniques.

5.2.5 Integration End Points

Integration schemes have another advantage because the calculated value of displacement thickness is not sensitive to a change in the end point of integration. To verify this, a test was performed where the displacement thickness was calculated on a Blasius profile while varying the end points of the integration. This value was compared to the thickness computed without integration to show the difference in threshold sensitivity of the two methods.

For the Blasius profile, $\frac{u}{U}$ is related to a function $f(\eta)$, where η is a function of y for a fixed x. $f'(\eta)$ is related to $\frac{du}{dy}$ and $f''(\eta)$ is related to $\frac{d^2u}{dy^2}$. For the vorticity integration method, $\frac{du}{dy}$ is going to be the approximated quantity, and the threshold may be related to the rate of change of vorticity with distance from the wall, or approximately $\frac{d^2u}{dy^2}$. The boundary layer will be said to extend until $\frac{d^2u}{dy^2}$, or equivalently $f''(\eta)$ is some small threshold number. $f'(\eta)$ was integrated from 0 to varying f'' threshold values, and the value of η corresponding to the calculated $f(\eta)$ was compared to η at the threshold f''. Results show η changes rapidly with changes in the $f''(\eta)$ threshold value, but η calculated with the integral is much less sensitive to changes in the end point of integration. This result is shown in figure 5-4 and is not surprising given that the velocity profile approaches the free stream asymptotically. There should be little

difference in the displacement thickness calculation as long as the end points of the integration are within the area where the velocity profile becomes arbitrarily close to the free stream value.

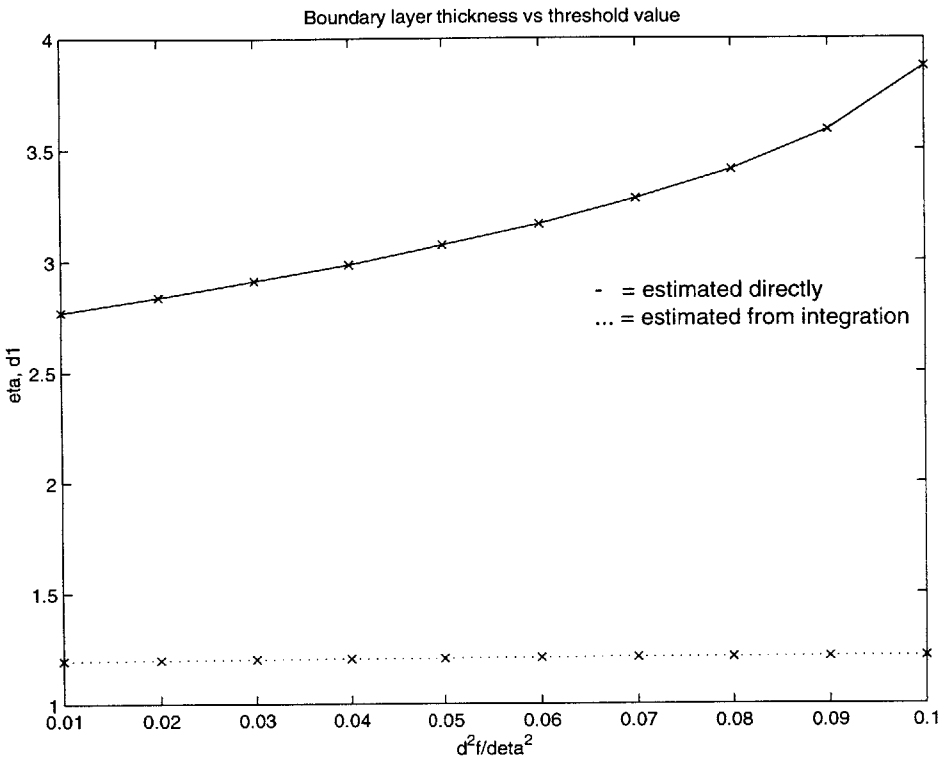

Figure 5-4: Variation in boundary layer thickness with changes in integration end point

Another possibility that has to be considered is how the end points of integration can be set to capture a boundary layer thickness in separated flows. Figure 5-5 shows some of the possible velocity profiles encountered in two-dimensional models. For the attached case, both the derivative of velocity and the second derivative of velocity go to zero toward the free stream. However, at the point of separation, there is an inflection point in the velocity profile, so setting the endpoint by locating the zero point of the first or second derivative will neglect the entire boundary layer. It is a similar situation for the fully separated case, except that the first and second derivatives will not be zero except as they approach the free stream. As a heuristic approach to finding the end point of integration, one could choose the location where the first and second derivatives are some arbitrarily small number, but some small

distance away from the wall to capture the information at the point of separation.

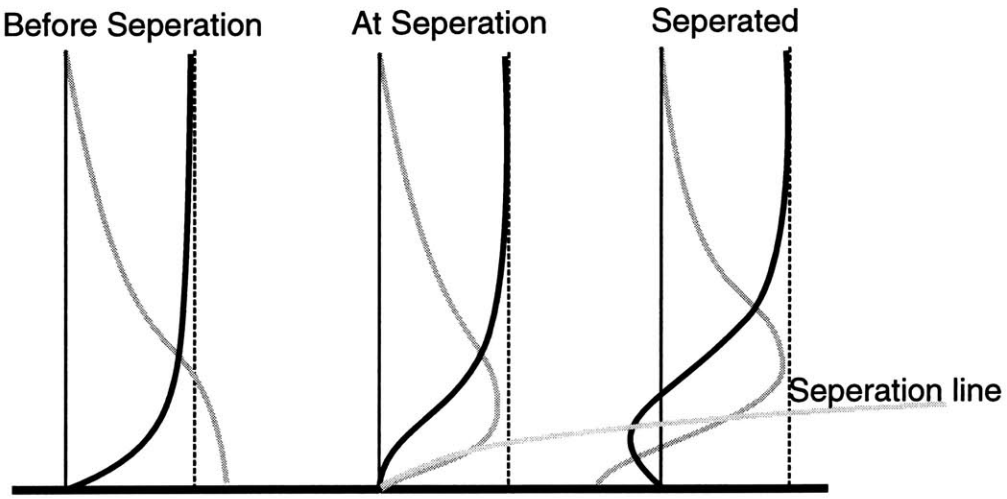

Figure 5-5: Velocity and velocity derivative profiles for various regimes

5.2.6 Geometric Difficulties

Geometric considerations create other difficulties in defining a boundary layer thickness and in determining the direction of integration. Ideally, the edge of the boundary layer can be visualized as a surface in a three-dimensional flow, and as a curve in two dimensions. The question is how to represent that surface or curve as a distance function along normals from a wall boundary. It may happen in some instances that this boundary layer surface does not intersect some of the wall surface normals. The easiest geometry to visualize this problem is with a corner flow model as shown in figure 5-7. As the origin is approached along y axis, normals to the yz plane pointing in the x direction reach a point where they do not cross the boundary layer surface, so the thickness of the boundary layer at that point along that normal is undefined. Figure 5-6 shows the displacement surface of the corner flow model and the same surface viewed as a function of displacement along the surface curve of the corner. Having a distance function defined on the wall that has singular points is not acceptable computationally. One option is to create "normal" curves that are better behaved, and ideally non-intersecting. That is, curves which start out normal to the surface, but may deviate from this away from the wall. A corner flow model was investigated to

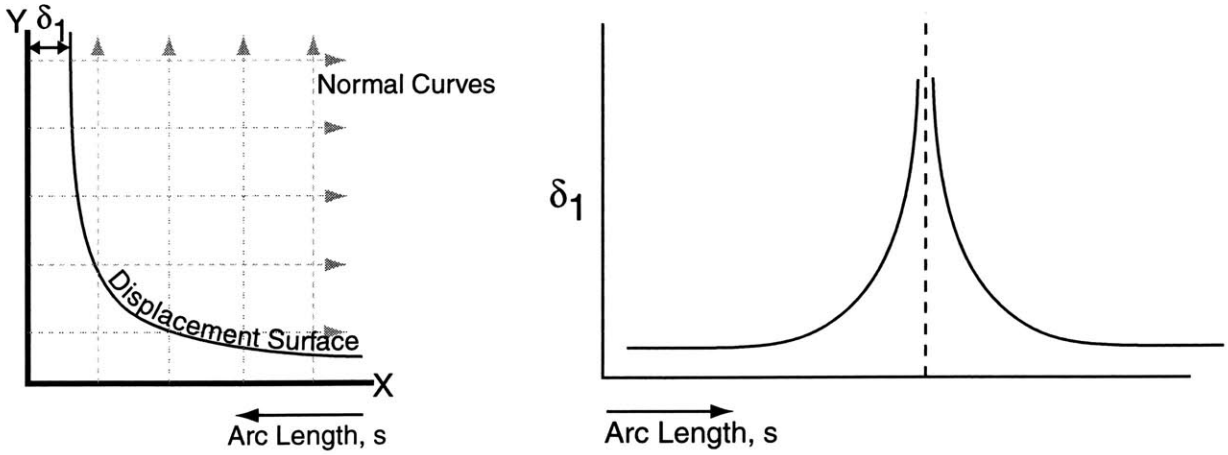

Figure 5-6: Boundary layer surface represented as a function of arc length

see if it is possible to choose different normal curves in the integration, but yield the same boundary layer curve. The solution to viscous flow in a corner as shown in 5-7 is described in Schlichting [4]. Because only the characteristic shape of the solution was important in this application, the solution was approximated with equation 5.8, where a is an arbitrary constant.

$$\phi = \frac{u}{U} = axy \tag{5.8}$$

Taking a two-dimensional cross section of the flow in the xy plane, and determining the displacement thickness along the $x = 0$ curve yields equation 5.9 for the curve of the displacement thickness boundary.

$$y = \frac{1}{2ax} \tag{5.9}$$

The problem with using equation 5.9 to describe the displacement thickness along the $y = 0$ wall is that there is a singularity as x approaches zero. To remove the singularity, curves may be defined that are everywhere normal to the curves of constant ϕ, these being the curves satisfying equation 5.10.

$$\psi = \frac{a}{2}(x^2 - y^2) \tag{5.10}$$

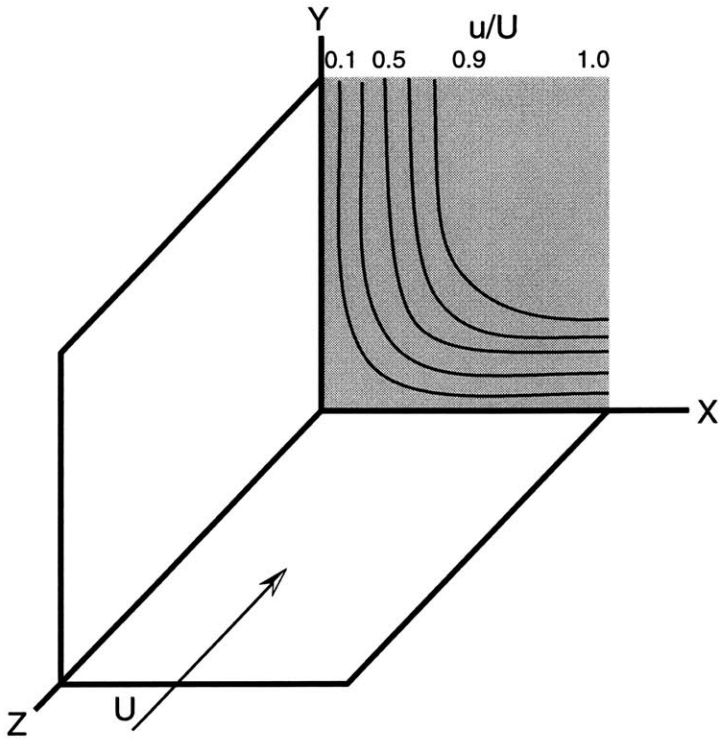

Figure 5-7: Corner Flow Model

The function ϕ represents a potential flow solution; the solution to the LaPlace equation. Using the stream function, ψ or alternatively the gradient of ϕ to determine the curves of integration is attractive because every such curve is unique and does not intersect any of the other $\psi = const$ curves. It also has the property that there are no singular points of the displacement thickness. The distances along the normal curves from the surface to the boundary layer curve all have real values.

Figure 5-8 shows the constant ϕ curves calculated for the corner flow model. Figure 5-9 is a plot of the ψ contour values, which are everywhere tangent to the gradient of ϕ. Figure 5-10 is a superposition of the ψ and ϕ coordinate system.

The boundary layer thickness, δ_1 on the normal curves, was determined with equation 5.11. This equation expresses the mass balance through the boundary layer. The first integral is the area outside the displacement thickness curve, but inside the boundary layer curve as shown in figure 5-11. This area times the free stream velocity is equal to the mass flow through the boundary layer, which is equal to the area expressed in the second integral times the free stream value.

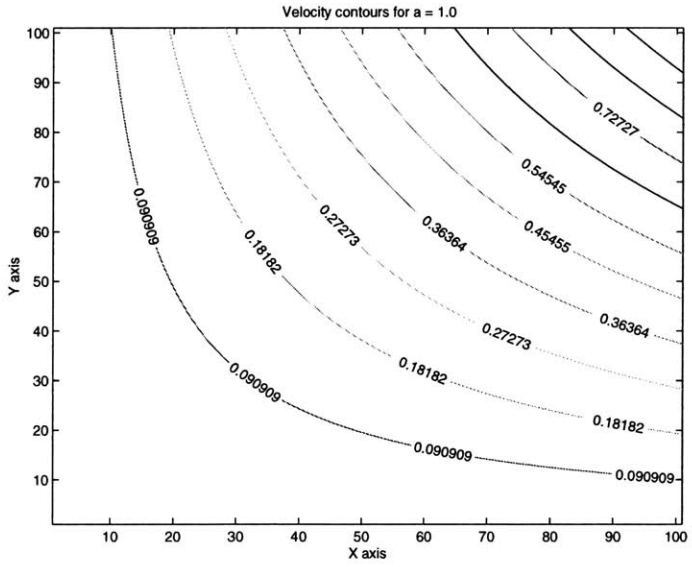

Figure 5-8: ϕ Function and values of $\frac{u}{U}$

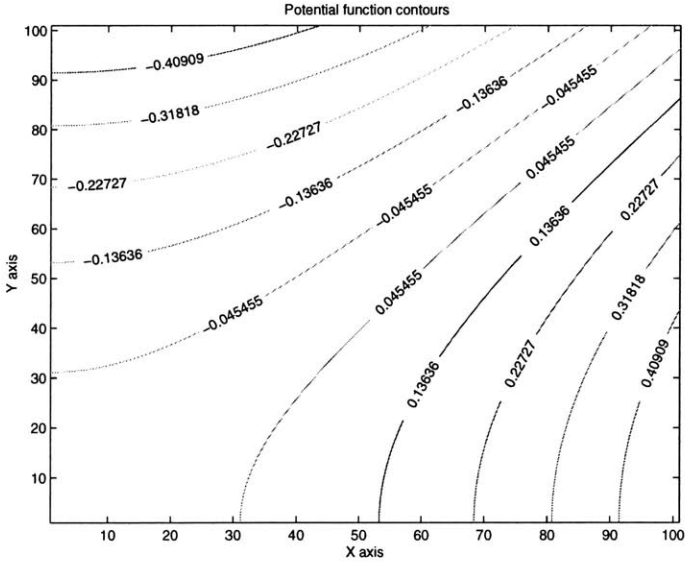

Figure 5-9: ψ Function contours

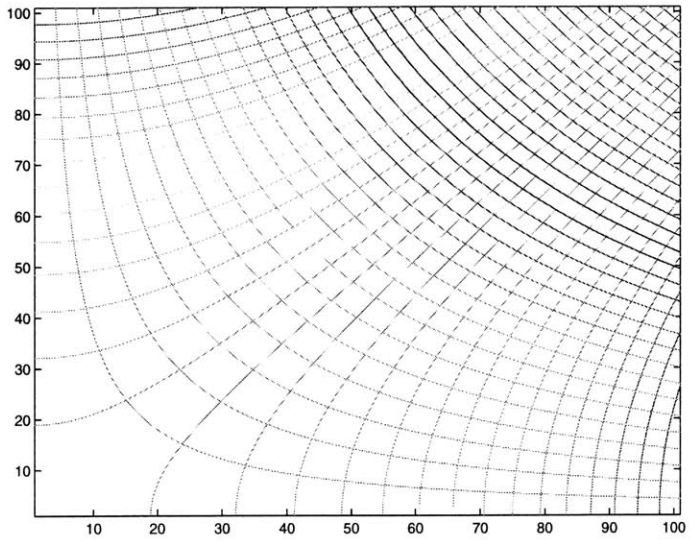

Figure 5-10: ψ and ϕ contours

$$\int_{\delta_1}^{\delta} d\phi d\psi = \int_0^{\delta} \frac{u}{U} d\phi d\psi \tag{5.11}$$

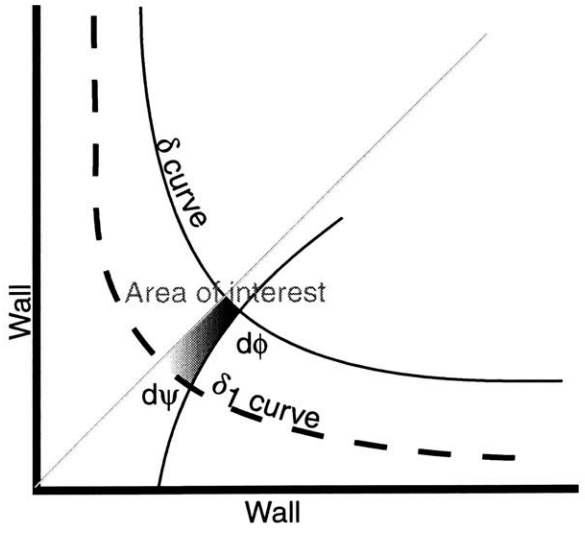

Figure 5-11: Areas used in displacement thickness calculation

To numerically estimate the displacement thickness from the equation, the domain was first descretized into square elements. The areas for all the elements within a small interval, $\Delta\psi$ were calculated and then the value of ϕ was varied to find the correct value of ϕ for which equation 5.12 was satisfied, where ϕ_{δ_1} is the value of *phi*

at the δ_1 curve and ϕ_δ is the value of ϕ at the edge of the boundary layer.

$$\sum_{0}^{\phi=\phi_{\delta_1}} \Delta phi, \Delta\psi = \sum_{0}^{\phi=\phi_\delta} \phi * \Delta\phi * \Delta\psi \tag{5.12}$$

The calculated displacement curve is shown in figure 5-12. The calculated curve deviates from the actual displacement thickness the greatest in the region 45 degrees from the center of the corner. This occurred because the shape of the $\psi = const$ curves becomes distorted in this region; they become closer together, enclosing fewer cells in the discretization and causing numerical errors. By defining the appropriate

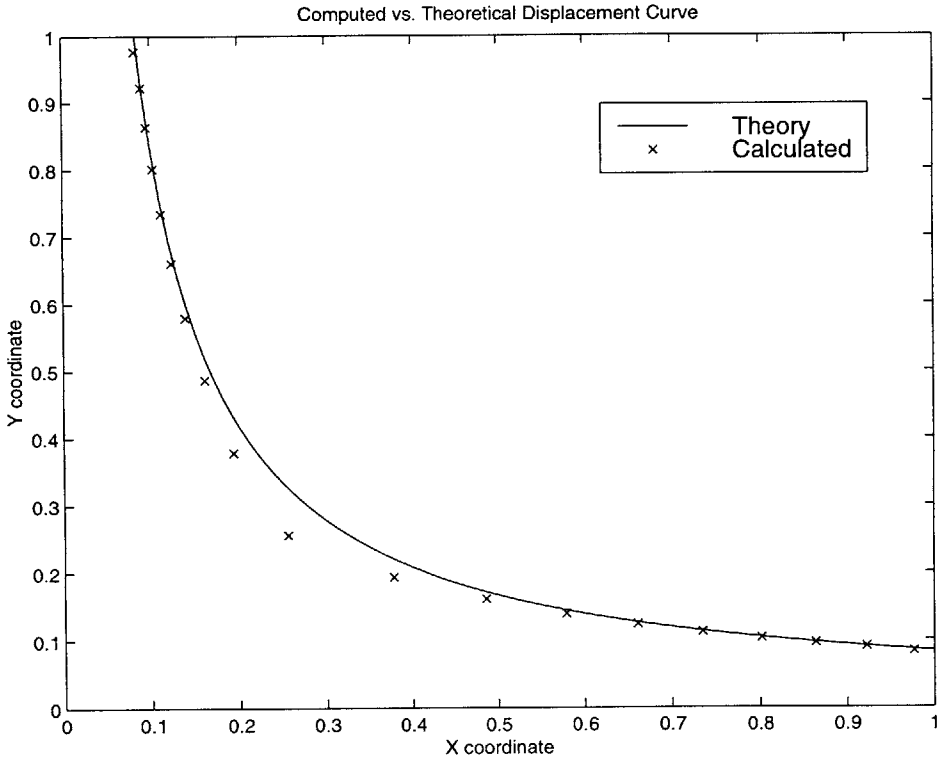

Figure 5-12: Corner flow calculated vs. theoretical displacement curve

normal curves, the displacement function became finite along the wall curve, but still closely approximates the actual location of the boundary layer curve.

Chapter 6

2D Boundary layer detection

The vorticity integration method that has been developed was applied to some of the principal solutions of the boundary layer equations to verify that the method would be applicable to these simple cases.

6.1 Flat plate results

Using it on the Blasius solution of laminar flow over a flat plate in a zero pressure gradient validated the boundary layer detection method.

6.1.1 Velocity integration vs. vorticity integration

The first thing to determine was whether the vorticity integration could really be used to approximate the free stream velocity and the location of the edge of the boundary layer. The method must produce accurate results for this simplest of cases, or else has no hope of being accurate in a real boundary layer determination, where numerical effects have influence.

For the Blasius solution over a two-dimensional flat plate, the two velocity components u_1 and u_2 are related to a function of a non-dimensional parameter η with

the following equation 6.3 from Schlicting [4].

$$\eta = y\sqrt{\frac{U}{x\nu}} \tag{6.1}$$

$$u_1 = Uf'(\eta) \tag{6.2}$$

$$u_2 = \frac{1}{2}\sqrt{\frac{U\nu}{x}}(\eta f' - f) \tag{6.3}$$

These relationships can be used to find the expression for the vorticity through the boundary layer, equation 6.4. Outside the boundary layer, the second derivative of the f function goes to zero, which makes the vorticity go to zero outside the boundary later. This is encouraging since the exact end point of the line integral is not critical, just as long as the vorticity is vanishingly small.

$$\omega = -f''(\eta)(\eta\frac{Uy}{4x^2} + \frac{U^{3/2}}{\sqrt{\nu x}}) \tag{6.4}$$

This equation for the vorticity was numerically integrated for a fixed value of x to determine how closely it would approximate the free stream value. The calculated value for the free stream velocity, U, was within 1% of the actual value.

Since the theoretical accuracy seems reasonable, the Blasius solution was mapped onto a small rectangular grid and the full algorithm was applied to the model to determine experimental values of the displacement and momentum thickness as functions of distance from the leading edge. The steps in implementing the method were as follows:

1. Triangulate the area over the flat plate.

2. Find the velocity at each point from the Blasius solution.

3. Set the points on the plate to have a value of 1.0 for ϕ, and those points on the upper portion of the domain to have a value of ϕ equal to 0.0.

4. Solve the LaPlace equation on the domain to find the ϕ field. A finite element technique was used to solve the equation on the domain, with the previously described dirchlet conditions.

5. A streamline integration technique was applied to integrate the vorticity along the gradient curves starting at the nodes on the plates.

6. These integration values were used to make an approximation to the displacement and momentum thicknesses at each node on the plate.

These results were then compared to the Blasius results and show a good agreement. Figure 6-1 is a picture of the model with the vorticity imposed from the Blasius solution results.

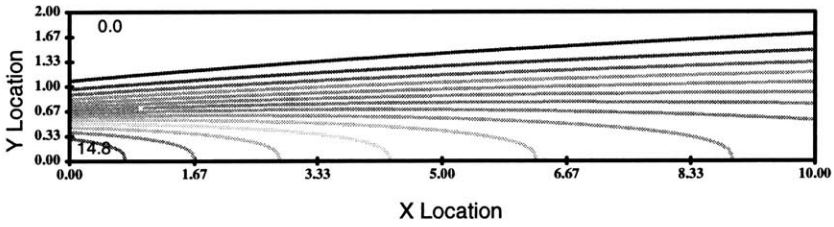

Figure 6-1: Vorticity plot on the flat plate test case

Figure 6-2 and 6-3 are plots of the displacement thickness and momentum thickness, respectively.

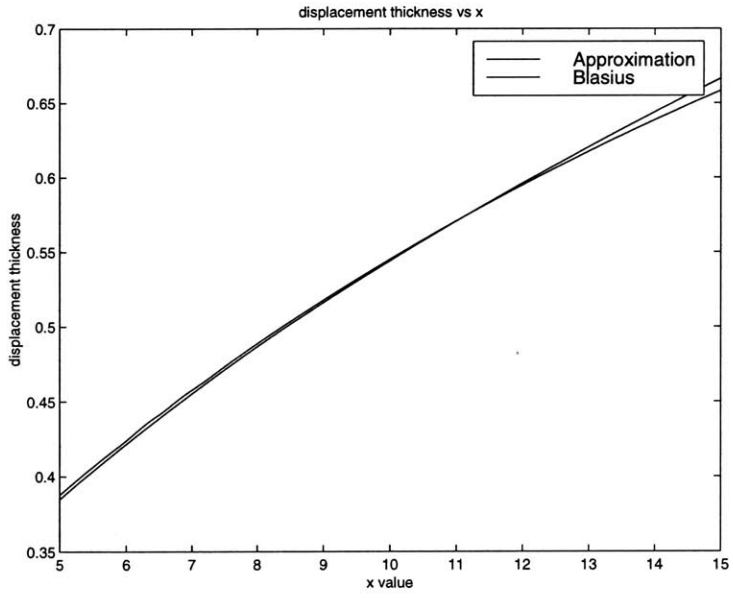

Figure 6-2: Displacement Thickness Calculated vs. Theoretical

The errors between the calculated and theoretical values of δ_1 and the momentum thickness are shown in figures 6-4 and 6-5, respectively.

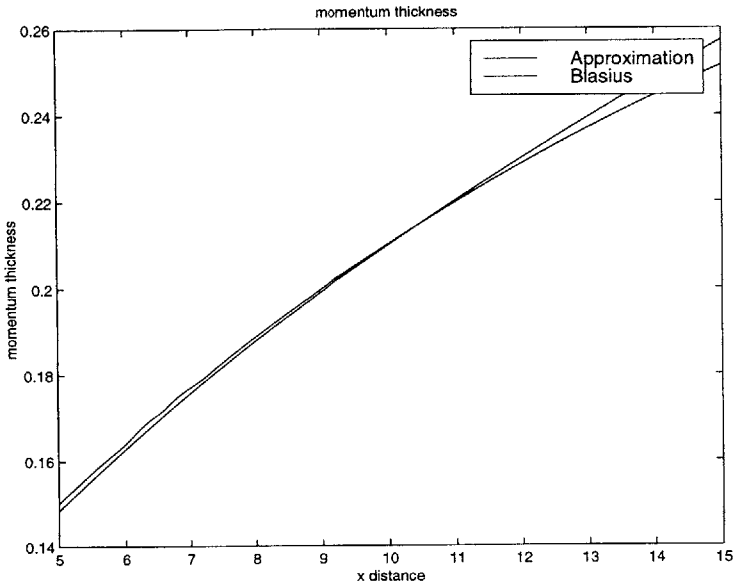

Figure 6-3: Momentum Thickness Calculated vs. Theoretical

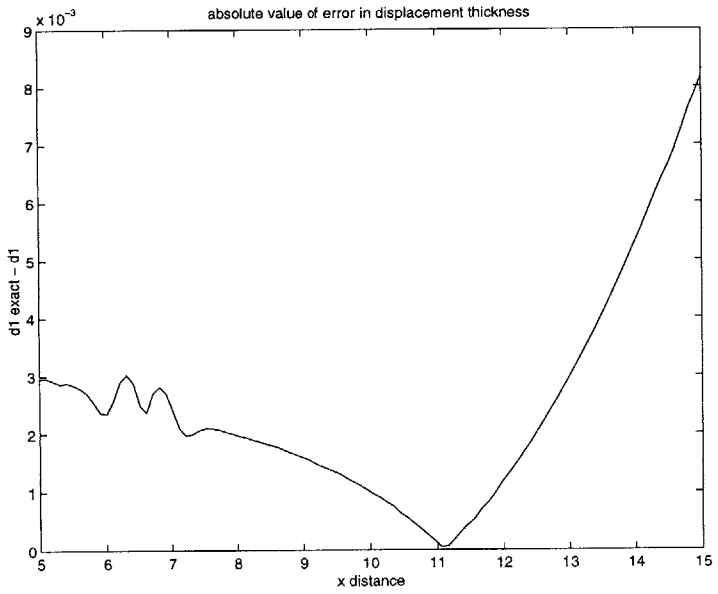

Figure 6-4: Calculated vs. theoretical displacement thickness

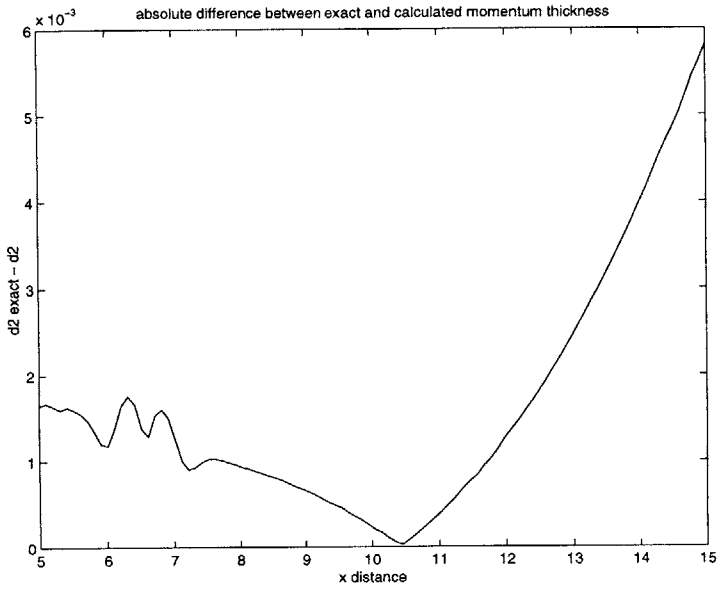

Figure 6-5: Calculated vs. theoretical momentum thickness

The error increases on the downstream side of the model because the vorticity does not go to zero at the furthest location normal to the surface. For the method to work properly, the boundary layer must be contained in the model domain, with the vorticity going to zero at the boundaries of integration.

6.2 Pipe Flow

The boundary layer estimation technique was applied to a model of fully developed laminar pipe flow. The pipe model was investigated primarily to determine the accuracy of the numerical techniques that were applied to the problem. Even though the model was two dimensional, the problem is actually one dimensional, with velocity being a function of the radial coordinate alone, so boundary layer thicknesses should not be a function of z or θ. However, it was analyzed as a higher dimensional model to make sure the numerical integration techniques were extensible to a three dimensional case. Figure 6-6 shows the model geometry and the coordinate system used in the analysis.

Since the flow is fully developed, the velocity is only a function of the radial coordinate, and from the Hagen-Poiseuille pipe flow equations described in Schlicting [4],

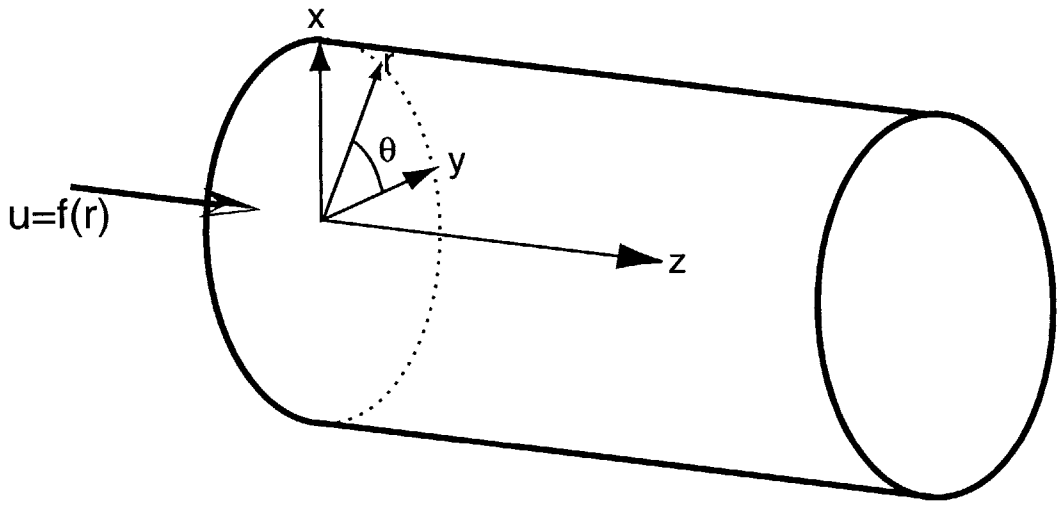

Figure 6-6: Pipe flow model geometry

the velocity in the z direction varies with r according to relationship in equation 6.5, where R is the radius of the tube.

$$u_z(r) = \frac{p_1 - p_2}{4\mu l}(R^2 - r^2) \tag{6.5}$$

The vorticity in the cylindrical coordinate system is expressed in equation 6.6, where $\hat{e_r}$, $\hat{e_\theta}$ and $\hat{e_z}$ are the unit vectors in the cylindrical coordinate system. The equation is simplified in this situation to equation 6.7 since the velocity only varies in the radial direction.

$$\omega = \bigtriangledown \times U = (\frac{1}{r}\frac{du_z}{d\theta} - \frac{du_\theta}{dz})\hat{e_r} + (\frac{du_r}{dz} - \frac{du_\theta}{dr})\hat{e_\theta} + \frac{1}{r}(\frac{d(r\ u_\theta}{dr} - \frac{du_r}{d\theta})\hat{e_z}\frac{1}{r} \tag{6.6}$$

$$\omega_\theta = -\frac{du_z}{dr} = -\frac{p_1 - p_2}{2\mu l}r \tag{6.7}$$

In order to determine how closely the displacement thickness can be approximated by integrating the vorticity, it is only necessary to find out how closely the integral of the vorticity approximates the maximum velocity through the pipe, since this is

the only location outside the boundary layer. Equation 6.8 is used to calculate the maximum velocity in the center of the pipe, and 6.9 is the approximate u_{max} value that can be calculated from integrating the θ component of the vorticity.

$$u_{max} = \frac{p_1 - p_2}{4\mu l} R^2 \tag{6.8}$$

$$u_{max} \approx \int_0^R -\omega_\theta dr = \int_0^R \frac{p_1 - p_2}{2\mu l} r \tag{6.9}$$

If the integral of the vorticity is performed, it exactly equals the expression for the maximum velocity. This directly implies that the calculation of the displacement thickness by vorticity integration will also be exact. Unlike the flat plate case, using the vorticity integration yields the exact same displacement thickness as the definition. In a similar way, the momentum thickness was calculated using both methods, and was found to be equal to $\frac{2}{15}R$.

6.2.1 Boundary layer measurements in channels

The variables δ_1 and δ_2 do not have the same meaning for pipe flow as they do for boundary layers in external flows. In external flows, δ_1 is the mass flow deficit per unit length normal to the flow due to the boundary layer. However, this no longer holds in the pipe flow example as can be shown by comparing the actual mass flow rate through a section, Q_a, to the mass flow rate calculated by knowing δ_1, Q_c.

$$Q_a = \pi R^2 u_{ave} = \frac{\pi}{8} \frac{R^4}{\mu} (-\frac{dp}{dx}) \tag{6.10}$$

$$u_{ave} = \frac{R^2}{8\mu} (-\frac{dp}{dx}) \tag{6.11}$$

$$Q_c = \pi \frac{8R^2}{9} u_{ave} = \frac{\pi}{9} \frac{R^4}{\mu} (-\frac{dp}{dx}) \tag{6.12}$$

Equation 6.13 follows from the relations for the calculated and actual mass flow rate.

$$\frac{Q_c}{Q_a} = \frac{8}{9} \tag{6.13}$$

Therefore the displacement thickness does not represent the location where the velocity contour can be approximated by a discontinuity from the free stream value to zero, while maintaining the same mass flow rate. The displacement thickness description is unable to capture the mass deficit of geometries with a finite radius of curvature. Figure 6-7 shows the region of overlap in the elemental areas that are used by the δ_1 calculation along with a corrected elemental area.

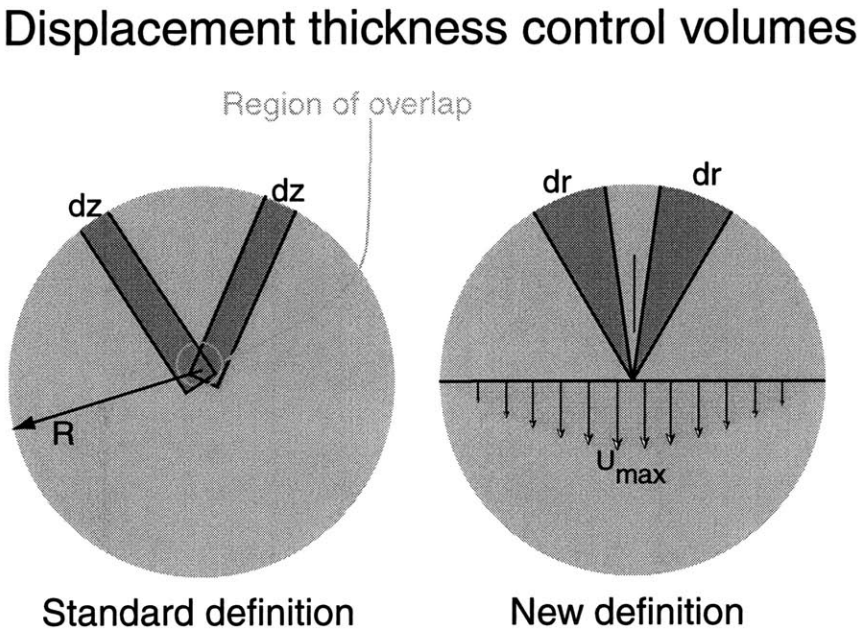

Figure 6-7: Integration Areas for the pipe

6.3 Boundary layer detection on a laminar flow airfoil model

The boundary layer detection algorithm was tested on a two dimensional viscous solution of the flow around a NACA0012 airfoil at a Reynolds number of 500. Figure 6-8 are contours of the velocity field around the airfoil model.

The vorticity was calculated by first breaking up the structured quadrilateral grid into triangular elements. Secondly, triangular element shape functions were used to calculate the velocity gradients at the center of each triangular cell. These gradients

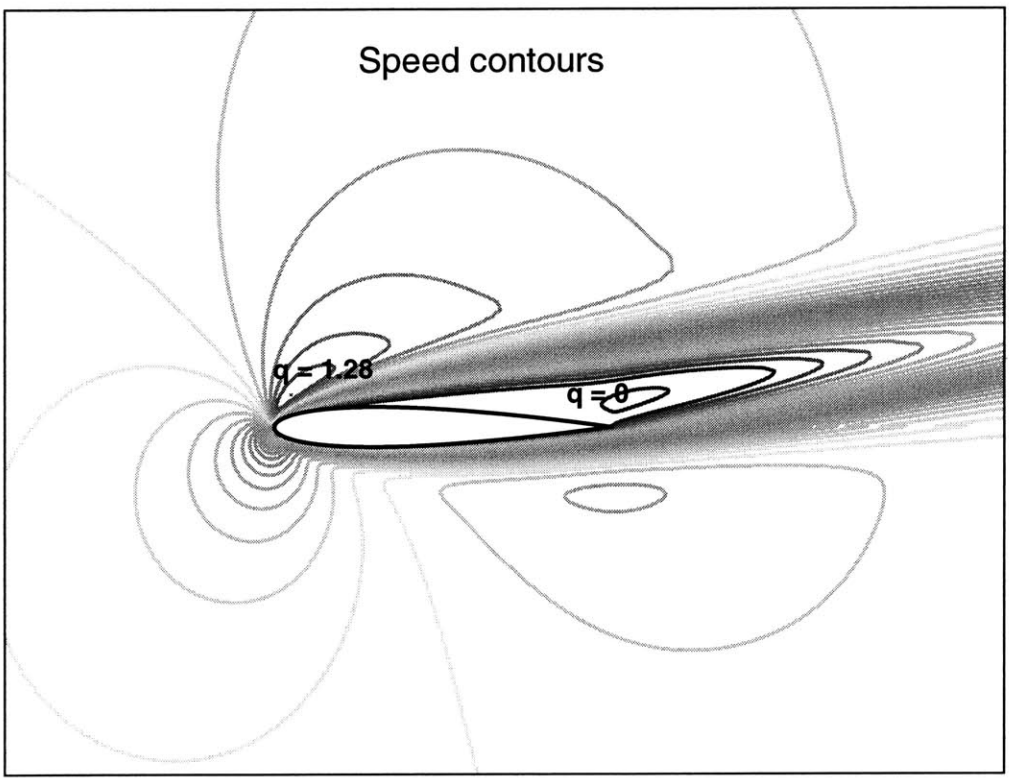

Figure 6-8: Velocity contours on NACA0012 airfoil in Re = 500 flow

were used to calculate the value of omega for each cell using the equation 6.14.

$$\omega = \frac{dv}{dx} - \frac{du}{dy} \tag{6.14}$$

The values at each cell where then distributed to the nodes using a area weighted averaging rule, equation 6.15.

$$\omega_{node} = \frac{\sum w_{cell} a_{cell}}{\sum a_{cell}} \tag{6.15}$$

The results of the vorticity calculation are shown in figure 6-9. The contours show a recirculation region near the trailing edge of the airfoil.

The displacement and momentum thickness calculations depend on the approximation of the free stream velocity. Figure 6-10 is a graph of the actual speed, the calculated speed and the vorticity along a normal curve at a point on the lower surface of the airfoil, where $\frac{x}{c} = 0.118$. Figure 6-11 is a similar calculation done on a point

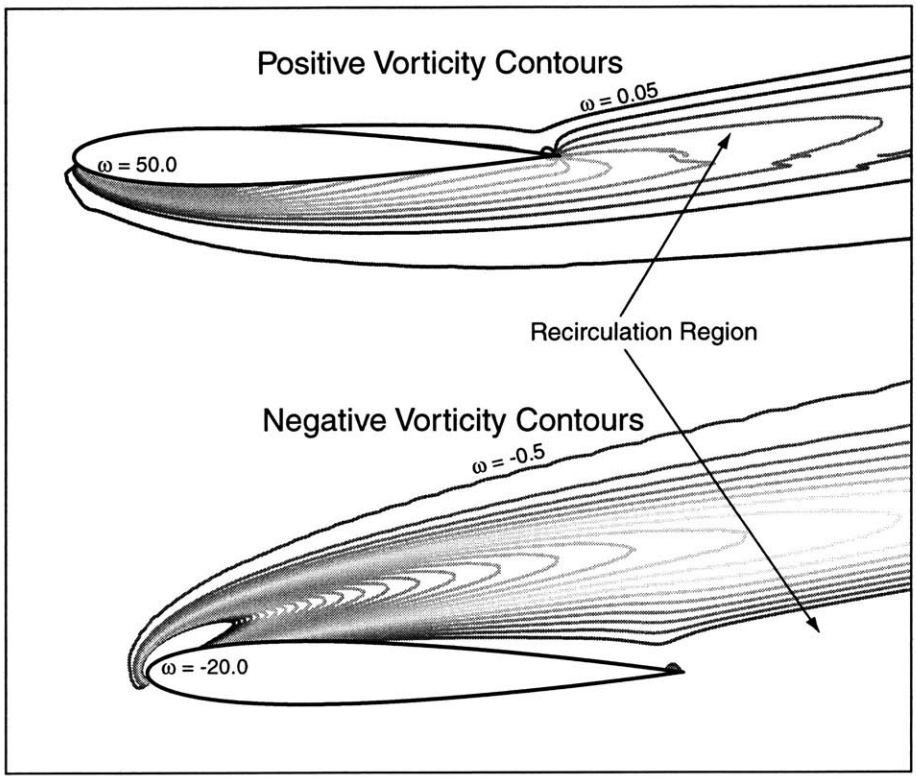

Figure 6-9: Vorticity contours on NACA0012 airfoil in Re = 500 flow

on the upper surface where $\frac{x}{c} = 0.32668$.

At both locations, the calculated speed values closely approximate the actual speed values until the vorticity becomes small in magnitude outside of the boundary layer. Outside the boundary layer, the speed may increase or decrease, but the calculated free stream value stays the same since the vorticity has gone to zero. This is encouraging since the vorticity integration method yields a free stream velocity approximation that is not very dependent on the end point of integration.

The results of examining a third point on the airfoil are shown in figure 6-12.

This point located on the upper surface of the airfoil where $\frac{u}{U} = 0.89$ and is in the recirculation region. Because it is possible to get an estimate of the free stream velocity even in the separated area where the vorticity changes sign, it is possible to find the displacement thickness in this region.

The free stream values calculated with the integrated vorticity method are shown in figure 6-13.

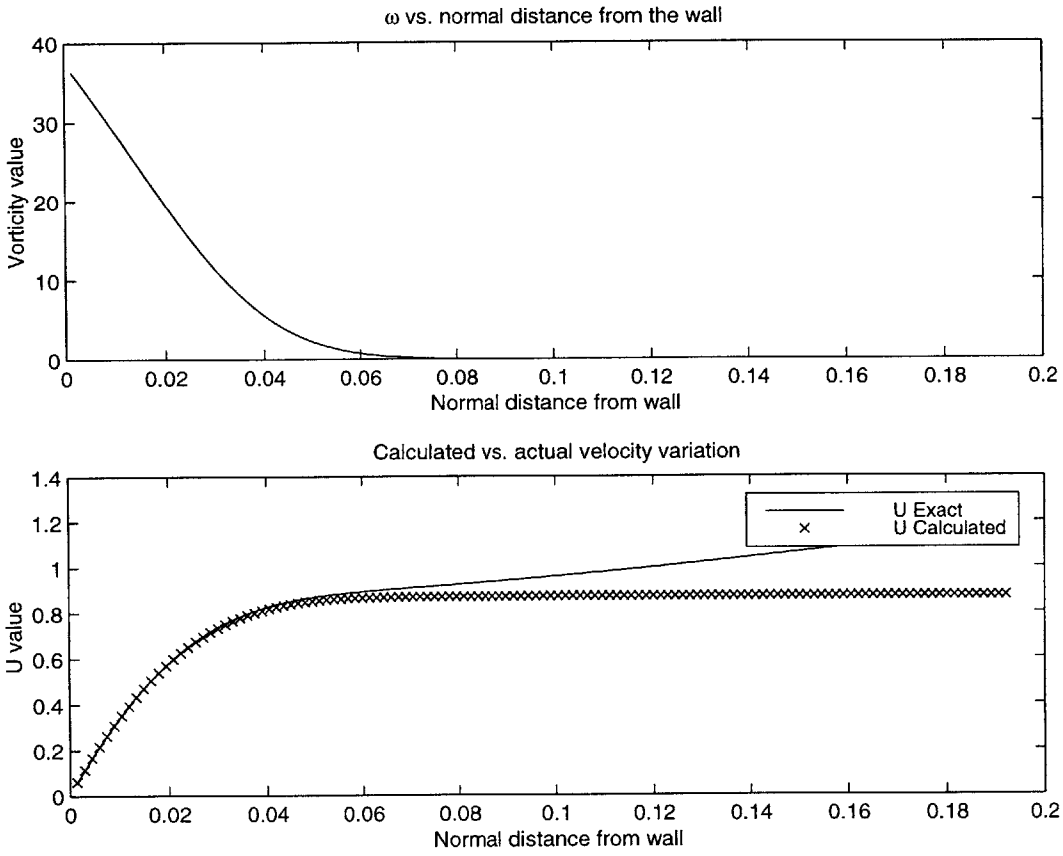

Figure 6-10: Free stream velocity calculation on airfoil in laminar flow, $\frac{x}{c} = 0.118$

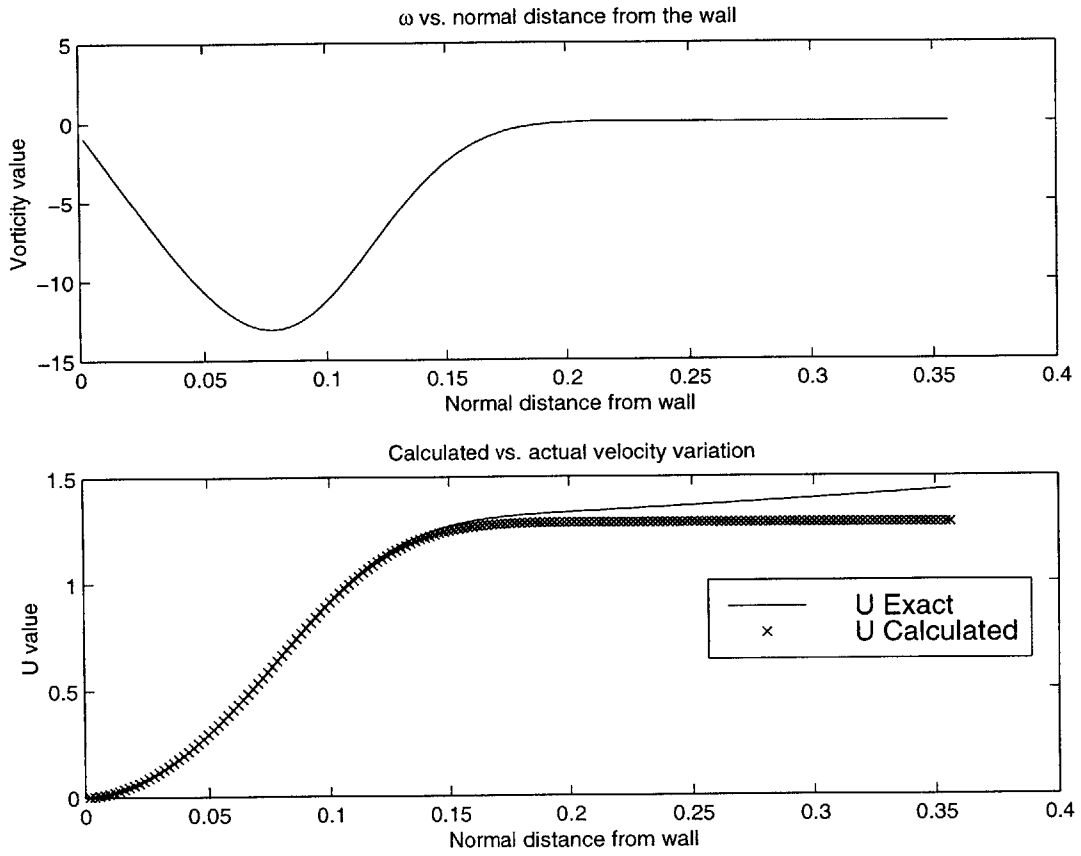

Figure 6-11: Free stream velocity calculation on airfoil in laminar flow, $\frac{x}{c} = 0.327$

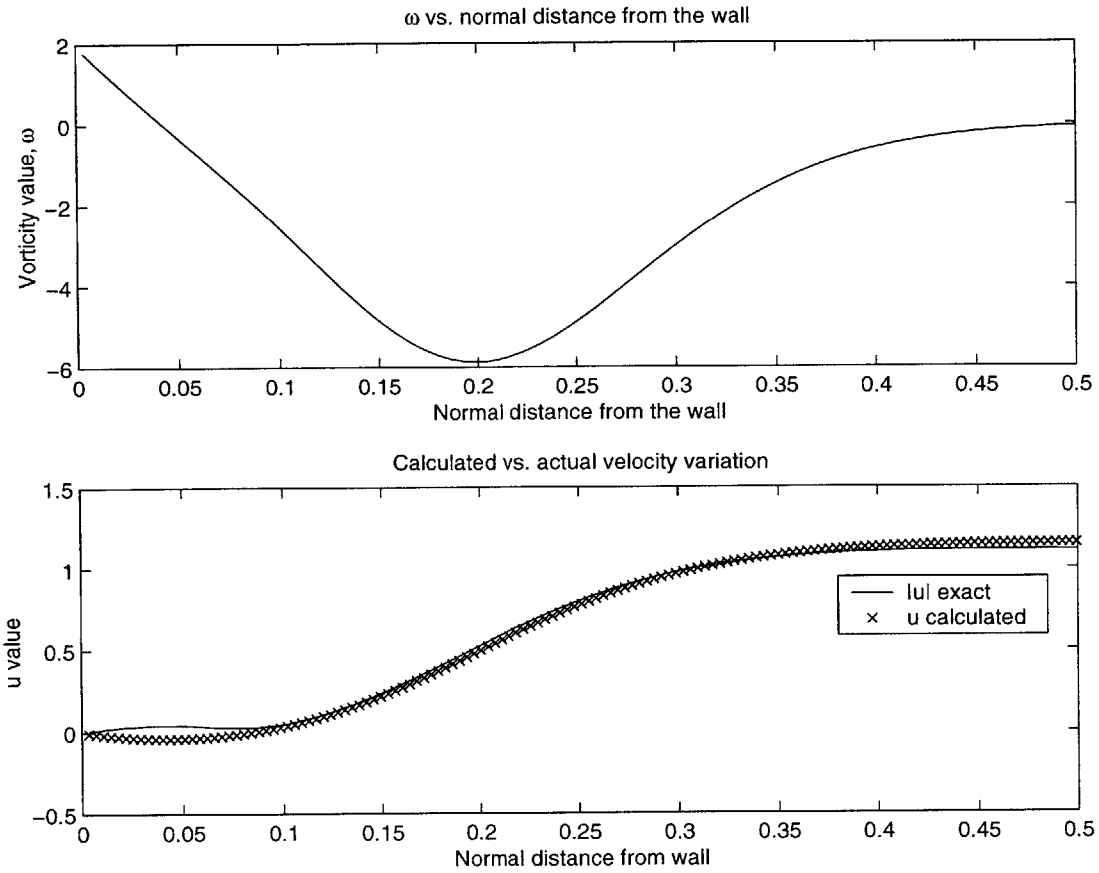

Figure 6-12: Free stream velocity calculation on airfoil in laminar flow, $\frac{x}{c} = 0.89$

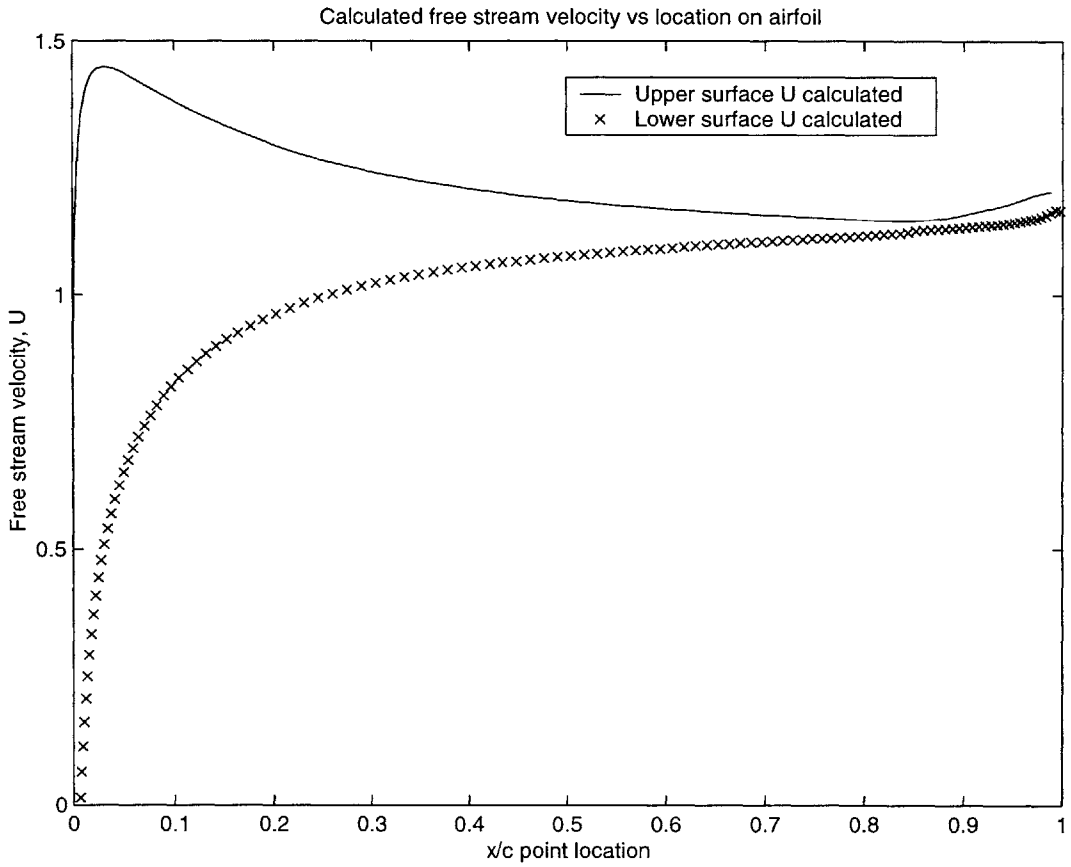

Figure 6-13: Calculated free stream velocity on laminar flow airfoil model

As was expected, the free stream velocity starts from zero at the stagnation point then increases to a maximum just beyond the leading edge in the low pressure region.

After the free stream values were calculated, the displacement thickness was estimated using another integration along the normal curves. The results are presented in figure 6-14.

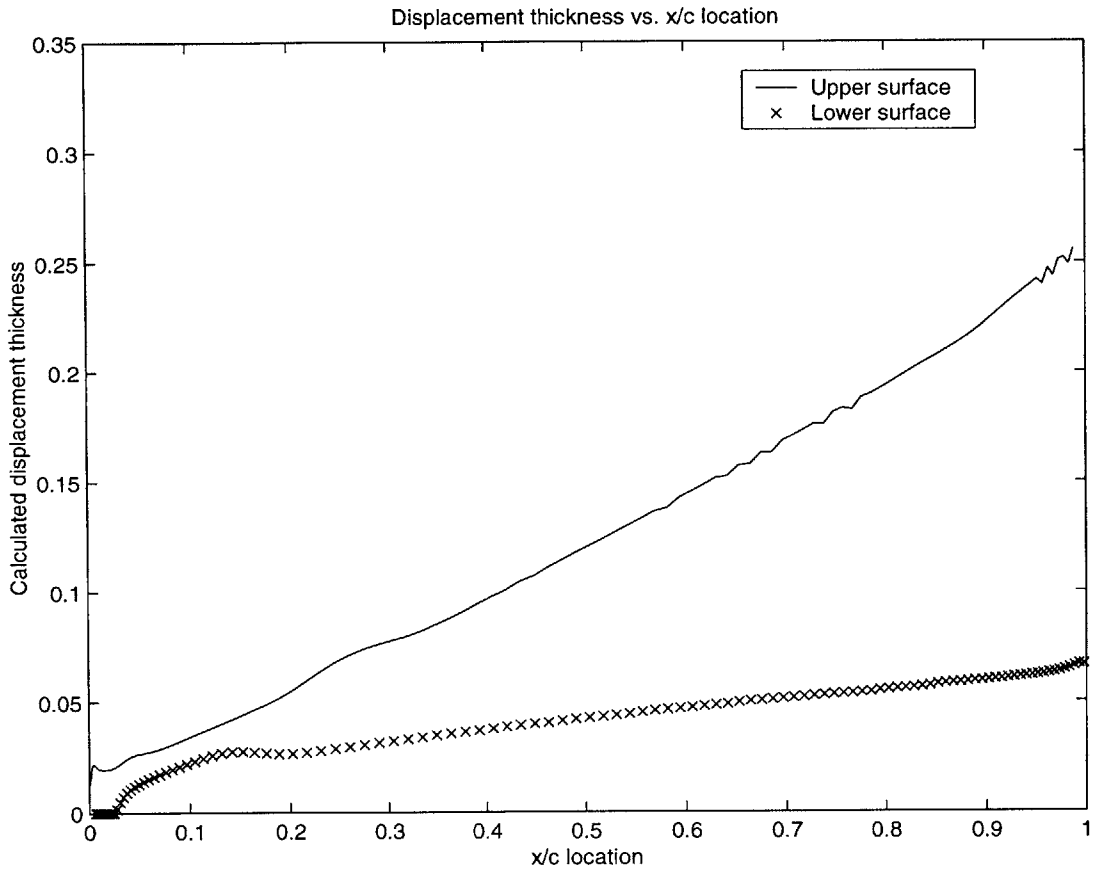

Figure 6-14: Calculated displacement thickness on laminar flow airfoil model

6.4 Boundary layer detection on a turbulent flow airfoil model

In the laminar flow case, the boundary layer thickness was not known, so it could not be compared to the boundary layer estimate extracted from the Navier-Stokes solution. So, the vorticity integration method was applied to another airfoil model

with a displacement thickness calculated with a more direct method.

The same free stream velocity calculation and vorticity estimation procedure was applied to this model as with the laminar flow model. Normal integration curves were calculated by solving LaPlace's equation on the domain, yielding the integration curves shown in figure 8-16. Figure 6-15 and figure 6-16 are plots of the calculated vs. actual speed values along the integration curves at two different locations on the airfoil surface.

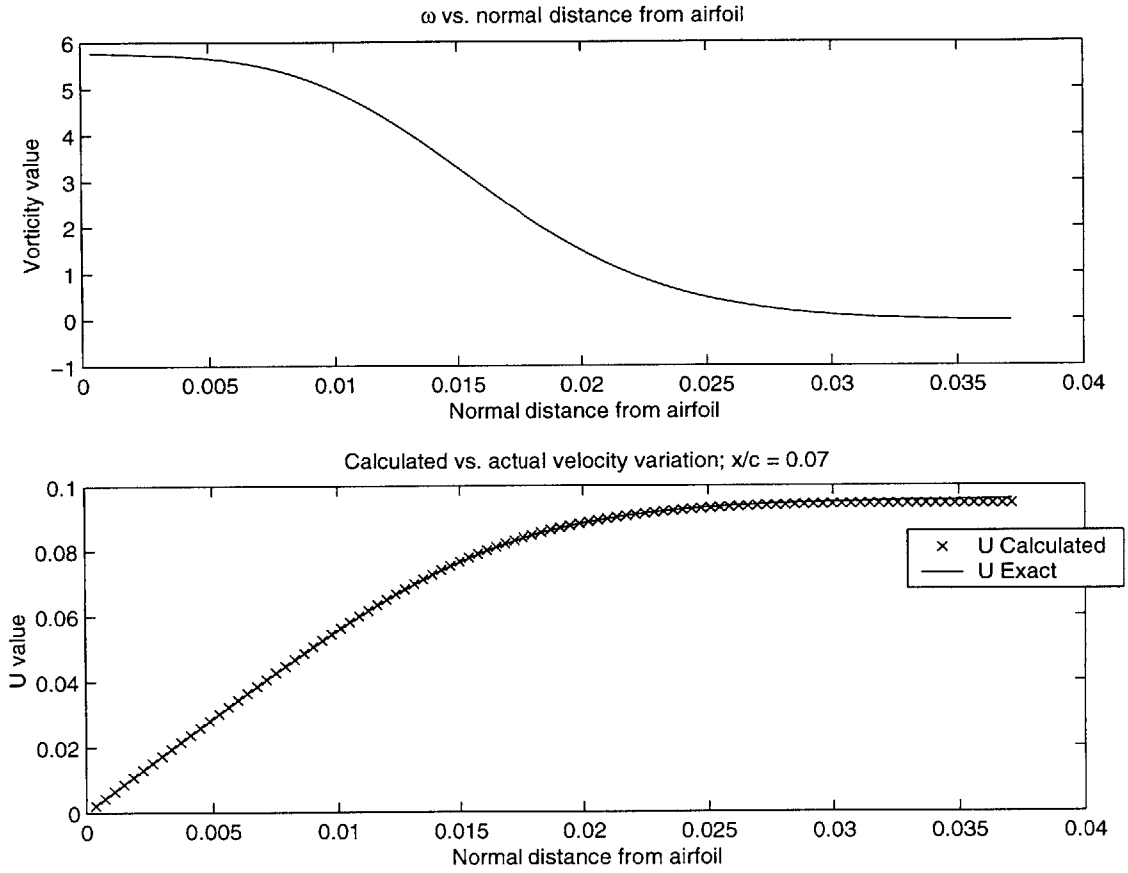

Figure 6-15: Free stream velocity estimation at $\frac{x}{c} = 0.1$

As in the laminar flow case, the estimated speed value closely follows the actual velocity magnitude value until outside the boundary layer where the vorticity is zero and the calculated speed no longer changes with distance.

The curve of estimated free stream velocity with distance along the airfoil is shown in figure 6-17. Following the laminar flow calculation of the displacement thickness, the estimated turbulent flow airfoil displacement thickness on the upper surface is

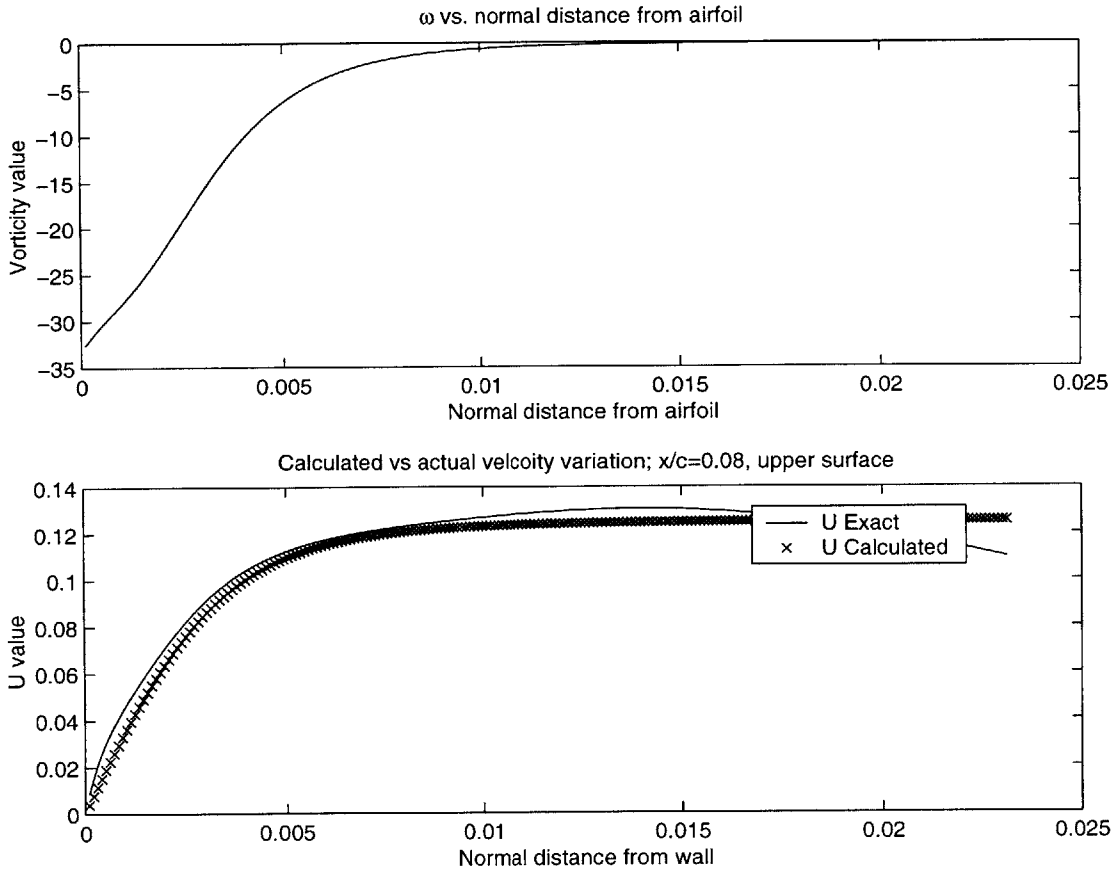

Figure 6-16: Free stream velocity estimation at $\frac{x}{c} = 0.008$

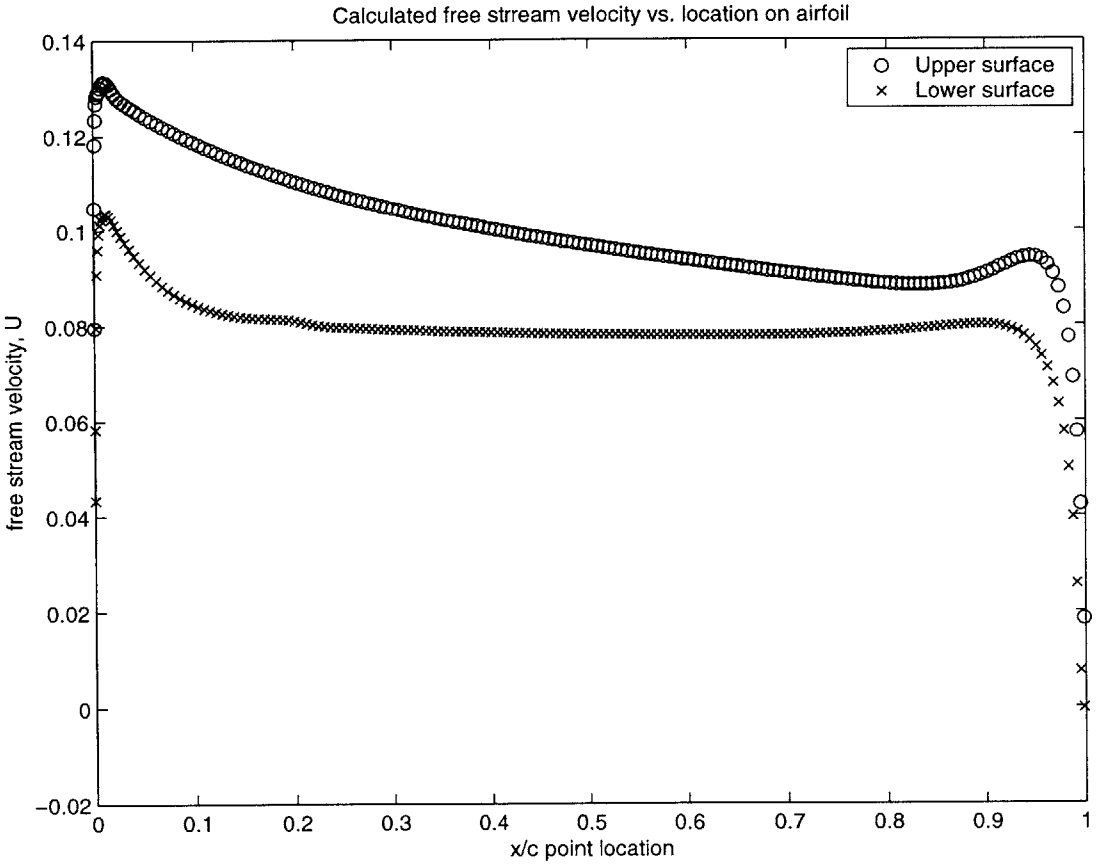

Figure 6-17: Free stream velocity vs. location

shown in figure 6-18. Because the flow field was calculated by first using a boundary integral method to find the extent of the boundary layer, this value of δ_1 could be checked against the calculated value. The upper surface results are shown in figure 6-18 and the lower surface results are displayed in figure 6-19.

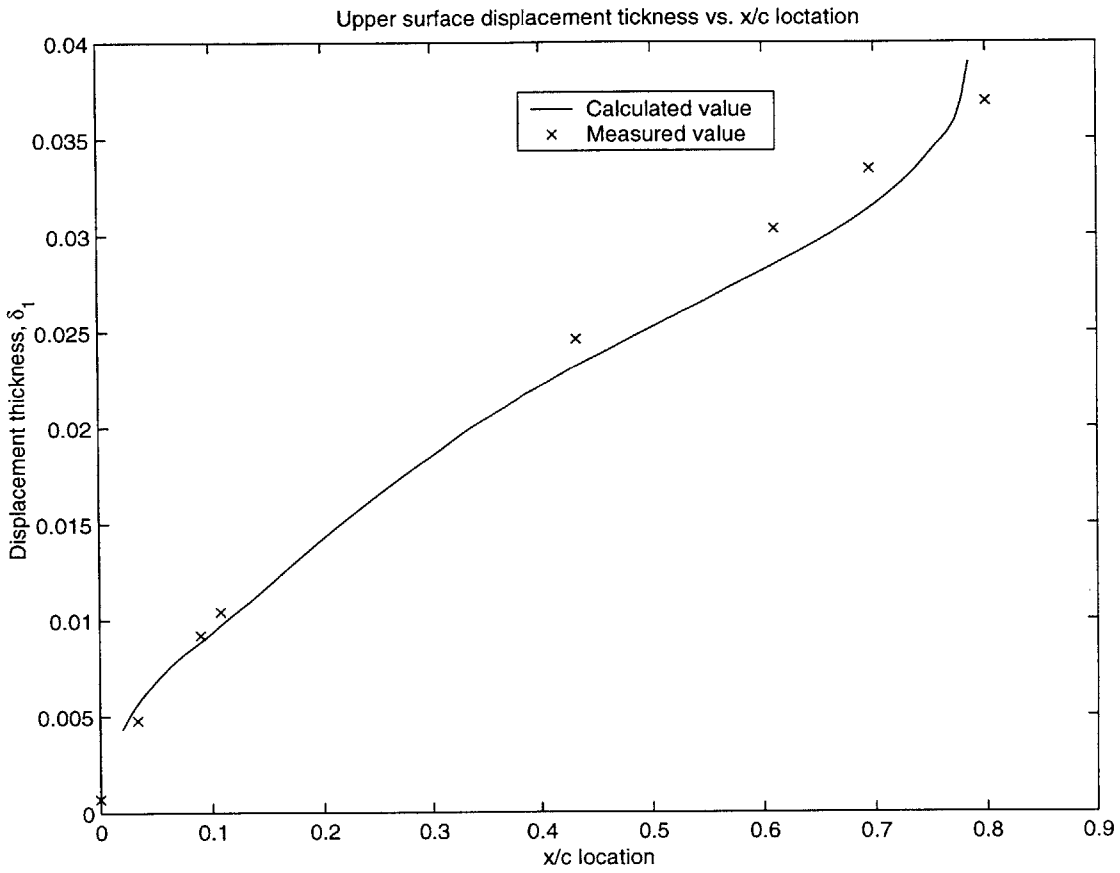

Figure 6-18: Displacement thickness vs. location on upper airfoil surface

The results indicate the vorticity integration method can find a displacement thickness that is in good agreement with the boundary layer thickness values that came directly from the CFD solution, especially on the upper airfoil surface. The maximum difference in thicknesses was 5% of the actual value on the upper airfoil surface and 10% on the lower airfoil surface. It seemed that the largest deviation occurred at the locations where the boundary layer was the thickest. This may have been because of the second order smoothing introduced to keep the numerical technique stable. Results were also not very accurate near the trailing edge because of the rapidly changing normals and the concentration of oddly shaped elements in

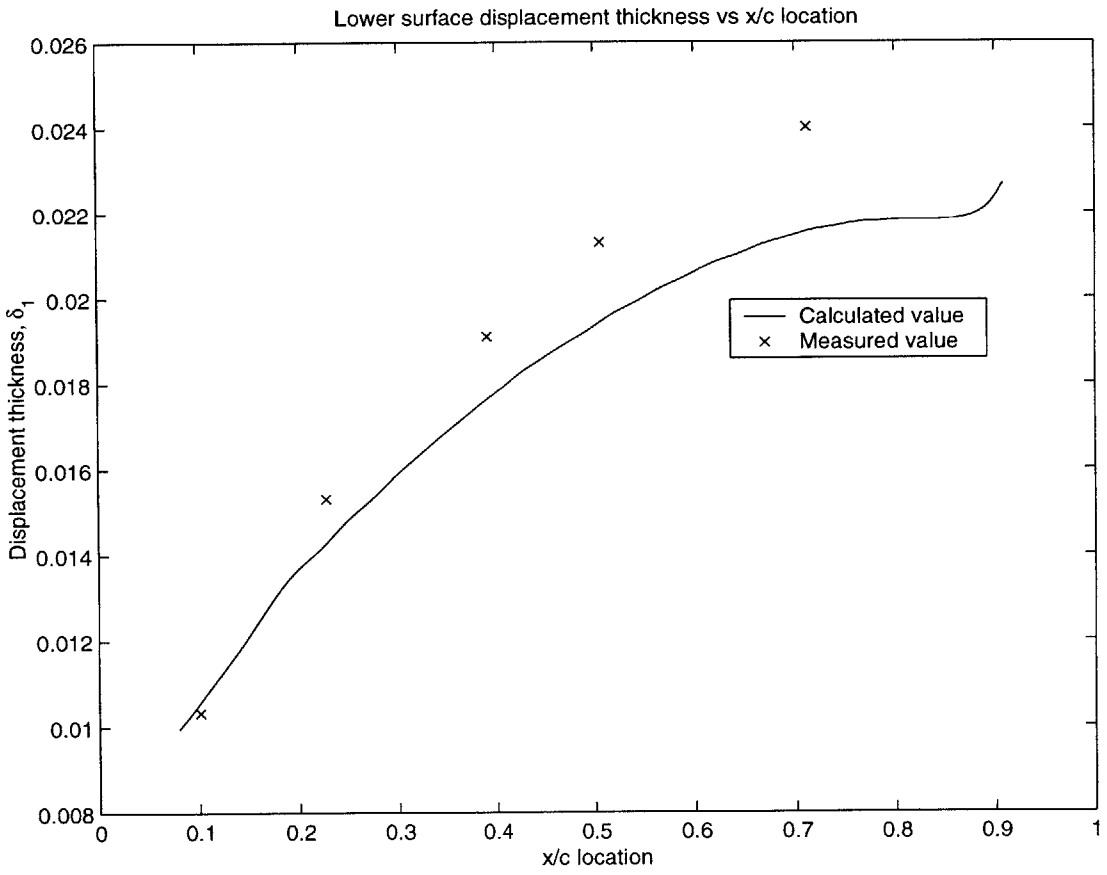

Figure 6-19: Displacement thickness vs. location on lower airfoil surface

this area.

Chapter 7

3D Boundary Layer Detection

The few analytical quasi 3D and fully 3D solutions of the Navier-Stokes equations that have been calculated provide good material for testing the boundary layer detection method previously described. Of particular importance is determining if the free stream velocities in these flows can be accurately estimated by integrating components of the vorticity vector. The accuracy of the displacement thickness approximation is dependent on the approximation to the free stream velocity. The free stream value is used for both calculating the integrand in equation 7.1 and in determining the end point of integration. The boundary layer thickness, δ was chosen as the point where the local velocity magnitude equals the free stream value.

$$\delta_1 = \int_0^{\delta} (1 - \frac{u}{U}) dl \tag{7.1}$$

7.1 Axisymmetric Stagnation Flow

As a preliminary to more complex three dimensional flows, the boundary layer detection method was tried on the simple axisymmetric stagnation flow, where the exact solution to the Navier-Stokes equation is known (see Schlicting [4]). The model of the problem is shown in figure 7-1. The potential flow conditions in the far field are shown in equation 7.3, where U is the freestream velocity in the r direction, W is the

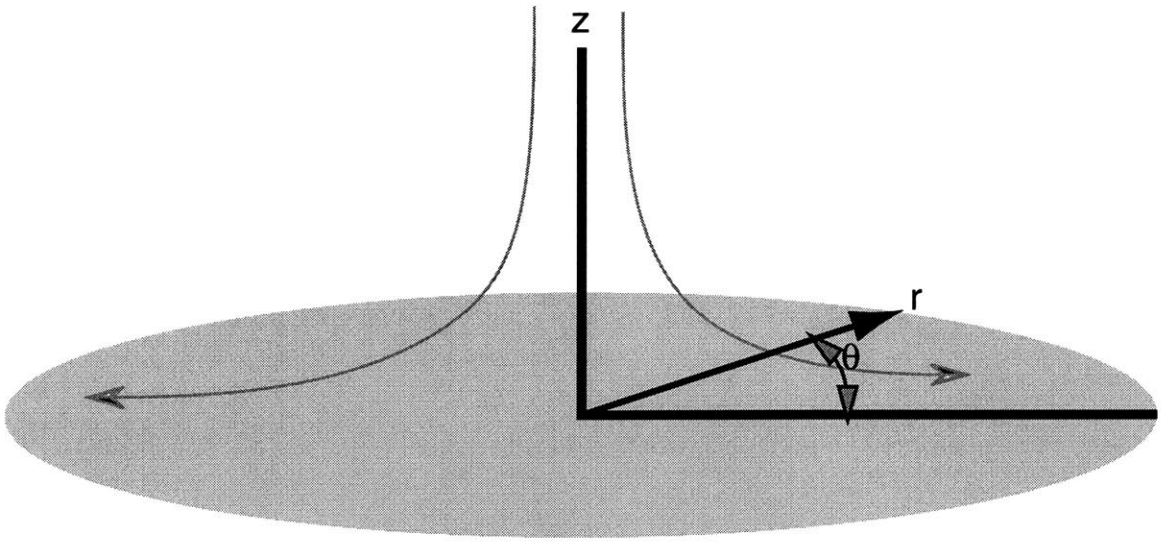

Figure 7-1: Stagnation flow model geometry

freestream velocity in the z direction, and a is an arbitrary constant.

$$U = ar \tag{7.2}$$

$$W = -2az \tag{7.3}$$

The Navier-Stokes equations were applied with the no slip boundary conditions on the plate, yielding and ordinary differential equation that is a function of z alone, so solutions are in the form $f(z)$. The velocity field components can be expressed as functions of $f(z)$, $f'(z)$, and r as shown in equation 7.5, where u_r is the velocity along the r axis, and u_z is the velocity in the z direction.

$$u_r(r,z) = rf'(z) \tag{7.4}$$

$$u_z(r,z) = -2f(z) \tag{7.5}$$

The equations are usually non-dimensionalized by defining a new variable $\zeta = \sqrt{\frac{a}{\nu}}z$ and a new function $\psi(\zeta) = \frac{f(z)}{\sqrt{a\nu}}$. The equation for $\psi(\zeta)$ can be solved numerically. To apply the boundary layer detection method that has been developed, it is necessary to integrate the vorticity from the plate, $z = 0$, out to infinity. Using the solution for the velocity components, and the definition for vorticity in cylinderical coordinates,

it is possible to find a relationship between the voritcity, some of the constants of the flow, and the $\psi(\zeta)$ function.

$$\omega = r\sqrt{\frac{a^3}{\nu}}\psi''(\zeta) \tag{7.6}$$

The approximation used in the detection method is that the free stream value, U can be approximated by integrating the vorticity from the plate to infinity.

$$U = ra \approx r\sqrt{\frac{a^3}{\nu}}\int_0^\infty \psi''(\zeta)dz \tag{7.7}$$

Changing the vorticity integration to an integration in ζ yields the following result for the integral.

$$\int_0^\infty \psi''(\zeta)dz = \sqrt{\frac{\nu}{a}}\int_0^\infty \psi''(\zeta)d\zeta \tag{7.8}$$

The integral is then easily tractable because $\psi'(\zeta) = 1$ from Schlicting [4], causing the integrated vorticity value to be equal to ra, the exact solution. For this case, there will be no difference between the actual values and using the integrated vorticity to determine the free stream velocity, the displacment thickness, or the momentum thickness.

7.2 Axisymmetric Stagnation Flow With Swirl

Another case where the boundary layer thickness can be determined analytically is the case of the stagnation flow field around a rotating disk shown in figure 7-2. This is truely a three dimensional boundary layer, with all three velocity components dependant on the three coordinates in the model. The solution is presented in [4] and yields equations for the velocity components related to the parameter ζ in equation 7.9, where w is the angular velocity of the plate and ν is the kinematic viscosity.

$$\zeta = z\sqrt{\frac{w}{\nu}} \tag{7.9}$$

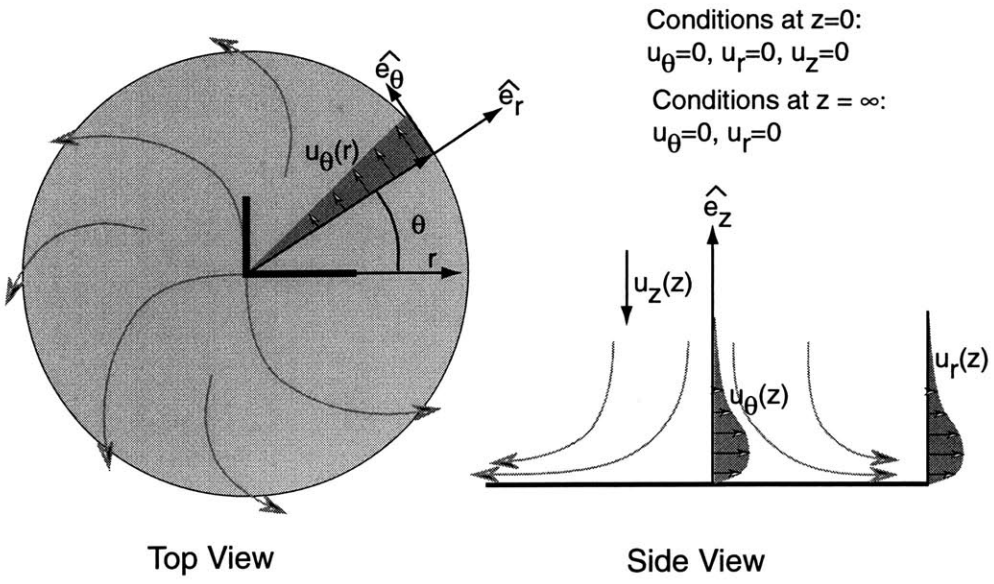

Figure 7-2: Stagnation flow model with swirl

The three velocity components are presented in equation 7.12 as a functions of ζ.

$$u_r = rwF(\zeta) \tag{7.10}$$

$$u_\theta = rwG(\zeta) \tag{7.11}$$

$$u_z = \sqrt{w\nu}H(\zeta) \tag{7.12}$$

The free stream velocity conditions are governed by the values of the functions F,G,and H as ζ or z goes to infinity. The radial component of the velocity goes to zero in the free stream because $F(\infty) = 0$. Similarly, the swirl component of the flow, u_θ goes to zero as z becomes large. In this flow situation, the primary flow direction will be chosen as the r direction and the θ direction will be the crossflow component of velocity. The component of vorticity that is used to calculate the primary boundary layer thickness is ω_θ, which is computed in equation 7.14. The cross flow component of the boundary layer is calculated with the $-\omega_r$ component of the vorticity vector, described in equation 7.13.

$$\omega_r = -r\sqrt{\frac{w^3}{\nu}}G'(\zeta) \tag{7.13}$$

$$\omega_\theta = r\sqrt{\frac{w^3}{\nu}}F'(\zeta) \tag{7.14}$$

If the ω_θ component of vorticity is integrated from 0 to some value of ζ, the result is an equation that exactly equals how the u_r component varies with ζ as shown in equations 7.15 and 7.16. This implies that the free stream u_r velocity component can be exactly described by integrating vorticity from zero to infinity.

$$u_r(\zeta) = r\sqrt{\frac{w^3}{\nu}}F(\zeta) \tag{7.15}$$

$$u_r(\zeta) \approx \int \omega_\theta d\zeta = r\sqrt{\frac{w^3}{\nu}}F(\zeta) \tag{7.16}$$

Similarly, the cross flow component of the velocity in the θ direction exactly equals the integration of the $-\omega_r$ component of the vorticity vector.

$$U_\theta(\zeta) = r\sqrt{\frac{w^3}{\nu}}G(\zeta) \tag{7.17}$$

$$U_\theta(\zeta) \approx -\int \omega_r d\zeta = r\sqrt{\frac{w^3}{\nu}}G(\zeta) \tag{7.18}$$

The method for computing the free stream velocity values from vorticity components works exactly for the three dimensional case of flow over a rotating plate, implying that the method for determining the displacement thickness in the r and θ direction will be exact.

Chapter 8

Integration Methods

This chapter deals with some of the numerical issues involved with integrating along curves and over regions. Since this thesis focuses on describing the boundary layer from the results of CFD solutions, it is necessary to determine how refined the model must be to get an accurate estimate of the boundary layer thicknesses.

8.1 One dimensional test problems

A small numerical experiment was done to determine the dependence of the error in displacement and momentum thickness on the number of integration points within the boundary layer. The Blasius velocity profile was integrated at some fixed x location to see how the number of points used in the integration effected the boundary layer thickness estimates. As shown in figure 8-1 the difference in theoretical and calculated values of the displacement thickness is linear with the element thickness. The accuracy of the estimation varies with $\frac{1}{h}$, where h is the element length. The momentum thickness error was slightly different, in that it varied with $\frac{1}{h^{\frac{3}{2}}}$ as shown in figure 8-2. The accuracy of the boundary layer estimation is limited by the displacement thickness error, and seems to require very many integration points for an estimate within 5% of the theoretical value. The values of the constants in the vorticity and velocity equations play a role in determining the number of integration points necessary. For this case, the constant values are presented in table 8.1.

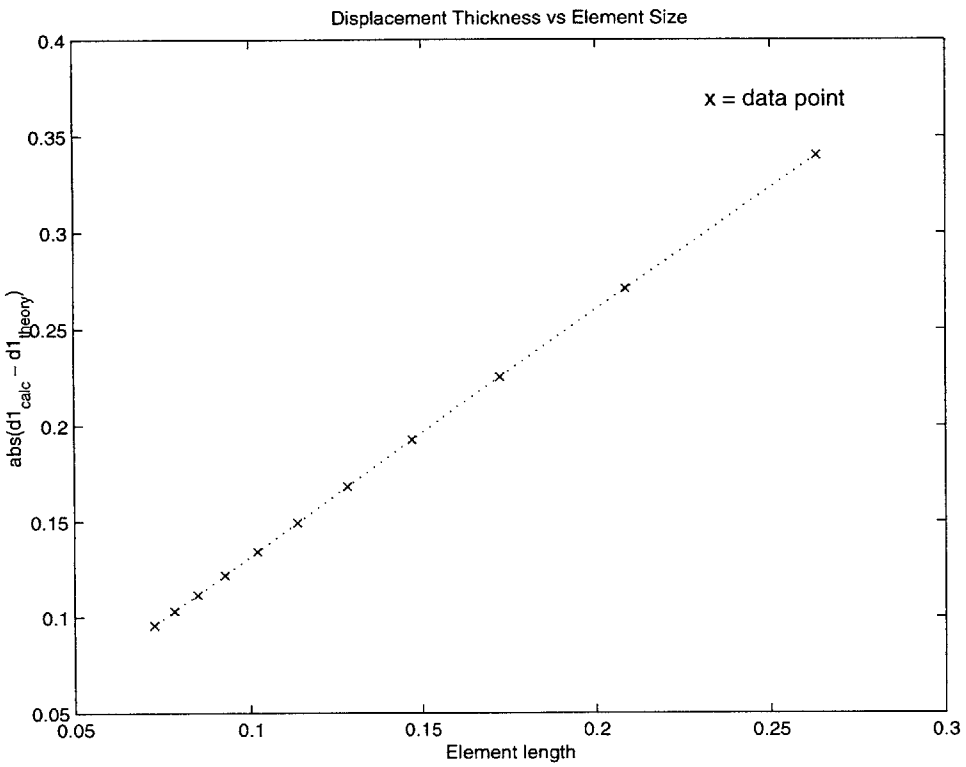

Figure 8-1: Element length vs. the error in displacement thickness

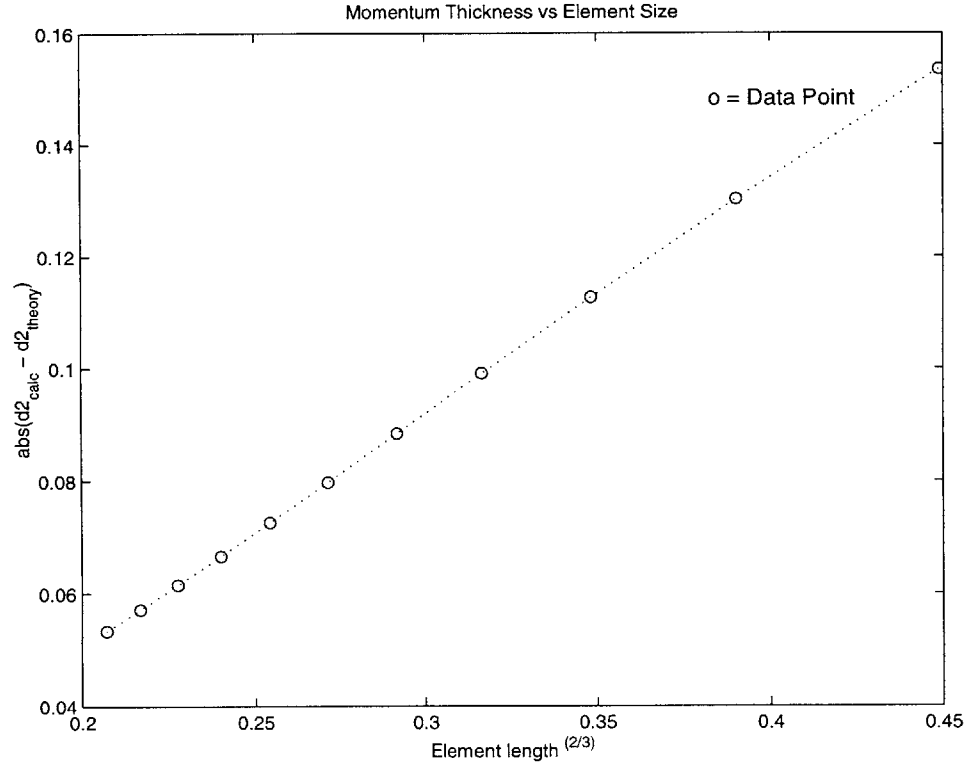

Figure 8-2: Element length vs. the error in momentum thickness

parameter	value
$\frac{dP}{dx}$	1
R	5.0
μ	0.1

Table 8.1: Boundary Layer Integration Parameters

With this combination of constants, 100 integration points were needed to get an displacement thickness error within 5% of the actual figure. Unfortunately, this degree of resolution is not typically available from CFD results, so some more accurate method must be developed.

8.2 Boundary layer integration as a solution to the convection equations

Generalizing the displacement and momentum boundary layer definitions to three dimensions results in a few volume integrations. Equation 8.1 is a generalized displacement thickness calculation, assuming a constant density. Equation 8.2 is a similar relation for the momentum thickness. The elemental volume, dV, under consideration is shown in figure 8-3.

$$\frac{\dot{m}}{\rho} = \int_0^\delta u dV = \int_{\delta_1}^\delta (U) dV \tag{8.1}$$

$$\int_0^\delta (u^2) dV = \int_{\delta_2}^\delta (U^2) dV \tag{8.2}$$

For practical reasons, it was necessary to develop an easier way of doing these area integrals for 2-D problems and volume integrals for 3-D problems. As described previously, non-intersecting normal curves on the wall surface can be constructed by setting up and solving the LaPlace equation in two or three dimensions. Solving this equation yields values of a potential function, which has gradients that are perpendicular to the wall surface and aligned in the direction of integration. In some cases, it is

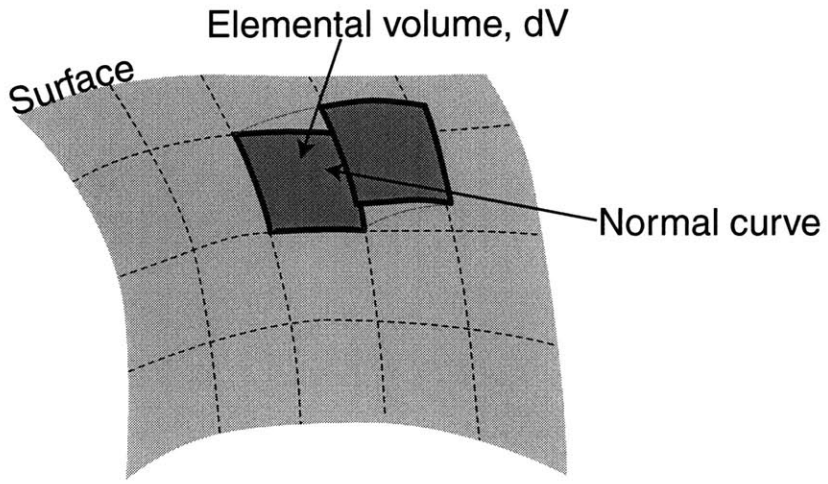

Figure 8-3: Boundary layer integration volume

possible to construct a stream function, ψ that is everywhere normal to the potential function, ϕ, and has tangency to the gradient of the potential function. The area or volume integrals needed to calculate δ_1 and δ_2 can be transformed into this new ϕ,ψ coordinate system. Equation 8.3 is a statement of the equivalence of the area integrals for the two coordinate systems.

$$\int_\Omega dxdy = \int_\Omega d\phi d\psi \tag{8.3}$$

The difficulty in evaluating these integrals is in constructing the stream function from the potential function; adding complexity and overhead to the calculation. Fortunately, there is another way to approach the integration that does not use the stream function directly, but only the gradient of the potential function. This is basically done by looking at the integration problem with an Eulerian view; allowing the values to march toward the starting point of streamline and adding up the results that convect by that point.

8.2.1 1D model

In order to introduce the technique, the first topic will be a simple integration of a scalar function of one variable, $q = q(x)$, shown in figure 8-4. The value of interest

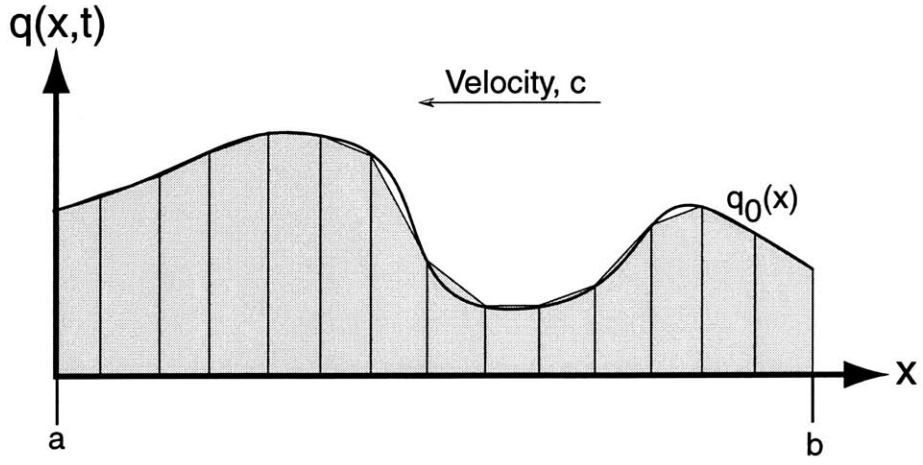

Figure 8-4: Function integration as convection

is the integrated value Q and is typically calculated with $Q = \int_a^b q dx$. Instead of integrating with respect to x, what if the entire curve were moving to the left with a constant velocity c? In that case, q becomes an equation of x and t, and conforms to the linear wave equation.

$$\frac{dq}{dt} + c\frac{dq}{dx} = 0 \tag{8.4}$$

The solution to this equation is the following, where $q_0(x)$ is just the function at the initial time.

$$q(x - ct) = q_0(x) \tag{8.5}$$

The original integral was evaluated from $x = a$ to $x = b$, and by changing the limits of integration, $q(x, t)$ can be integrated in time to yield the same result.

$$Q = \int_a^b q_0(x)dx = \int_0^{\frac{a-b}{c}} q(a - ct)dt \tag{8.6}$$

Because the function, q now varies with x and t, a boundary condition has to be imposed on the integral. This new boundary condition does not allow information to come from outside the initial conditions; $q(b) = 0$ for $t > 0$.

Using this method, the original integral can be transformed from an integration in space to an integration in time by introducing a velocity to the original solution $q_0(x)$. There yields no real advantage for this particular case. However, in the current application of boundary layer integration, the exact path of integration is not know, only a vector field tangent to the integration paths. It then becomes easier to reverse the vectors and convect values of interest back to the beginning of the streamlines.

8.2.2 Higher dimensions

Just as the integration of a function of one spatial variable can be changed into a time integral, any integration over a domain can be changed into an integration in time. The Gauss equation relates the time and spatial change of a field variable within a domain and is restated in equation 8.7. In this equation, Ω is the domain of the problem, dA is an elemental piece of the domain, $d\Omega$ is the boundary of the domain, q is the value being integrated, and c is the velocity vector.

$$\frac{d}{dt}\int_{\Omega} qdA = \int_{d\Omega}(qc_i \cdot \hat{n})ds \tag{8.7}$$

The integration on the boundary of the domain can be restated as an integration of the flux on the boundary with the following equations, 8.8 and 8.9.

$$\frac{dq}{dt}\int_{\Omega} qd\Omega = -\int_{d\omega}(Fdy - Gdx) \tag{8.8}$$

$$Fdy - Gdx = Fluxout \tag{8.9}$$

If both sides are integrated with respect to t, the desired integral is shown to be equivalent to a time integral of the flux around the boundary of the domain, eqn 8.10.

$$Q = \int_0^{\infty}\int_{\omega}(\frac{dQ}{dt})dt = -\int_0^{\infty}(Fluxout)dt \tag{8.10}$$

Figure 8-5 is a representation of a typical two dimensional domain for an integration problem that is solved as a time integration.

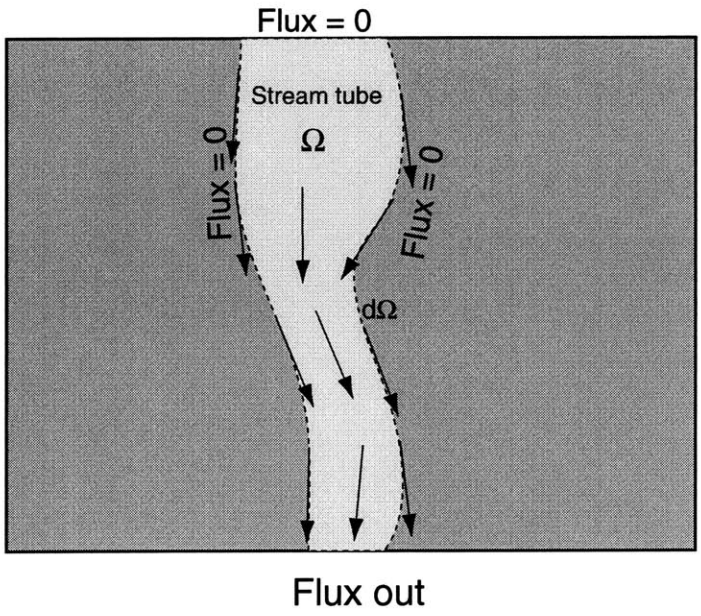

Figure 8-5: Area integration as a solution to the convection equations

Boundary conditions for the higher dimensional problem are similar to the one dimensional case. If $(c_i \cdot \hat{n}) < 0$ then the $q = 0$ for $t > 0$, since only quantities inside the domain should get integrated. No boundary condition should be imposed on parts of the boundary where $c_i \cdot d\Omega > 0$, corresponding to an outflow condition.

8.2.3 Discretizing the equations

The first step in applying the integration method is to discretize the domain and the time variable. The discrete problem can be solved in any number of ways, see for example [7], but for this particular case the method chosen was to do a finite volume discretization on a domain decomposed into triangular elements. Integrating the differential form of the governing equation, 8.11 yields equation 8.12.

$$\frac{dq}{dt} = c_i \frac{dq}{dx_i} \tag{8.11}$$

$$\int_\Omega (\frac{dq}{dt} + c_i \frac{dq}{dx_i}) d\Omega \tag{8.12}$$

The integral of the divergence of q can be converted to a integral around the domain as shown in equation 8.13 for a two dimensional problem.

$$\int_{\Omega} \frac{dq}{dt} + \int_{d\Omega} (c_1 q n_x + c_2 q n_y) ds = 0 \tag{8.13}$$

If the integral around the domain is performed in a counterclockwise direction, the normal vector has the components in equation 8.14.

$$\hat{n} = \frac{dy}{ds}, -\frac{dx}{ds} \tag{8.14}$$

Using this definition of the normal vector, the final integral can be arranged as shown in equation 8.17

$$\int_{\Omega} \frac{dq}{dt} = -\oint (F dy - G dx) \tag{8.15}$$

$$F = c_1 q \tag{8.16}$$

$$G = c_2 q \tag{8.17}$$

This equation can be applied to discretized domains shown in figure 8-6 to produce the spatially discrete version of the equation. For a typical node, J in the domain, this might reduce to the discrete equation 8.18.

$$\begin{aligned} A_j \frac{dq_j}{dt} + (F\delta y - G\delta x)_{KL} & \\ + (F\delta y - G\delta x)_{LM} + (F\delta y - G\delta x)_{MN} & \\ + (F\delta y - G\delta x)_{NO} + (F\delta y - G\delta x)_{OK} = 0 & \end{aligned}$$

Moving the values with respect to time simulates the motion along a streamline, so a high order accuracy time stepping method is recommended to more closely follow the streamline curves. In this particular case, a fourth order Runga Kutta method was used. The time step should be constant over the domain, and small enough to satisfy stability constraints. The choice of time step also affects accuracy, as the direction of integration more closely follows the desired vector field when the time

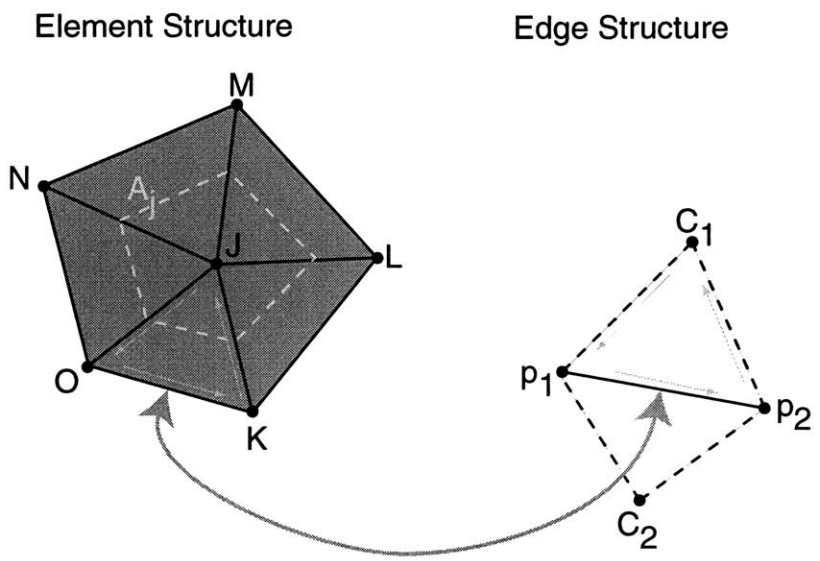

Figure 8-6: Typical Triangulated Domain

step is small.

8.2.4 Corner flow test case

The two dimensional problem representing corner flow from chapter 5 was used to validate the new integration method. As a check, the area of the unit square was calculated using the new method; summing the fluxes across the boundary streamlines shown in figure 5-9. Figures 8-7 and 8-8 show the domain after 10 and 30 iterations, respectively. It is clear that the values have begun to move toward the corner, where the flux will be summed and used to approximate the area between the streamlines.

The fluxes summed on the wall boundary represented the stream tube area, and are shown in figure 8-9. The total area was calculated by summing the areas collected on the wall boundary, and was close to the actual value of 1 to within 0.1%.

The choice of the numerical scheme used to solve the linear convection equation effects the results of the area integral. As an example, numerical smoothing was applied to the square area integration model. Figure 8-10 shows the converged convection solution values for both a smoothed and undamped case. The undamped case shows large areas where the values go beyond the narrow boundaries of the smoothed solution, even though they should be uniformly zero. With smoothing, the

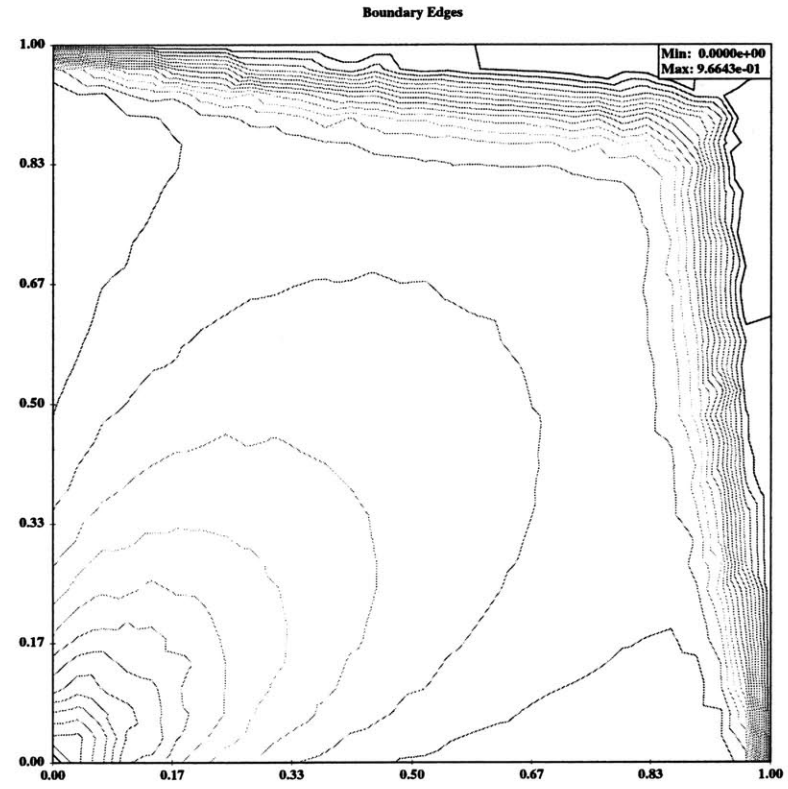

Figure 8-7: Area convection results after 10 iterations

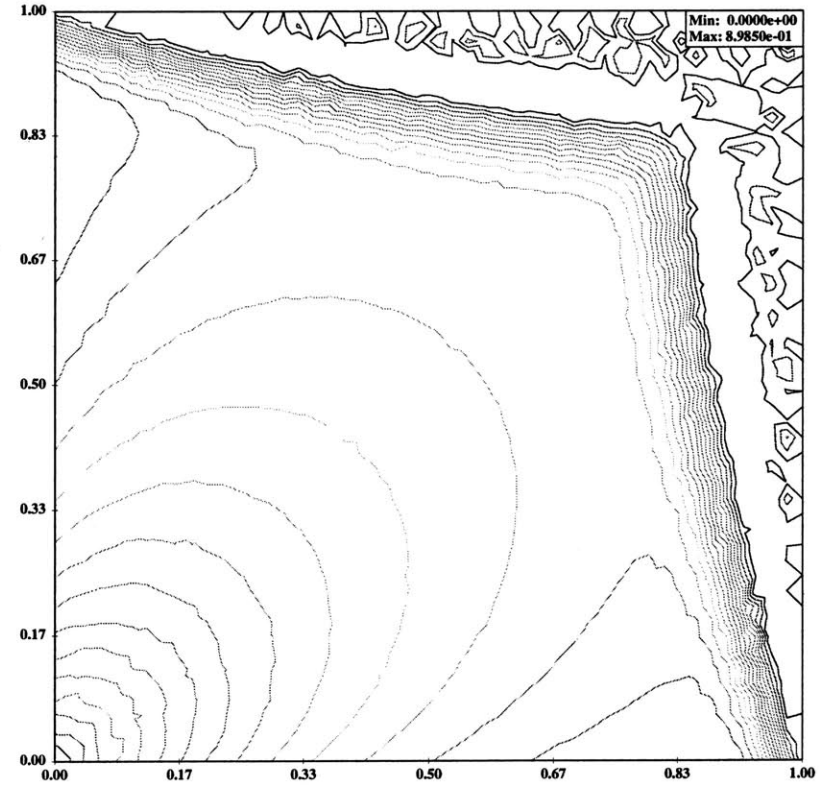

Figure 8-8: Area convection results after 30 iterations

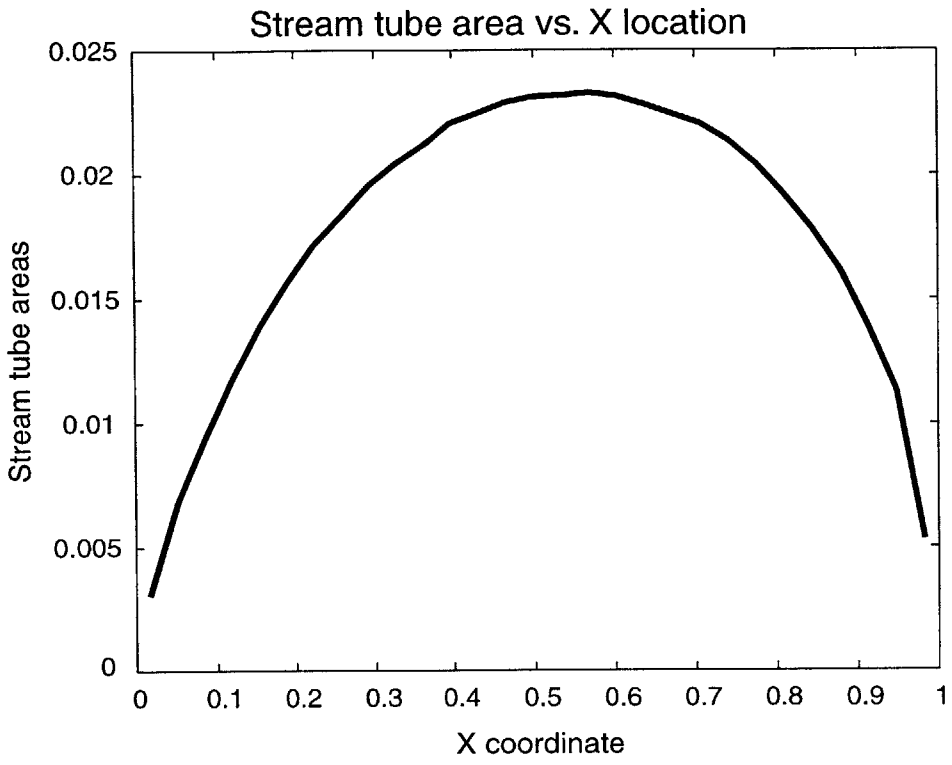

Figure 8-9: Convected area calculation

solution converges more quickly and the end result is a more uniform field of values.

Second order smoothing was chosen for this example because it can show up in many convection equation solution procedures and is the most detrimental for this integration method. The second order terms cancel the high frequency noise effectively, but also damp out some of the lower frequency information, depending on the constant used in the method. The higher the damping constant, the more smoothing takes place. Unfortunately, because the damping has smoothed over the convected values, the error in the total area calculation increases with increasing damping. Figure 8-11 shows the effect of changing the damping on the calculated area. At time $t = 1$, the discontinuity at the boundary has begun to convect toward the right, but as it is doing so, the values are smoothing out due to the dissipation. All values at the left boundary get set to zero, so the approximated discontinuity gets truncated, removing some of the area from the integral.

With the convection calculation yielding the correct values for the area calculation,

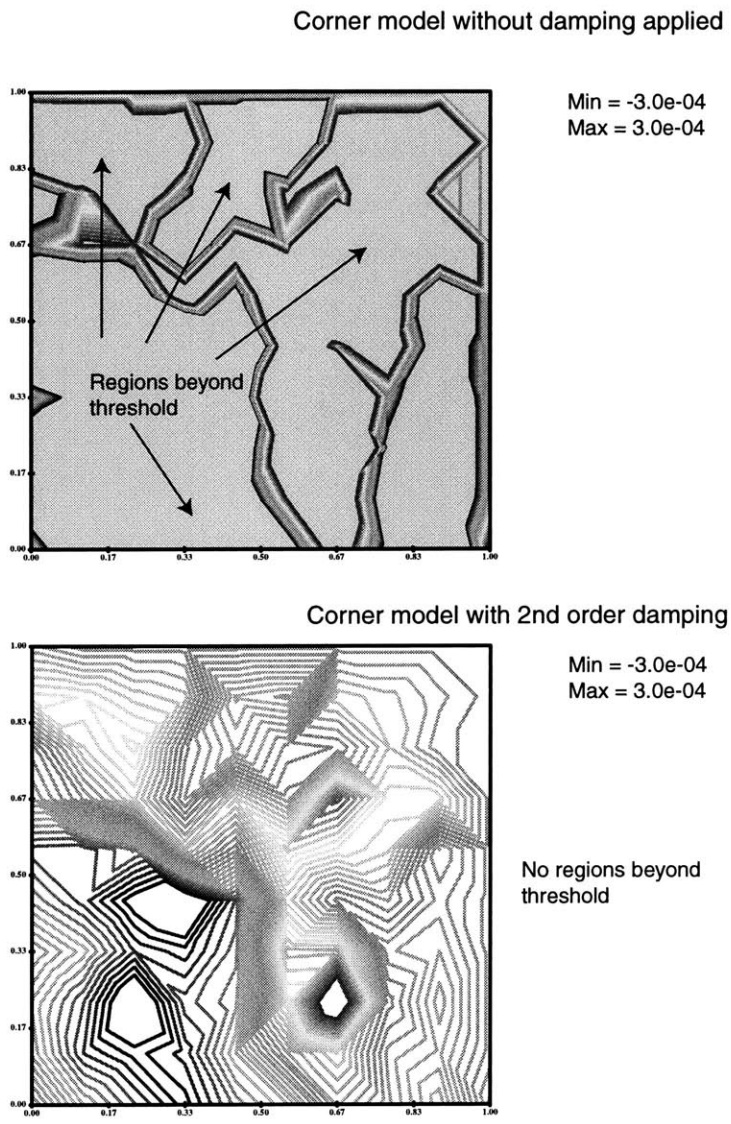

Figure 8-10: Convection values without damping: Area = 1.01, with damping: Area = 0.97

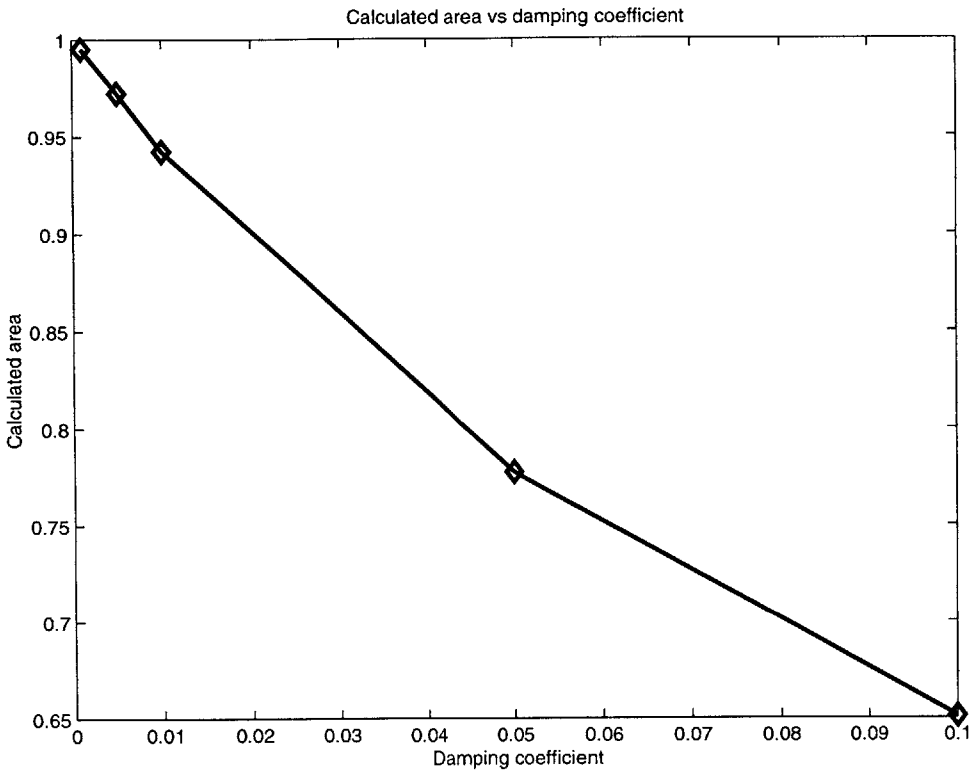

Figure 8-11: Dissipation constant vs. integrated area value

a full displacement thickness calculation was carried out with the results in figure 8-12. The calculated results were not a good fit at the edges, where x goes to 0.0 and x goes to 1.0 because the streamlines that are being integrated on go outside the domain before they reach the edge of the boundary layer. The calculated values are also not an excellent fit at the corner of the curve. This is because the streamlines become very close in this region, requiring more elements to fully resolve it. The method was also applied to a coarser grid, to see how the grid resolution affected the results. Surprisingly, the curve fit was much the same as for the more refined grid, as can be seen in figure 8-13.

8.2.5 Laminar airfoil test case

The convection integration technique was used during the calculation of the displacement thickness on both the airfoil models of chapter 6. Figure 8-14 shows how the contours of vorticity change as the convection proceeded along the $\nabla\phi$ vectors radi-

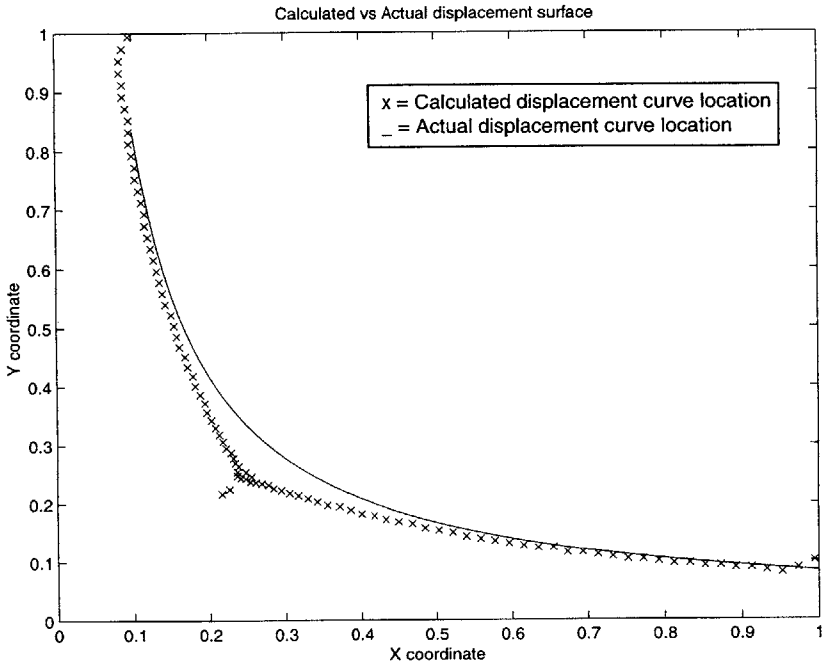

Figure 8-12: Displacement thickness curve

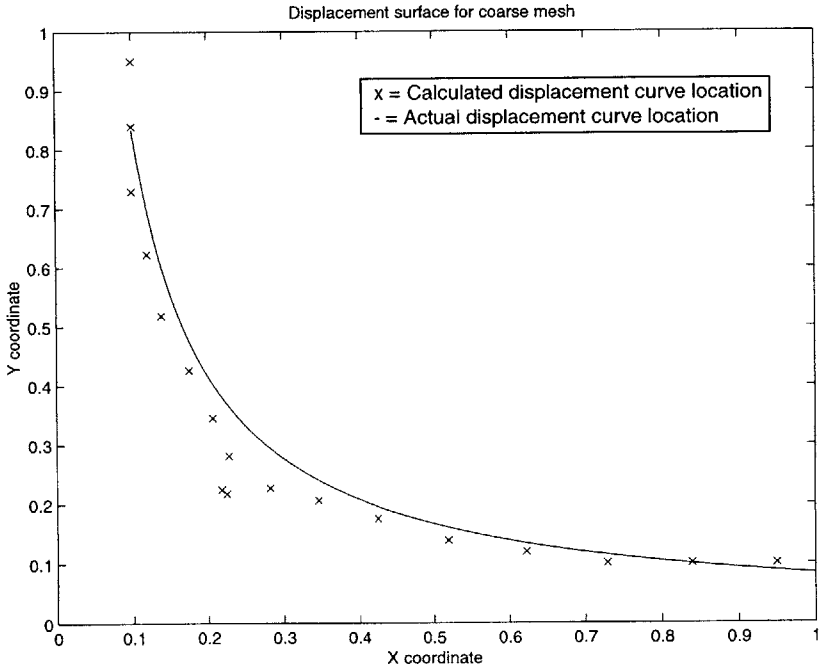

Figure 8-13: Displacement thickness curve for coarse grid

ating from the airfoil. The grid around the model was a C shaped grid that made it possible to extend the airfoil edge all the way to the boundary of the model as shown in figure 8-15. This was done to keep the normal curves from changing direction radically at the trailing edge point. The flux of the vorticity through the

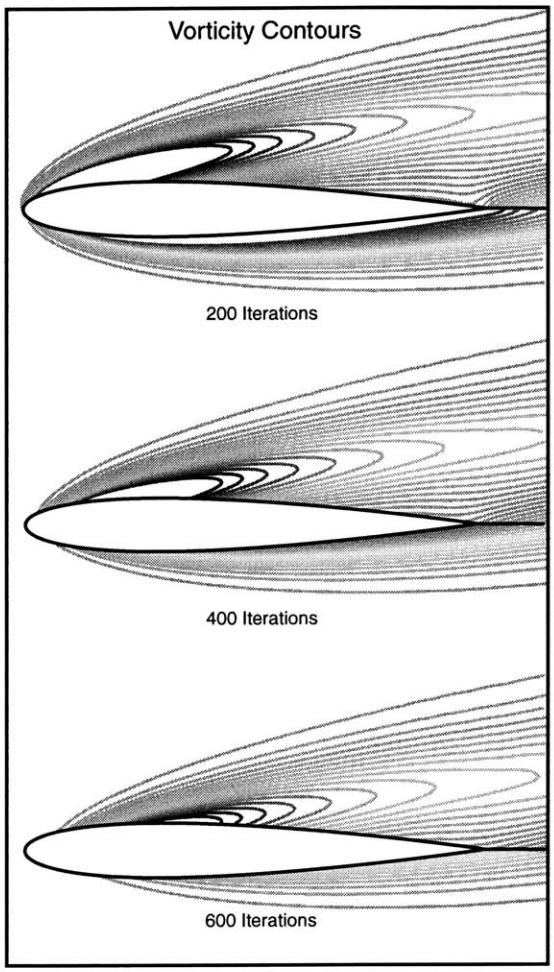

Figure 8-14: Convecting vorticity on a laminar airfoil model

airfoil edges was calculated at each time step, and summed to estimate the vorticity of the elemental areas between values of ϕ. After the flux was summed, the value was divided by the edge length for an estimate of the free stream velocity. The free stream velocity was then used to calculate the displacement thickness.

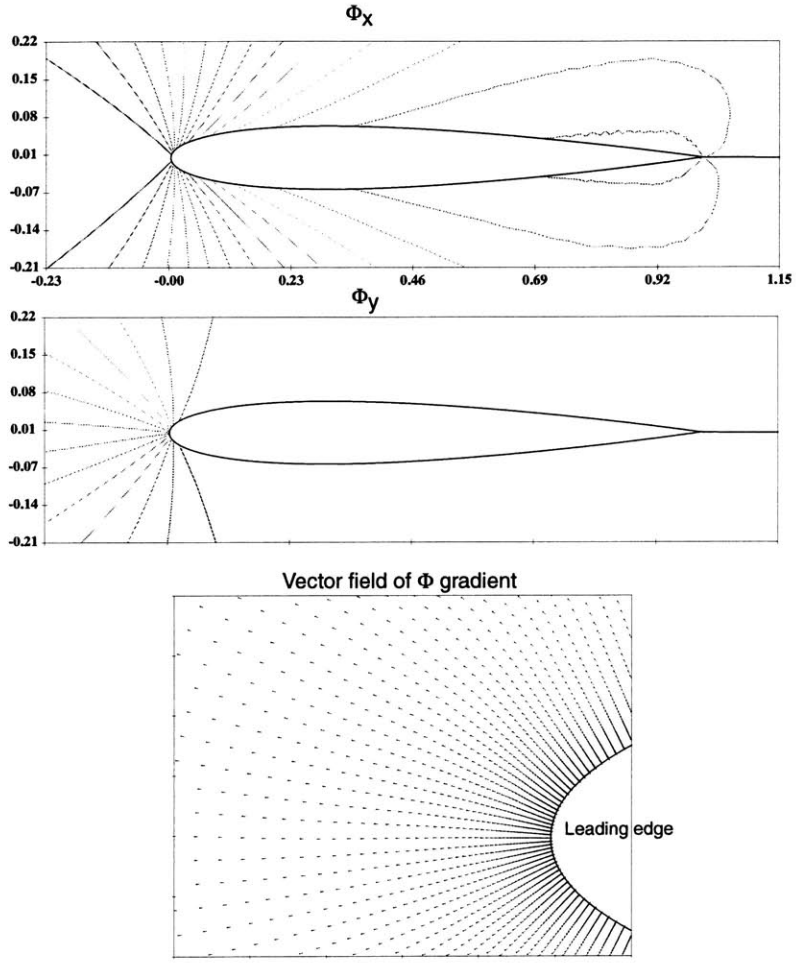

Figure 8-15: Normal curves used for convecting vorticity on the laminar airfoil model

8.2.6 Turbulent airfoil test case

The same calculation procedure was applied to the turbulent airfoil model to obtain the free stream velocity and displacement thickness approximation presented in chapter 6. Figure 8-16 are the normal curves used to convect the voriticty values. The trailing edge of this airfoil model is very sharp, making the normal curves highly

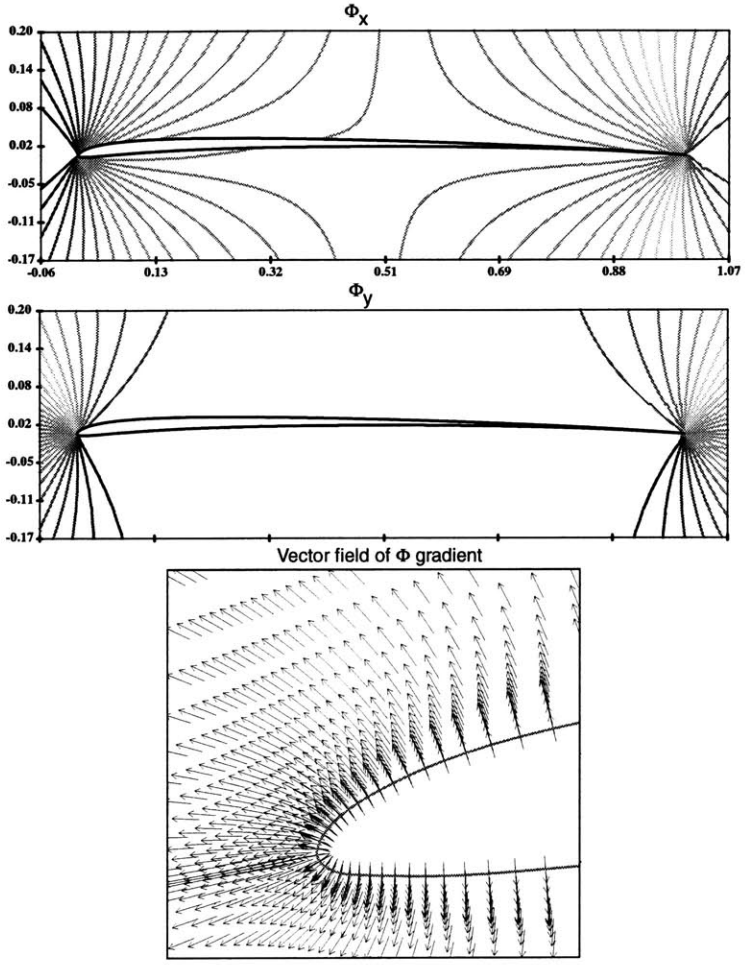

Figure 8-16: $\nabla\phi$ solution for convection velocity

distorted in this region. In fact the value of $\nabla\phi$ is non-unique at the trailing edge. Because the curves were distorted, the calculated free stream velocity and displacement thicknesses were not as accurate near the trailing edge of the airfoil.

Figure 8-17 shows the convection equation solution at different time steps.

The numerical methods used for integrating the vorticity can be easily used to integrate any quantity along a stream tube or stream line. One other possible use

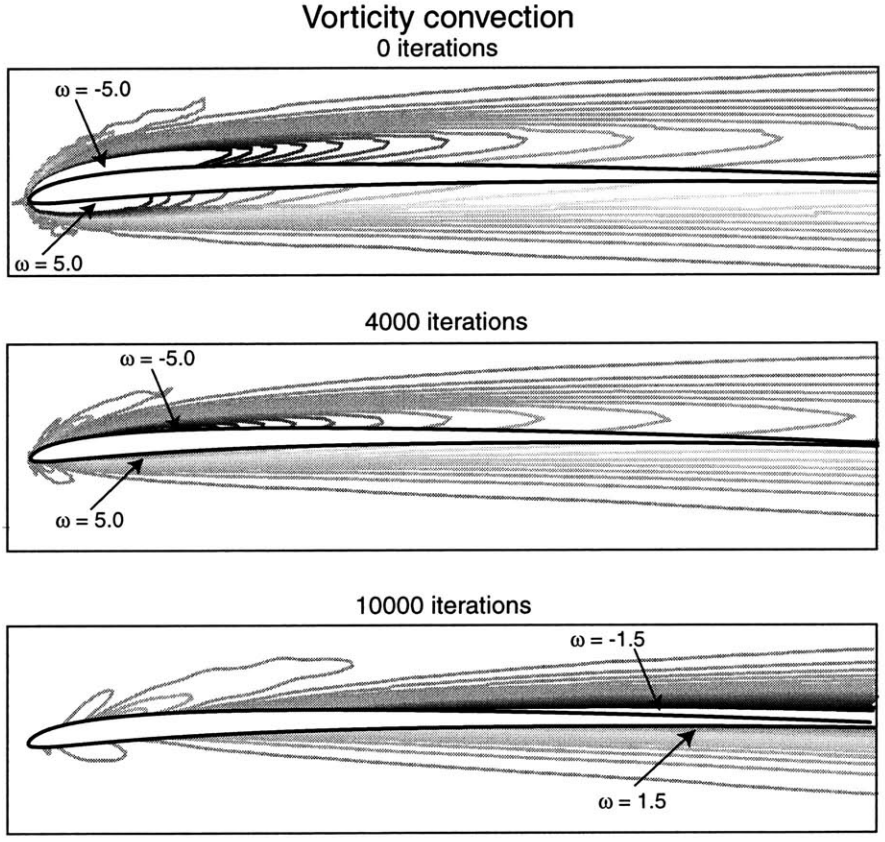

Figure 8-17: Convecting vorticity on a turbulent airfoil model

is to find the locations in the flow where certain quantities are being generated; for example, locations of heat or entropy generation. By convecting the scalar value in the opposite direction of the gradient of that scalar, it will eventually wind up at the initial source.

8.2.7 Time dependant problems

The boundary layer detection technique can be applied to transient CFD solutions as well, by simply applying the detection technique to each individual time step of the solution. Unfortunately, it is not possible to advance the vorticity convection solution at the same as the actual CFD solution is progressing in time, since the vorticity is being convected along different streamlines that are not related to the streamlines in the solution.

There are however some ways to speed up the calculations. One of these is to restrict the computational domain to regions around the body where the vorticity is non-zero. By restricting the domain, the distance that the values have to convect is smaller, and so the number of computation intervals is reduced. This technique was used on the turbulent airfoil model, since the boundary layer was such a small fraction of the chord length of the airfoil.

Another difficulty using this technique on time dependant problems is the problem of choosing the appropriate reference frame. Some of the vorticity components are being used to estimate the rate of velocity change normal to the body surface. However, if the body is in motion relative to the coordinate system used to calculate the vorticity components, this may not be a good assumption. The vorticity has to be calculated with respect to the body frame of reference.

It should be noted that while the shape of the boundary layer depends strongly on the history of the flow, using the vorticity to estimate the boundary layer thickness does not. The instantaneous values of displacement or momentum thickness do not depend on the rate of change of any of the velocity components. Since the vorticity is used to estimate these velocity components in the boundary layer, the rate of change of vorticity is not important in time dependant problems.

8.2.8 Other three dimensional issues

Certain vortical structures must be rejected in order to use the vorticity to estimate the free stream velocity and boundary layer thickness. For example, on a finite wing, the vortices created in the boundary layer will turn near the edges and start flowing downstream, creating the familiar trailing edge wing vortex. This vortex, while generated in the boundary layer should clearly not be included with it. For this reason, only the component of the vorticity normal to both the solid surface and the local velocity vector are needed to estimate the change in velocity through the boundary layer. Other sources of vorticity such as curved shocks and wake regions will have to be dealt with differently, mainly because they extend the vorticity field beyond the boundary layer. When the vorticity does not go to zero in the free stream, other assumptions have to be made in order to put an upper boundary on the vorticity integration and produce an estimate for the free stream velocity.

8.3 Summary of Boundary Layer Detection Technique

This section outlines the steps involved in calculating the displacement thickness as a function of the location on the body, and highlights some of the difficulties at each step.

- Setup and solve LaPlace's equation to find the potential function ϕ and the normal curves
    1. Use dirchlet conditions on the solid surface and in the far field
    2. Find the direction of the normals by finding the gradient of the potential, $\nabla\phi$
- Integrate the vorticity components to determine the free stream velocity.
    1. Sum the flux of the vorticity component normal to the wall to estimate the free stream velocity.

2. To get an idea of the cross flow in the boundary layer, sum the flux of the vorticity component tangent to the normal curves.

- Use the equation $\delta_1 dA = \int_0^\delta dV - \frac{1}{U}\int_0^\delta (u) dV$ to determine the displacement thickness.

    1. The variable dA refers to the elemental area on the wall surface.
    2. The thickness of the boundary layer, δ can be estimated by the location where the velocity equals the estimated free stream value; $u = U$.

Chapter 9

Conclusions

9.1 Shock Detection

The stationary shock finding algorithm does not produce a shock surface that would reflect the shape of the shock in the physical flow, but because of numerical approximation, shows a shock region. The thickness of the region can give information about the quality of the solution and location of needed mesh refinement. Any dispersion and dissipation in the solution is reflected in the shape and size of the shock region. Dissipation tends to enlarge the marked shock region, while dispersion creates spurious shock indications upstream and downstream of the actual shock.

The nature of the solutions and the susceptibility of the shock detector to small errors in the solutions make filtering a requirement, especially in transient solutions. However, it was determined that filtering to enforce jump conditions and shock direction is not as attractive and effective as a simple threshold on the pressure gradient magnitude. The heuristic method of determining this threshold that was presented in chapter 4 was effective on the models tested.

Shock finding based on fluid dynamic principles is practical, with some advantages over more general edge detection methods, but still requires filtering of the results.

9.2 Boundary Layer Description

Boundary layer thicknesses can be related to a momentum or mass deficit that are of interest to designers and analysists, but only by redefining quantities like the displacement and momentum thickness to include more complex geometries. The main failure of those boundary layer descriptions being their inability to take into account a curvature of the solid surface. For curved surfaces, a volume integral can be used to deal with complex geometry. For some geometries, like concave surfaces, normal vectors will intersect each other making it difficult to find a differential volume. To deal with the situation, the LaPlace operator to construct curves that are normal to the wall surface, but are guaranteed not to be self-intersecting.

One of the difficulties in determining the boundary layer thickness is finding the "free stream" velocity outside of the boundary layer. For the simple two and three dimensional flows examined; the free stream velocity was accurately estimated by integrating the vorticity components along curves normal to the wall, starting at the wall and going and out toward the boundary of the model. Indeed, in some cases this yields the exact free stream velocity, without error. Because the magnitude of vorticity usually asymptotically decreases to zero in the free stream, the choice of where to end the integration becomes less critical. However, choosing an end point for the integration becomes important in separated regions, downstream of a curved shock, or in wake regions where the free stream vorticity is not zero. It may be possible to negate these effects by ending the integration when the first or second derivative of the vorticity along the normal curve is zero.

The numerical technique introduced to integrate between normal curves proved to be useful for carrying out the displacement thickness calculations. Without using the convection technique, it would be necessary to explicitly find the region between the normal curves that extend from each point on the airfoil boundary. This could be done by constructing a stream function from each point, or by constructing a piecewise linear curve that starts at the boundary points and is tangent to the $\nabla\phi$ vectors. Then the area integrations would have to take place between each pair of

boundary curves. For three dimensional problems, it is necessary to perform a volume integration, which would necessitate finding the normal curves on all the elemental wall surface points and then constructing some sort of volume from these curves. By using the convection equations, these areas and volumes are implicitly defined, making the computation much simpler. Care is needed in selecting the numerical scheme for solving the equations. It needs to be stable and use as little dissipation as possible to maintain the accuracy of the final integral.

This method of boundary layer thickness estimation may also be applied to other regions of the flow where the mass and momentum deficit is of interest; as in wake regions. As long as normal curves can be defined from the center of the wake, the vorticity integration should yield the free stream velocity, which can be used to determine a mass and momentum deficit in the wake. The difficulty is determining the center of this wake, which may be possible for some simple flows like those behind an airfoil in high Reynolds number flow, but gets more complicated when other phenomena are occurring like vortex shedding or other time dependant phenomenon.

Future work needs to concentrate on applying the vorticity integration technique to more complex three-dimensional CFD solutions. For the two dimensional cases chosen, integrating the vorticity seems to be the most direct and unambiguous way of estimating the free stream velocity and the boundary layer thickness.

Bibliography

[1] Ma Kwan-Liu, John Van Rosendale, and Villem Vermeer. 3d shock wave visualization on unstructured grids. 1985.

[2] David Darmofal. Hierarchal visualization of three-dimensional vortical flow calculations. Master's project, M.I.T., Aero/Astro depatrment, June-August 1991.

[3] P.P Walatka, P.G. Burning, and Pierce L. Elson. *Plot3D Users Manual.* NASA, July 1992. NASA TM 101067.

[4] Schlicting. *Boundary-Layer Theory.* McGraw-Hill, Inc., seventh edition, 1979.

[5] Frederick S. Sherman. *Viscous Flow.* McGraw-Hill, Inc., New York, 1990.

[6] Thomas D. Taylor Roger Peyret. *Computational Methods for Fluid Flow.* Springer-Verlag, New York, 1983.

[7] William H. Press, Saul A. Teukolsky, William T. Vertterling, and Brian P. Flannery. *Numerical Recipies in Fortran*, volume 0. Cambridge University Press, Cambridge, second edition, 10 January 1992.